nature chemistry

Article

https://doi.org/10.1038/s41557-023-01381-0

Air- and photo-stable luminescent carbodicarbene-azaboraacenium ions

In the format provided by the authors and unedited

Table of Contents

Section

Pages

Acenes and related neutral BN acenes

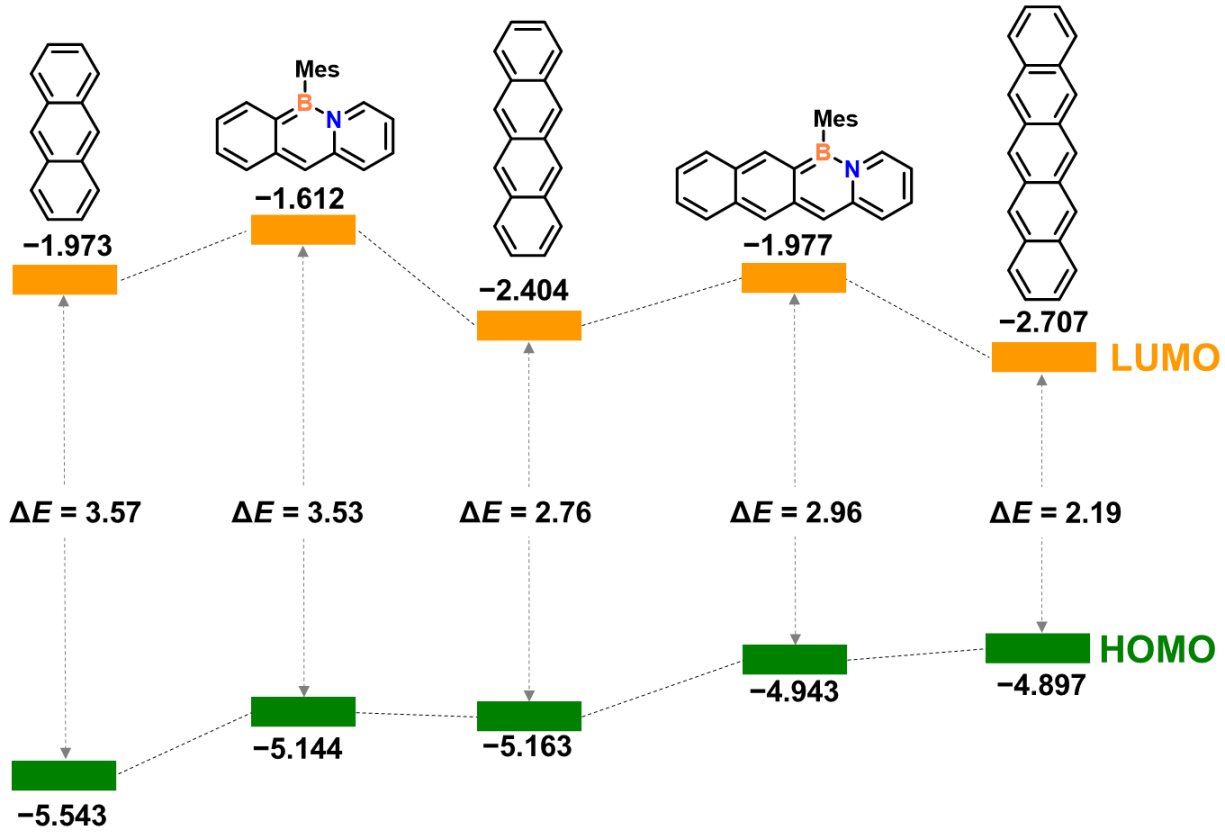

Supplementary Figure 1. Calculated frontier orbital energies (in eV, gas phase) of anthracene, neutral 9,9a-BN-anthracene, tetracene, neutral 12,12a-BN-tetracene as well as pentacene (from left to right) at the B3LYP-D3(BJ)/def2-TZVP level of theory.

General Procedures

All air- and moisture-sensitive reactions were carried out under an inert atmosphere of argon using standard Schlenk techniques or in a MBRAUN LABmaster glovebox equipped with a −36 ºC freezer. Reaction solvents including toluene, hexanes, diethyl ether and tetrahydrofuran (THF) were purified by distillation over Na/benzophenone. Dichloromethane (DCM) and chlorobenzene were purified via distillation over CaH_2. Dry acetonitrile (MeCN) was purchased from Millipore Sigma and used as received in a SureSeal. Deuterated solvents were purchased from Cambridge Isotope Laboratories and distilled over Na/benzophenone (C_6D_6) or CaH_2 (CD_3CN, *o*-DCB-d_4). All glassware used for reactions was oven-dried overnight at 190 ^oC. The NMR spectra were collected on Bruker Advance III 600 MHz, Bruker Advance III 800 MHz, Varian Inova 500 MHz, and Varian 600 MHz spectrometers. Proton and carbon signals are reported in ppm and referenced to residual solvent peaks of the deuterated solvent (^1H: $CDCl_3$ δ 7.26, CD_2Cl_2 δ 5.32; CD_3CN δ 1.94; *o*-DCB-d_4 δ 7.19, 6.93; ^{13}C: $CDCl_3$ δ 77.16, CD_2Cl_2 δ 53.84; CD_3CN δ 118.7, 1.4). Abbreviations are as follows; s = singlet, d = doublet, t = triplet, hept = heptet, dt = doublet of triplets, m = multiplet, br = broad. All boron signals are reported in ppm and were referenced to an external standard, BF_3•Et_2O (^{11}B: δ = 0.00). Due to a borosilicate NMR probe, there is a broad signal observed from −25 to 25 ppm. Elemental analyses were performed at the University of Virginia Department of Chemistry using a Perkin Elmer 2400 Series II Instrument. Single crystal X-ray diffraction data were collected on a Bruker D8Venture Photon III Duo diffractometer. The structures were solved and refined using the Bruker SHELXTL Software Package within OLEX2 1.5. The following compounds were prepared according to literature procedures: B−N-chelate *ortho*-borylated compound **4a** and **4b**,[1] bis(1-isopropyl-3-methyl-benzimidazol-2-ylidene)methane [CDC **L1**] and bis(1-cyclohexyl-3-methyl-benzimidazol-2-ylidene)methane [CDC **L2**].[2] All other chemicals were purchased from Millipore Sigma or Ambeed and used as received.

Synthetic Procedures

Synthesis of 5

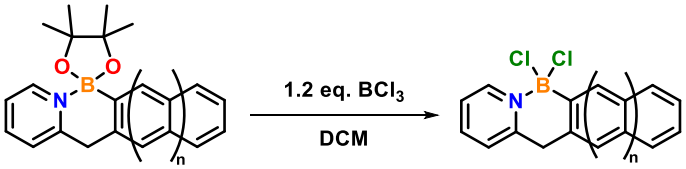

n=0, **4a**
n=1, **4b**

n=0, **5a**
n=1, **5b**

To a solution of **4**[1] (2.95 g for **4a**, 3.15 g for **4b**,10 mmol, 1 eq.) in dry DCM (2 mL), a solution of BCl_3 (1 M in DCM) (12 mL, 12 mmol, 1.2 eq.) was added dropwise at 0°C under argon protection. The reaction was stirred at room temperature for 16 hrs before the resulting mixture was concentrated and washed with hexanes (50 mL). The final product was isolated by recyclization from a mixture of DCM and hexanes.

5a, light grey solid (1.74 g, 70% yield). ^{1}H NMR (600 MHz, $CDCl_3$, 20 °C) δ 9.56 (dd, *J* = 6.2, 1.6 Hz, 1H, ArC*H*), 8.05 (td, *J* = 7.7, 1.6 Hz, 1H, ArC*H*), 8.01 (dd, *J* = 7.4, 1.4 Hz, 1H, ArC*H*), 7.70 – 7.64 (m, 1H, ArC*H*), 7.64 – 7.60 (m, 1H, ArC*H*), 7.41 – 7.33 (m, 1H, ArC*H*), 7.29 (td, *J* = 7.4, 1.5 Hz, 1H, ArC*H*), 7.24 (d, *J* = 7.1 Hz, 1H, ArC*H*), 4.45 (s, 2H, CH_2). ^{13}C{^{1}H} NMR (201 MHz, $CDCl_3$, 20 °C) δ 156.9, 144.7, 142.4, 133.8, 132.0, 128.0, 127.2, 126.4, 125.9, 123.8, 38.8. ^{11}B{^{1}H} NMR (192 MHz, $CDCl_3$, 20 °C) δ 6.2. Anal. Calcd. For $C_{12}H_{10}BCl_2N$: C, 57.67; H, 4.03; N, 5.60%. Found: C, 57.60; H, 4.19; N, 5.77 %.

5b, white solid (2.49 g, 83% yield). ^{1}H NMR (600 MHz, CD_2Cl_2, 20 °C) δ 9.61 (dd, *J* = 6.2, 1.6 Hz, 1H, ArC*H*), 8.41 (s, 1H, ArC*H*), 8.14 (td, *J* = 7.7, 1.6 Hz, 1H, ArC*H*), 7.95 – 7.89 (m, 1H, ArC*H*), 7.85 – 7.79 (m, 1H, ArC*H*), 7.78 – 7.73 (m, 2H, ArC*H*), 7.70 (ddd, *J* = 7.6, 6.0, 1.4 Hz, 1H, ArC*H*), 7.51 – 7.43 (m, 2H, ArC*H*), 4.65 (s, 2H, CH_2). ^{13}C{^{1}H} NMR (201 MHz, CD_2Cl_2, 20 °C) δ 157.4, 144.8, 143.1, 133.5, 133.1, 132.7, 131.7, 128.7, 127.4, 127.0, 126.5, 125.9, 124.4, 124.4, 39.5. ^{11}B{^{1}H} NMR (192 MHz, $CDCl_3$, 20 °C) δ 6.4. Anal. Calcd. For $C_{16}H_{12}BCl_2N$: C, 64.06; H, 4.03; N, 4.67%. Found: C, 63.70; H, 4.00; N, 4.53%.

One-pot synthesis of BN-acene cations (Compound 1, 2 and 3)

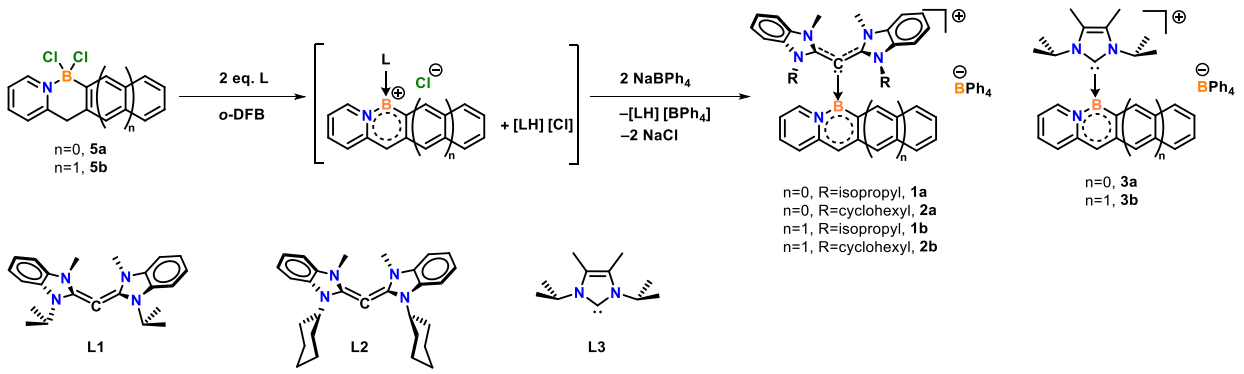

To a solution of CDC ligand (**L1** or **L2**) or NHC ligand (**L3**) (0.2 mmol, 2 eq.) in *o*-DFB (3 mL), the corresponding dichloroboranes derivative **5a/5b** (25 mg for **5a**, 30 mg for **5b**, 0.1 mmol, 1 eq.) was added. The reaction was protected from light and stirred at room temperature for 18 hrs. Then sodium tetraphenylborate (68mg, 0.2 mmol, 2 eq.) was added into the resulting mixtures and continue to stir in the dark for 12 hrs. The solution was filtered through a 0.45 µm PTFE syringe filter and the solvent was removed under vacuum. The residue was re-dissolve in 60/40 o-DFB/hexanes (10 mL) was added and the mixture were allowed to stand still at r.t. for 12 hrs. During which time, a colorless precipitate formed, which was the protonated ligand $[(LH)]^+[BPh_4]^-$. After filtration and the solution was placed into the in the glovebox fridge (−36 °C) for overnight. The resulting precipitate was isolated by filtration and dried *in vacuo* to afford the product. Analytical pure product can be obtained from the second recrystallization from a 70/30 *o*-DFB/hexanes (for **1a** and **2a**, **3a**) or 70/30 THF/hexanes (for **1b** and **2b**) at −36 °C.

Azaboraanthracenium ion **1a** (synthesized from **5a** and CDC ligand **L1**), bright yellow solid (71 mg, 83% yield). ^{1}H NMR (600 MHz, *o*-DCB-d_4, 120 °C) δ 7.69 –7.66 (m, 9H, Ar*H* 1H/BPh_4–Ar*H* 8H), 7.48 – 7.45 (ddd, *J* = 8.2, 6.9, 1.2 Hz, 1H, Ar*H*), 7.35 (d, *J* = 7.4 Hz, 1H, Ar*H*), 7.29 – 7.25 (m, 3H, Ar*H*), 7.20 – 7.14 (m, 5H, Ar*H* overlap with *o-DCB-d*$_4$), 7.12 (dd, *J* = 7.5, 1.6 Hz, 1H, Ar*H*), 7.08 (m, 1H, Ar*H*), 7.02 – 6.97 (m, 10H, Ar*H* 2H/BPh_4–Ar*H* 8H), 6.85 – 6.82 (m, 4H, BPh_4–Ar*H*), 6.56 – 6.53 (m, 1H, Ar*H*), 6.00 (ddd, *J* = 7.5, 6.2, 1.4 Hz, 1H, Ar*H*), 4.32– 4.20 (m, 2H, C*H*(CH_3)$_2$), 3.06 (s, 3H, C*H*$_3$), 3.03 (s, 3H, C*H*$_3$), 1.13 – 1.01 (m, 9H, CH(C*H*$_3$)$_2$), 0.83 (s, 3H, CH(C*H*$_3$)$_2$). Discernable ^{13}C{^{1}H} NMR cannot be obtained due to the limited solubility in *o*-DCB-d_4 and/or gradual decomposition at the high collecting temperature. ^{11}B{^{1}H} NMR (192 MHz, CD_3CN, 20 °C) δ 36.4 (*B*$^+$), −6.6 (*B*Ph_4^-). Anal. Calcd. For $C_{59}H_{57}B_2N_5$: C, 82.62; H, 6.70; N, 8.16 %. Found: C, 82.62; H, 6.69; N, 7.99 %.

Azaboratetracenium ion **1b** (synthesized from **5b** and CDC ligand **L2**), red solid (82 mg, 90% yield). ^{1}H NMR (600 MHz, *o*-DCB-d_4, 120 °C) δ 8.15 (s, 1H, Ar*H*), 7.81 (s, 1H, Ar*H*), 7.79 (d, *J* = 8.5 Hz, 1H), 7.75 – 7.72 (m, 8H, BPh_4–Ar*H*), 7.35 – 7.29 (m, 3H, Ar*H*), 7.22 – 7.15 (m, 8H, Ar*H*), 7.08 – 7.02 (m, 11H, Ar*H* 3H/BPh_4–Ar*H* 8H), 6.93 – 6.88 (m, 4H, BPh_4–Ar*H*), 6.42 (dd, *J* = 9.3, 6.0 Hz, 1H, Ar*H*), 5.85 (t, *J* = 6.7 Hz, 1H, Ar*H*), 4.30 (s, 2H, C*H*(CH_3)$_2$), 3.11 (s, 3H, C*H*$_3$), 3.00 (s, 3H, C*H*$_3$), 1.13 (brs, 12H, CH(C*H*$_3$)$_2$). Discernable ^{13}C{^{1}H} NMR cannot be obtained due to the limited solubility in *o*-DCB-d_4 and/or gradual decomposition at the high collecting temperature.

$^{11}B\{^{1}H\}$ NMR (192 MHz, CD_2Cl_2, 20 °C) δ 37.4 (B^+), −6.6 (BPh_4^-). Anal. Calcd. For $C_{63}H_{59}B_2N_5$: C, 83.35; H, 6.55; N, 7.71 %. Found: C, 83.53; H, 6.56; N, 7.69 %.

Azaboraanthracenium ion **2a** (synthesized from **5a** and CDC ligand **L1**), bright yellow solid (80 mg, 85% yield). ^{1}H NMR (600 MHz, *o*-DCB-d_4, 140 °C) δ 7.71 – 7.68 (m, 9H, Ar*H* 1H/BPh_4–Ar*H* 8H), 7.50 – 7.48 (m, 2H, Ar*H*), 7.43 (d, *J* = 8.0 Hz, 1H, ArH), 7.37 – 7.35 (m, 2H, Ar*H*), 7.19 – 7.12 (m, 6H, Ar*H*), 7.09 – 7.05 (m, 3H, Ar*H*), 7.01 (t, *J* = 7.4 Hz, 8H, BPh_4–Ar*H*), 6.86 (t, *J* = 7.2 Hz, 4H, BPh_4–Ar*H*), 6.60 (dd, *J* = 9.2, 6.1 Hz, 1H, Ar*H*), 6.10 (m, 1H, Ar*H*), 4.04 (s, 1H, C*H*$(CH_3)_2$), 3.91– 3.89 (m, 1H, C*H*$(CH_3)_2$), 3.14 (s, 3H, C*H*$_3$), 3.07 (s, 3H, C*H*$_3$), 2.04 – 1.79 (m, 3H, cyclohexyl-*H*), 1.76 – 1.55 (m, 2H, cyclohexyl-*H*), 1.43 – 1.41 (m, 3H, cyclohexyl-*H*), 1.30 – 1.27 (m, 3H, cyclohexyl-*H*), 1.21 – 1.19 (m, 2H, cyclohexyl-*H*), 0.90 – 0.86 (m, 3H, cyclohexyl-*H*), 0.64 (s, 1H, cyclohexyl-*H*), 0.36 – 0.25 (m, 3H, cyclohexyl-*H*). Discernable $^{13}C\{^{1}H\}$ NMR cannot be obtained due to the limited solubility in *o*-DCB-d_4 even at high temperature. $^{11}B\{^{1}H\}$ NMR (192 MHz, CD_3CN, 20 °C) δ 36.5 (B^+), −6.7 (BPh_4^-). Anal. Calcd. For $C_{65}H_{65}B_2N_5$: C, 83.24; H, 6.99; N, 7.47 %. Found: C, 83.50; H, 6.70; N, 7.50 %.

Azaboratrtracenium ion **2b** (synthesized from **5b** and CDC ligand **L2**), orange-red solid (75 mg, 76% yield). ^{1}H NMR (600 MHz, *o*-DCB-d_4, 145 °C) δ 8.18 (s, 1H, Ar-*H*), 7.98 (s, 1H), 7.79 (d, *J* = 8.5 Hz, 1H, Ar-*H*), 7.69 – 7.67 (m, 8H, BPh_4–Ar*H* 8H), 7.43 – 7.40 (m, 2H, Ar-*H*), 7.36 – 7.28 (m, 2H, Ar-*H*), 7.25 – 7.16 (m, 6H, Ar-*H* overlap with *o-DCB-d*$_4$), 7.11 – 7.06 (m, 4H, Ar-*H*), 6.99 (t, *J* = 7.3 Hz, 8H, BPh_4–Ar*H* 8H), 6.84 (t, *J* = 7.2 Hz, 4H, BPh_4–Ar*H* 4H), 6.46 (dd, *J* = 9.3, 6.0 Hz, 1H, Ar-*H*), 5.93 (t, *J* = 6.8 Hz, 1H, Ar-*H*), 4.11 – 4.01 (m, 2H, C*H*$(CH_3)_2$), 3.21 (s, 3H, C*H*$_3$), 3.08 (s, 3H, C*H*$_3$), 1.94 – 1.83 (m, 3H, cyclohexyl-*H*), 1.66 – 1.13 (m, 11H, cyclohexyl-*H*), 0.91 – 0.69 (m, 4H, cyclohexyl-*H*), 0.33 – 0.29 (m, 2H, cyclohexyl-*H*). Discernable $^{13}C\{^{1}H\}$ NMR cannot be obtained due to the limited solubility in *o*-DCB-d_4 even at the high temperature. $^{11}B\{^{1}H\}$ NMR (192 MHz, CD_3CN, 20 °C) δ 37.8 (B^+), −6.7 (BPh_4^-). Anal. Calcd. For $C_{69}H_{67}B_2N_5$: C, 83.89; H, 6.84; N, 7.09 %. Found: C, 83.60; H, 6.69; N, 6.89 %.

Azaboraanthracenium ion **3a** (synthesized from **5a** and NHC ligand **L3**), light yellow powder (44 mg, 65% yield). ^{1}H NMR (800 MHz, CD_3CN, 20 °C) δ 8.00 (dd, *J* = 8.4, 1.1 Hz, 1H, ArC*H*), 7.83 (ddd, *J* = 8.2, 6.8, 1.3 Hz, 1H, ArC*H*), 7.73 (dt, *J* = 7.9, 1.1 Hz, 1H, ArC*H*), 7.65 – 7.62 (m, 2H, ArC*H*), 7.60 (s, 1H, ArC*H*), 7.44 (ddd, *J* = 7.9, 6.8, 1.0 Hz, 1H, ArC*H*), 7.28 – 7.26 (m, 8H, BPh_4– ArC*H*), 7.10 (ddd, *J* = 9.3, 6.7, 1.0 Hz, 1H, ArC*H*), 6.99 (t, *J* = 7.5 Hz, 8H, BPh_4– ArC*H*), 6.85 – 6.83 (m, 4H, BPh_4– ArC*H*), 6.65 (ddd, *J* = 7.3, 6.3, 1.2 Hz, 1H, ArC*H*), 4.31 (hept, *J* = 6.9 Hz, 2H, C*H*$(CH_3)_2$), 2.45 (s, 6H, C*H*$_3$), 1.32 (d, *J* = 6.9 Hz, 6H, CH(C*H*$_3)_2$), 1.25 (d, *J* = 6.9 Hz, 6H, CH(C*H*$_3)_2$). $^{13}C\{^{1}H\}$ NMR (800 MHz, CD_3CN, 20 °C) δ 164.9 (q, *J* = 48.3 Hz), 142.4, 140.0, 136.8, 135.1, 134.2, 133.5, 130.5, 128.2, 128.1, 126.7 (q, *J* = 3.3 Hz), 126.6, 125.1, 122.8, 114.7, 112.4, 54.6, 22.4, 21.6, 10.5. $^{11}B\{^{1}H\}$ NMR (192 MHz, CD_3CN, 20 °C) δ 31.8 (B^+), −6.6 (BPh_4^-). Anal. Calcd. For $C_{47}H_{49}B_2N_3$: C, 83.32; H, 7.29; N, 6.20 %. Found: C, 83.32; H, 7.39; N, 6.02 %.

Synthesis of Mes-BN acene (Compound 6)

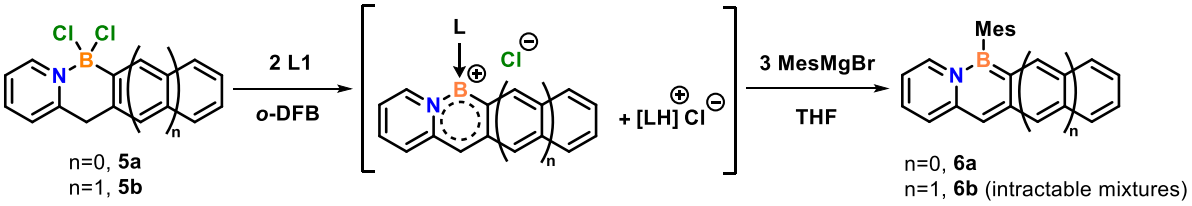

To a solution of CDC ligand **L1** (140 mg, 0.4 mmol, 2 eq.) in *o*-DFB (3 mL), the corresponding dichloroborane derivative **5a/5b** (50 mg for **5a**, 60 mg for **5b**, 0.2 mmol, 1 eq.) was added in the dark. The reaction was stirred at room temperature for 18 hrs. The solution was filtered through a 0.25 μm PTFE syringe filter and the solvent was removed under vacuum. The residue was redissloved in THF (5 mL) and cooled to 0 ^{o}C, MesMgBr (1 M in THF) (0.6 mL, 3 eq.) was added dropwise and stirred at r.t. for 3 hrs. After filteration through a plug of silica gel (1 cm) in the glovebox and washed with THF, the volatiles were removed *in vacuo* to give the title compound (**6a** or **6b**).

6a (synthesized from **5a**), yellow powder (44 mg, 77% yield). ^{1}H NMR (600 MHz, CD_2Cl_2, 20 °C) δ 7.79 (m, 1H), 7.71 (ddd, *J* = 7.8, 1.5, 0.8 Hz, 1H), 7.66 (ddd, *J* = 8.2, 6.8, 1.4 Hz, 1H), 7.57 (dt, *J* = 7.3, 1.1 Hz, 1H), 7.33 (dt, *J* = 9.2, 1.3 Hz, 1H), 7.24 (ddd, *J* = 7.8, 6.8, 1.1 Hz, 1H), 7.09 (s, 1H), 6.97 (m, 2H, Mes-Ar*CH*), 6.84 (ddd, *J* = 9.2, 6.0, 1.3 Hz, 1H), 6.23 (ddd, *J* = 7.4, 6.1, 1.4 Hz, 1H), 2.38 (s, 3H, Mes-CH_3), 1.96 (s, 6H, Mes-CH_3). ^{11}B{^{1}H} NMR (192 MHz, CD_2Cl_2, 20 °C) δ 40.8. The ^{1}H-NMR and ^{11}B-NMR data in agreement with the literature.[3]

Compound **6b** was obtained as an intractable mixture. The red crude solution is prone to rapid decomposition (with noticeable color fading) in solution even under dark during work up in the glove box.

Photo-oxidation of Mes-BN acene 6a

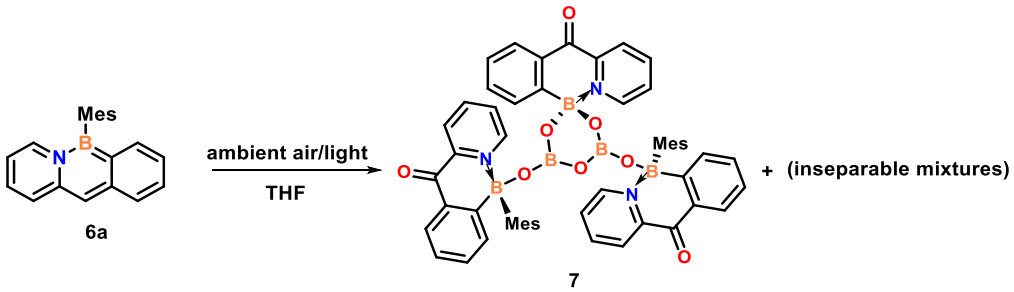

A solution of **6a** (297 mg, 1 mmol) in THF (5 mL) was prepared and allowed to stir under ambient light while exposed to air. The solution color faded after ca. 8 hours and NMR analysis indicated the crude product contained inseparable mixtures. However, a single crystal from was grown from the mixtures, and the structure was identified to be **7** and the X-ray structure was shown in Supplementary Figure 57. A proposed mechanism for the formation **7** *via* zwitterionic intermediates is shown in Supplementary Figure 113.

NMR Spectra

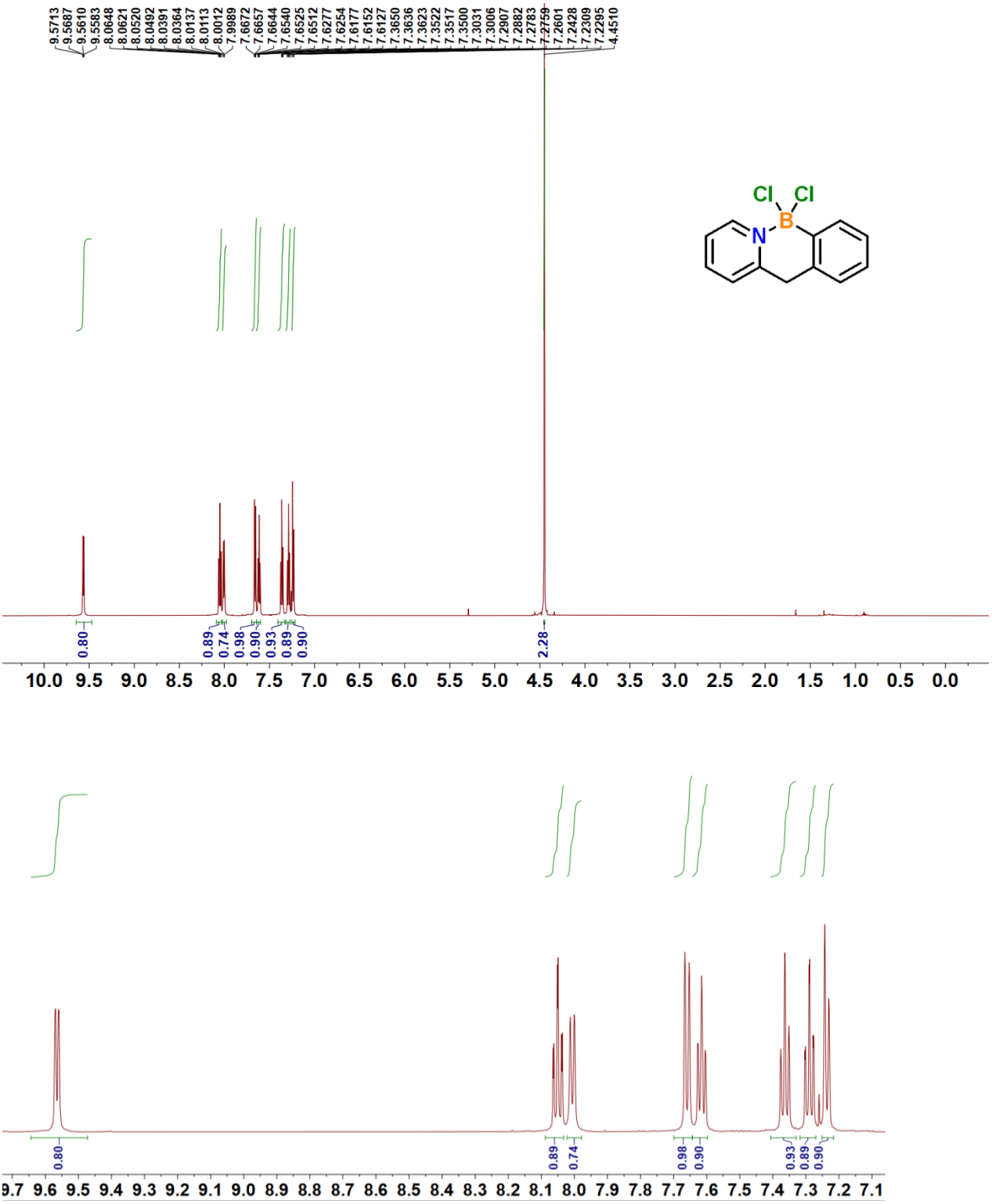

Supplementary Figure 2. ^{1}H NMR (600 MHz, $CDCl_3$, 25 °C) spectrum for **5a** (top) and its zoomed aromatic region (bottom).

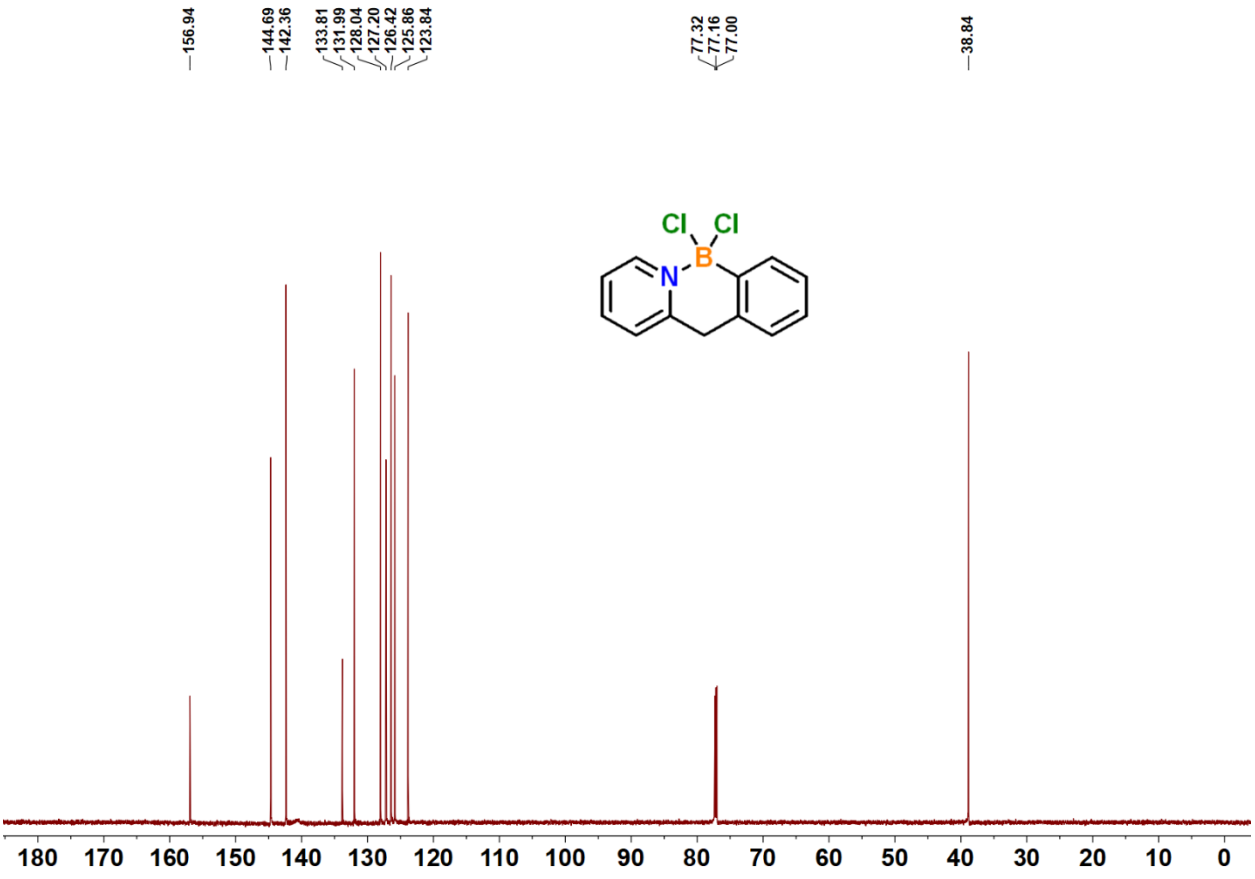

Supplementary Figure 3. ^{13}C NMR (201 MHz, $CDCl_3$, 25 °C) spectrum for **5a**.

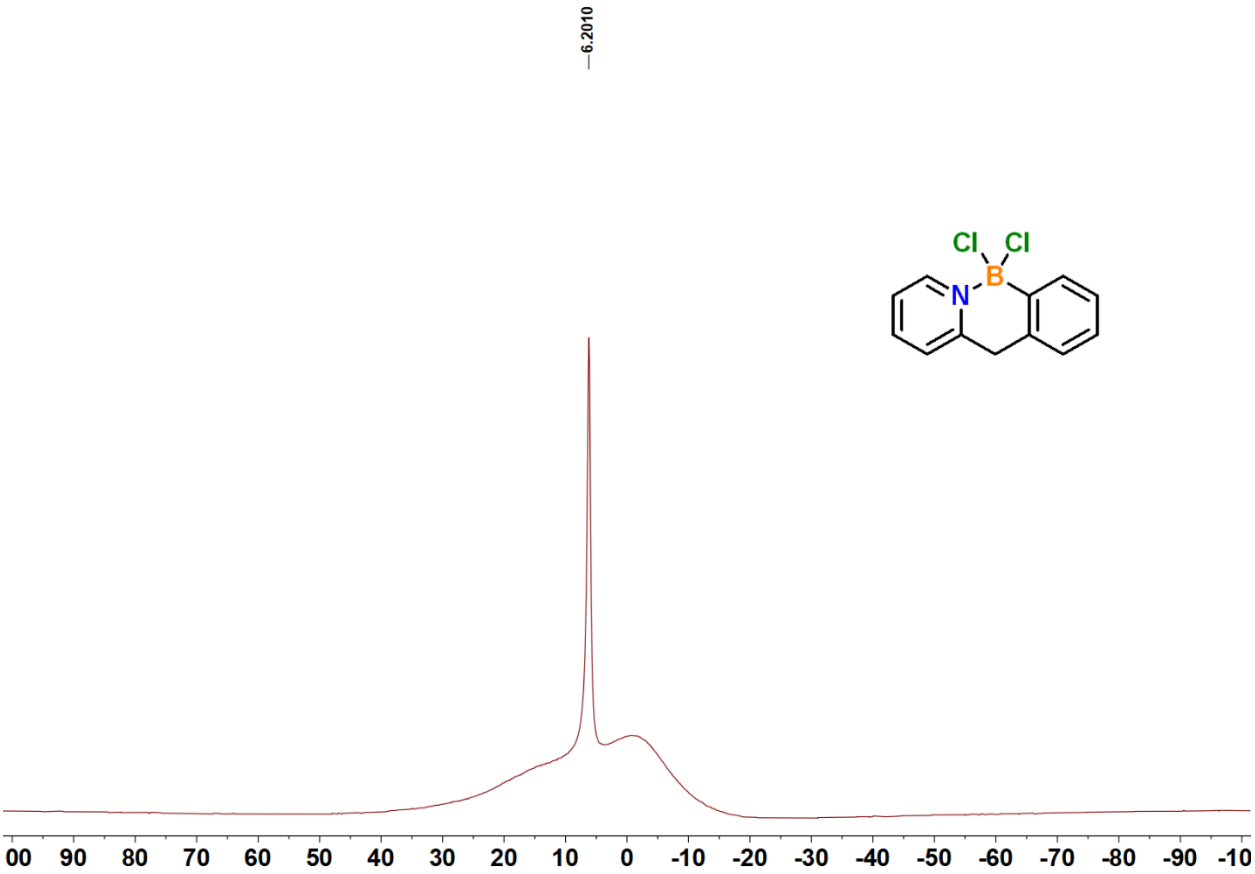

Supplementary Figure 4. $^{11}B\{^{1}H\}$ NMR (192 MHz, $CDCl_3$, 25 °C) spectrum for **5a**.

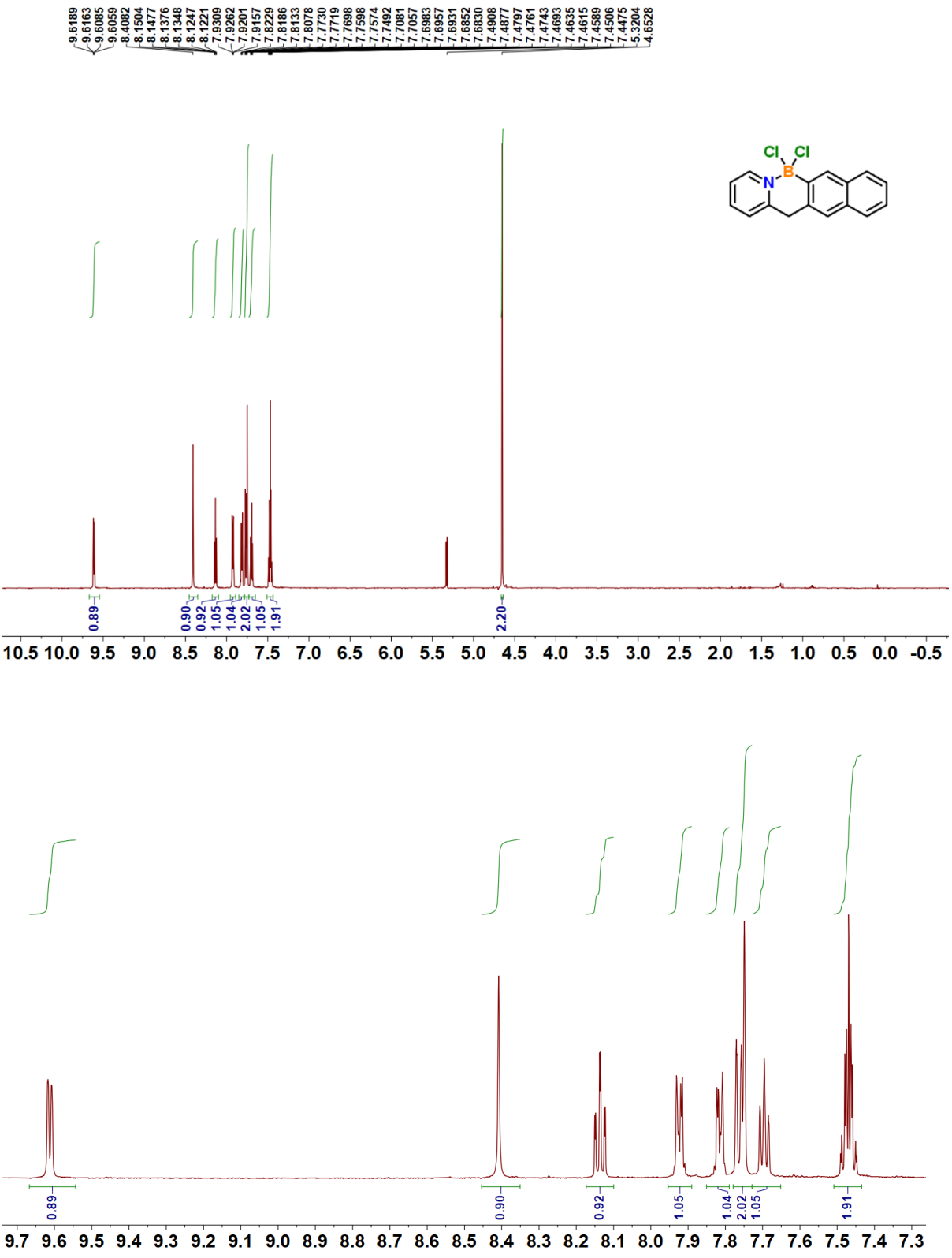

Supplementary Figure 5. ^{1}H NMR (600 MHz, CD_2Cl_2, 25 °C) spectra for **5b** (top) and its zoomed aromatic region (bottom).

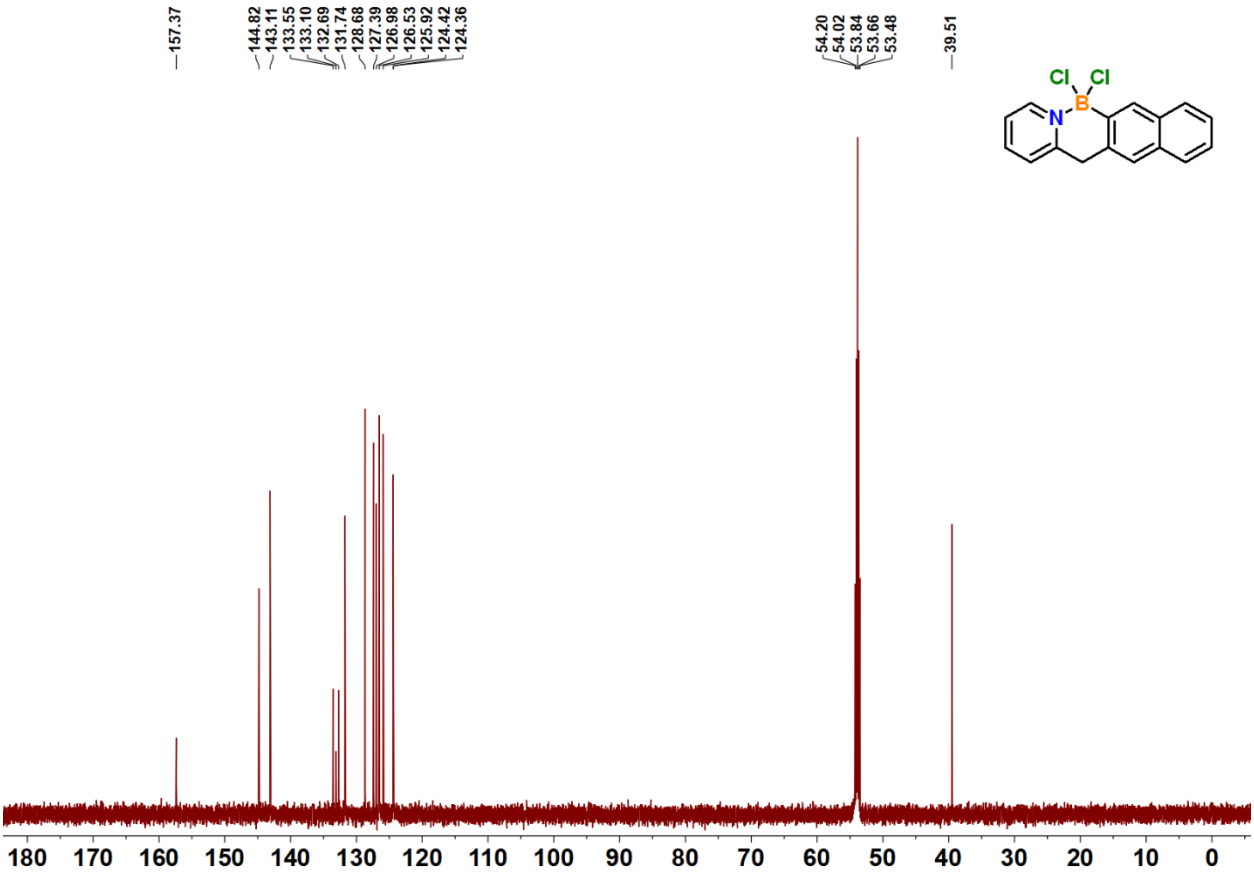

Supplementary Figure 6. ^{13}C NMR (201 MHz, CD_2Cl_2, 25 °C) spectrum for **5b**.

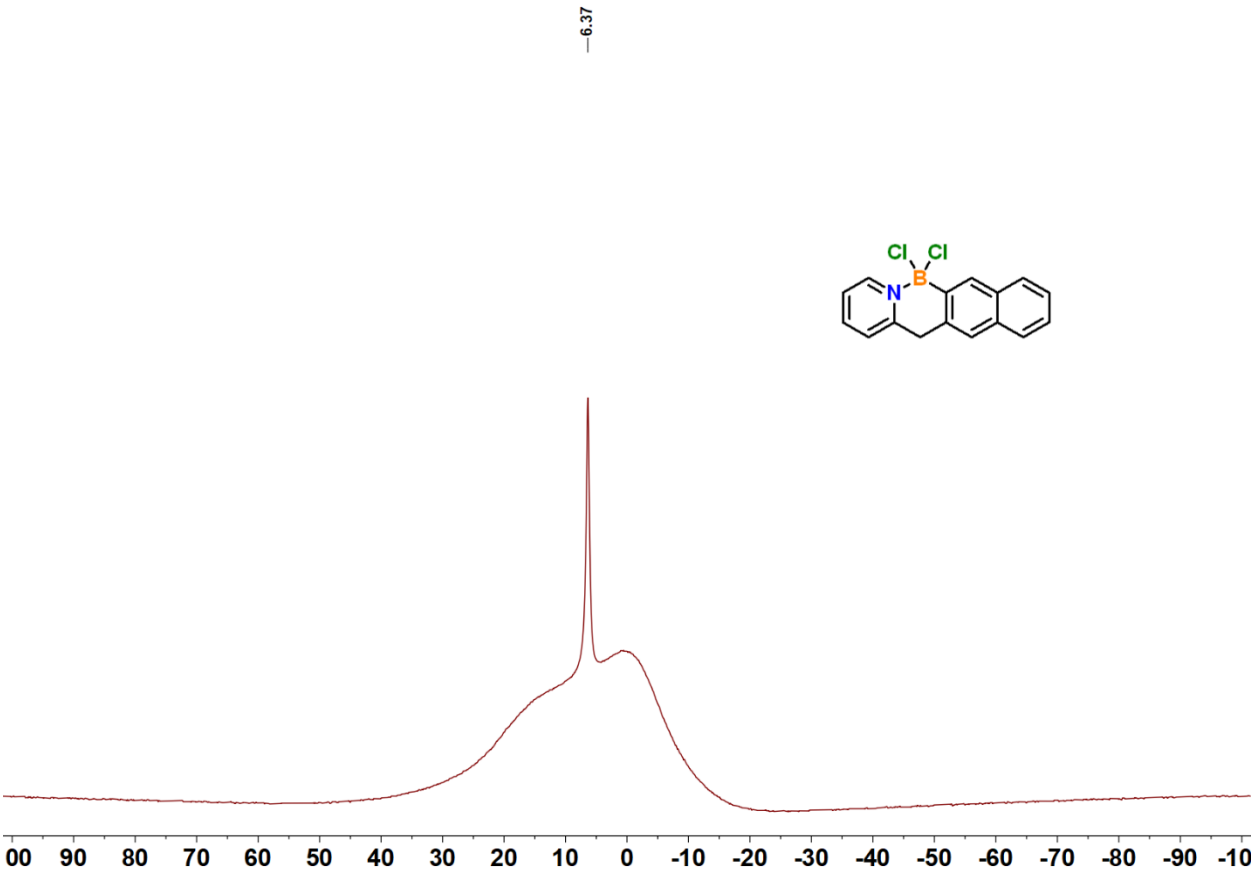

Supplementary Figure 7. $^{11}B\{^{1}H\}$ NMR (192 MHz, CD_2Cl_2, 25 °C) spectrum for **5b**.

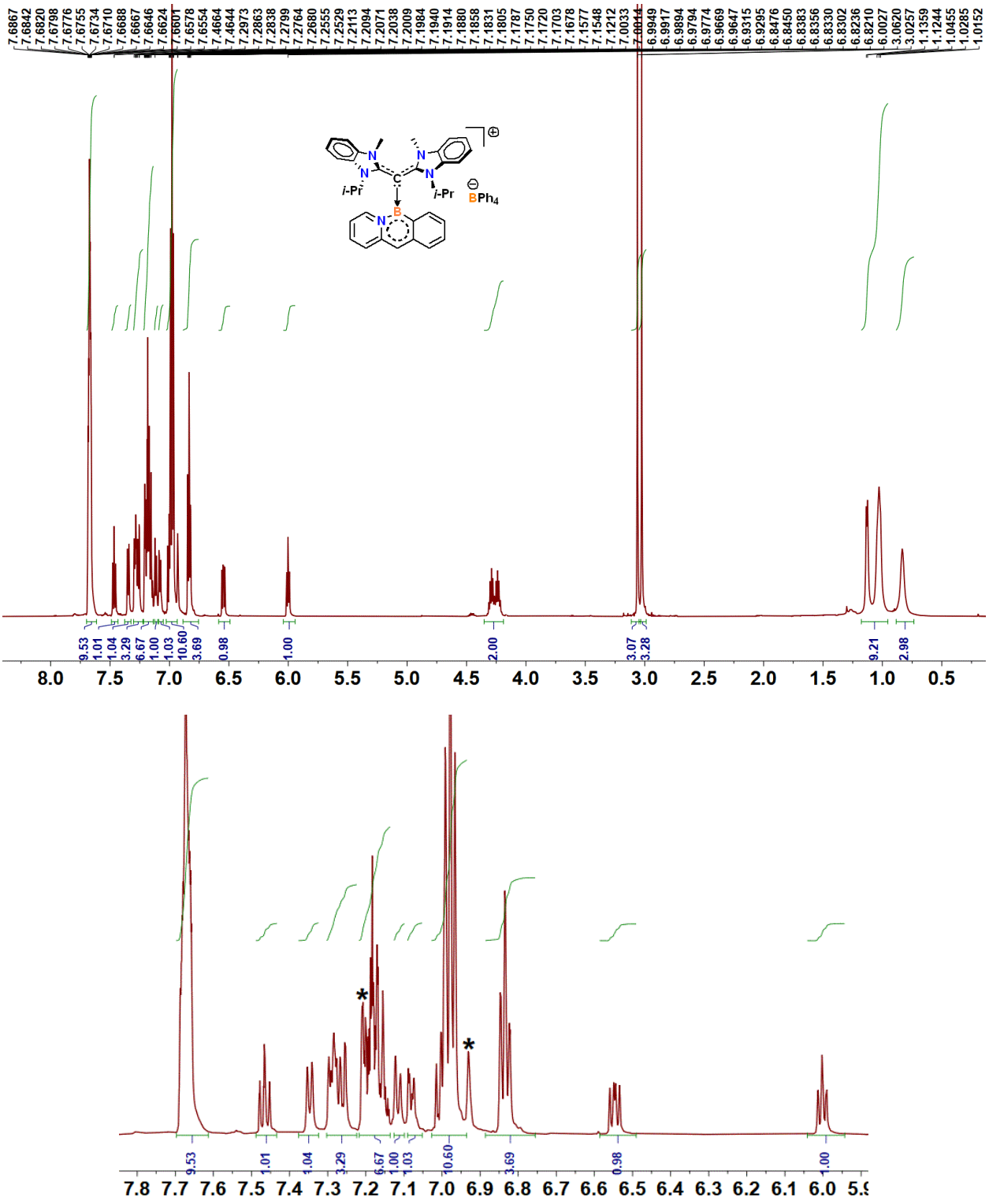

Supplementary Figure 8. ^{1}H NMR (600 MHz, *o*-DCB-d_4, 120 °C) spectra for **1a** (top) and its zoomed aromatic region (bottom). (*) denotes the *o*-DCB-d_4 residual protons. Peaks splitting for the aromatic regions was unclear when CD_3CN were used as the NMR solvent.

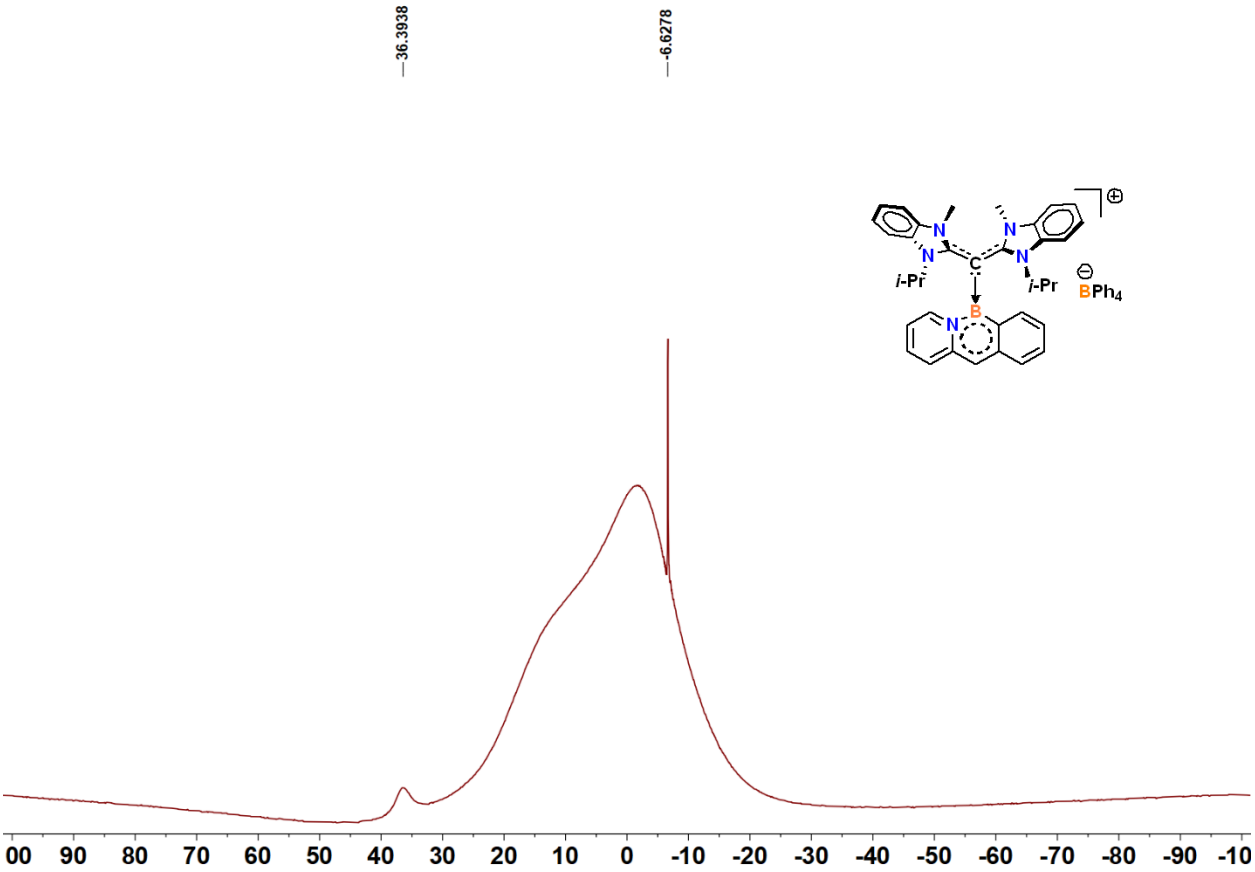

Supplementary Figure 9. $^{11}B\{^{1}H\}$ NMR (192 MHz, CD_3CN, 25 °C) spectrum for **1a**.

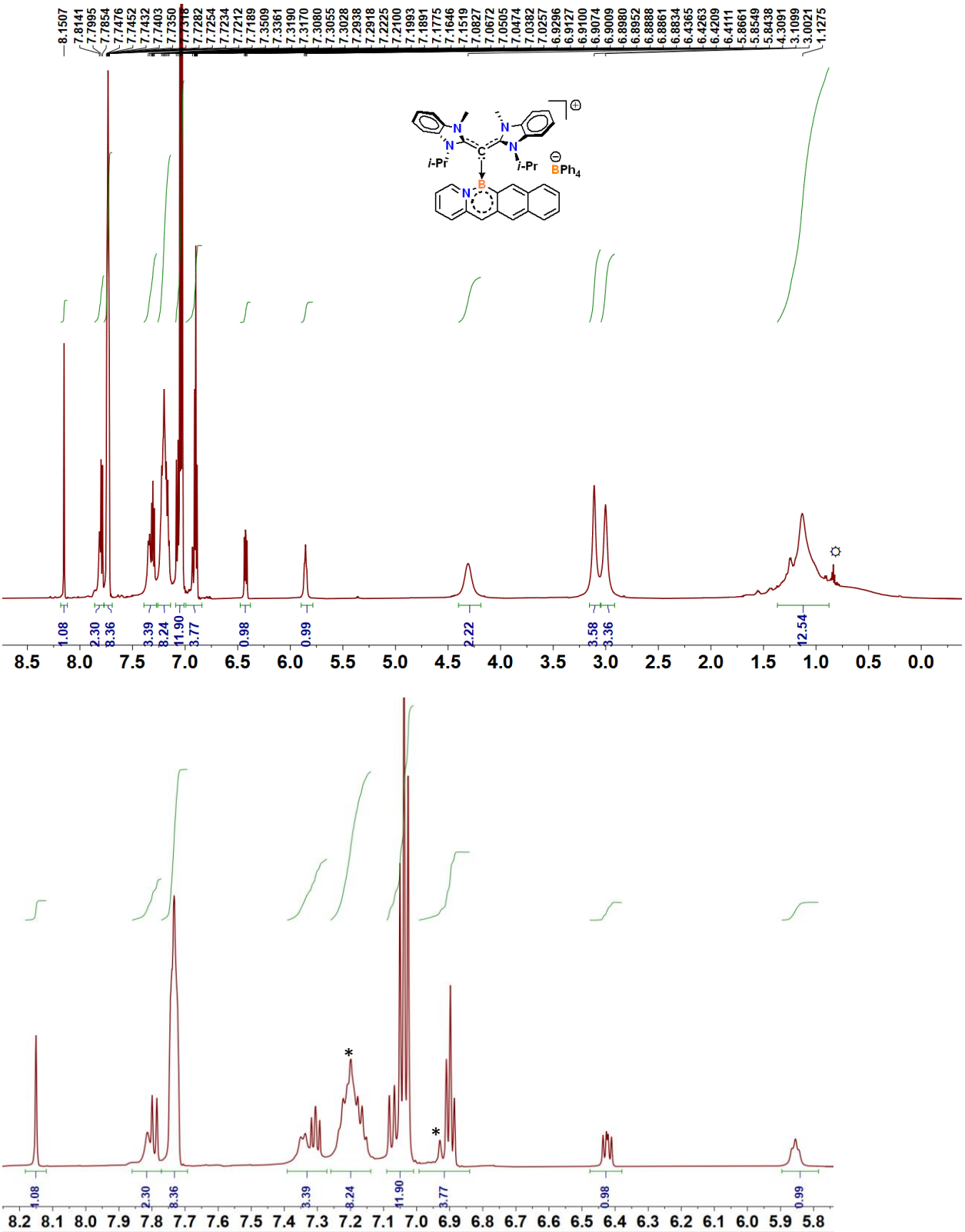

Supplementary Figure 10. ^{1}H NMR (600 MHz, o-DCB-d_4, 120 °C) spectra for **1b**. (*) denotes the *o*-DCB-d_4 residual protons. (☼) NMR solvent contaminate from the vapor (hexane or pentane) in the glove box.

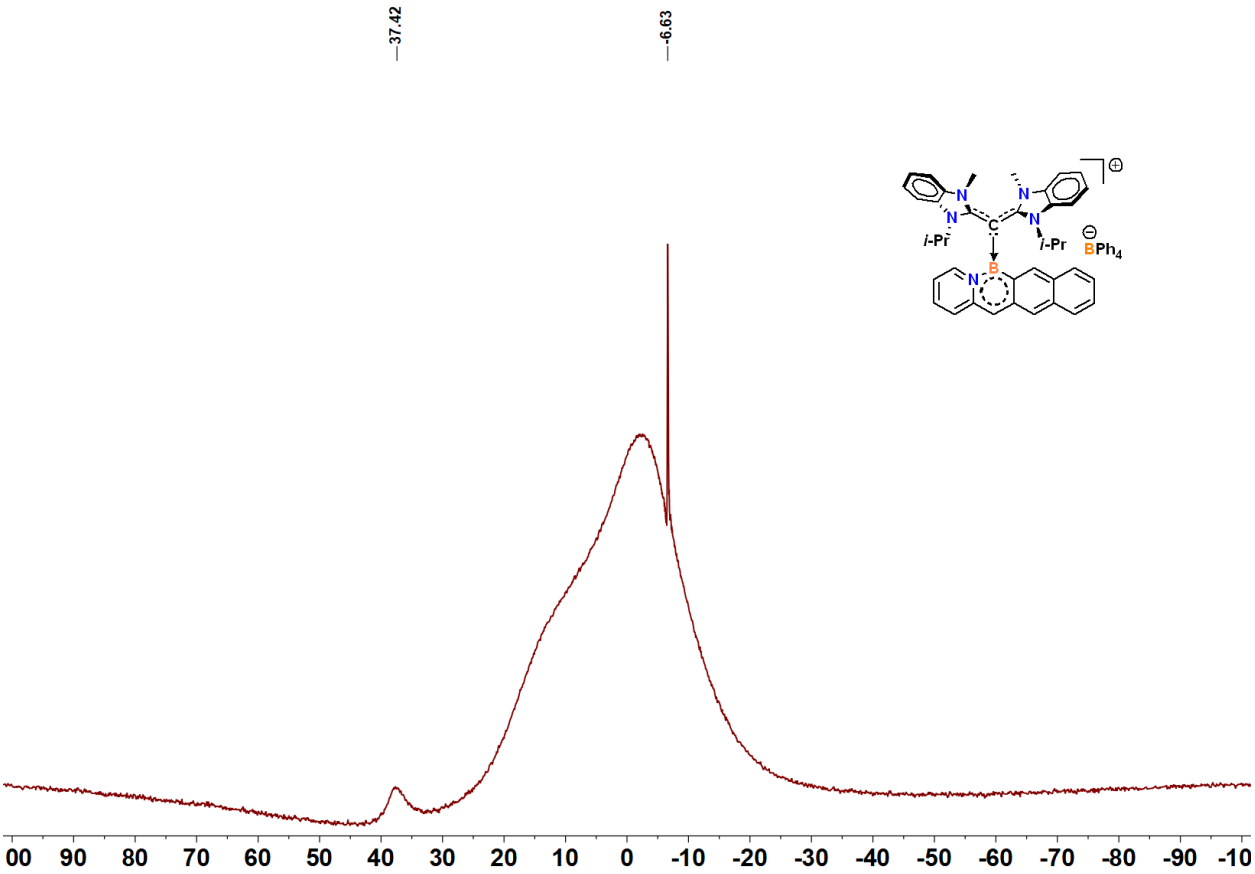

Supplementary Figure 11. $^{11}B\{^{1}H\}$ NMR (192 MHz, CD_3CN, 25 °C) spectrum for **1b**.

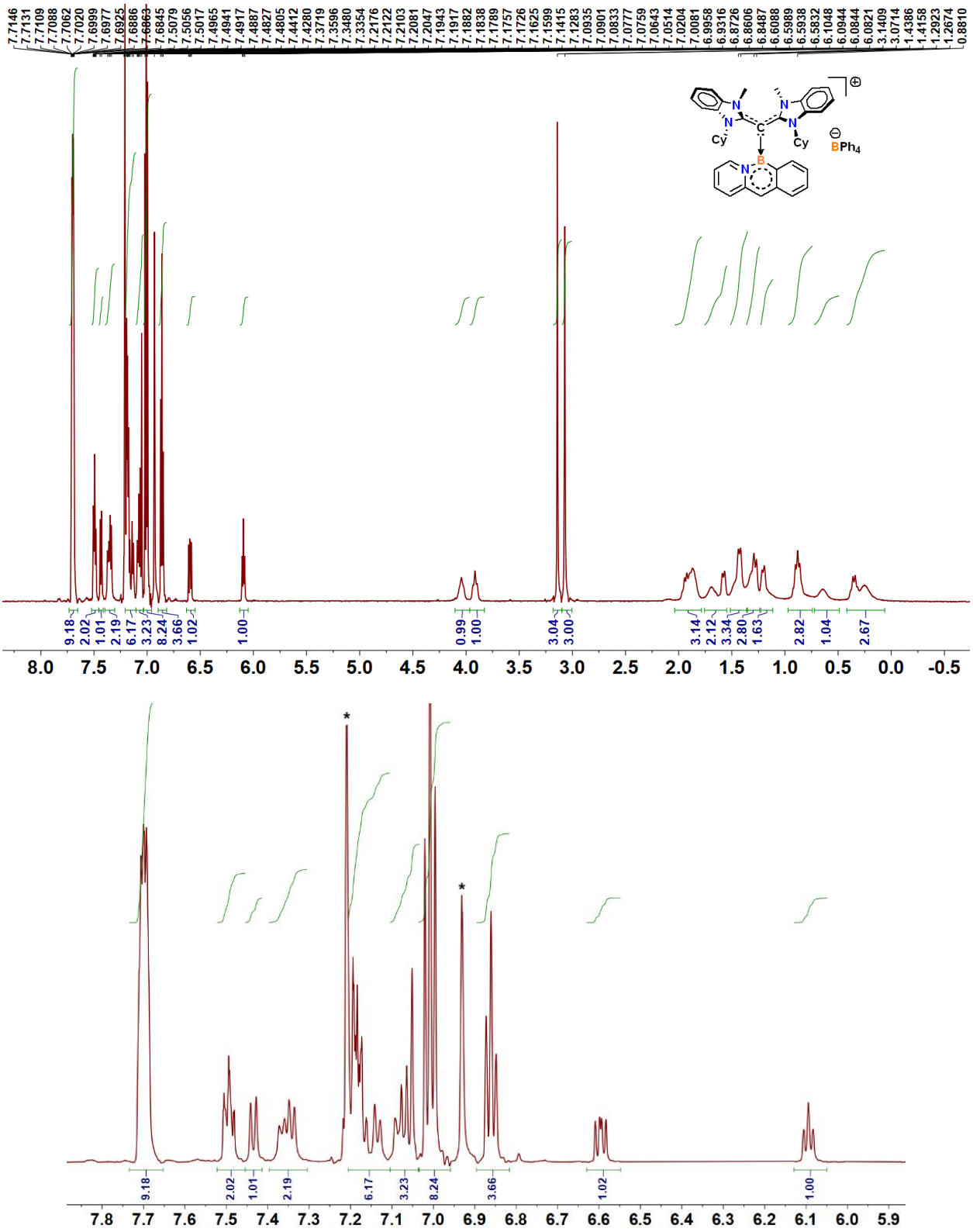

Supplementary Figure 12. ^{1}H NMR (600 MHz, *o*-DCB-d_4, 140 °C) spectra for **2a** (top) and its zoomed aromatic region (bottom). (*) denotes the *o*-DCB-d_4 residual protons.

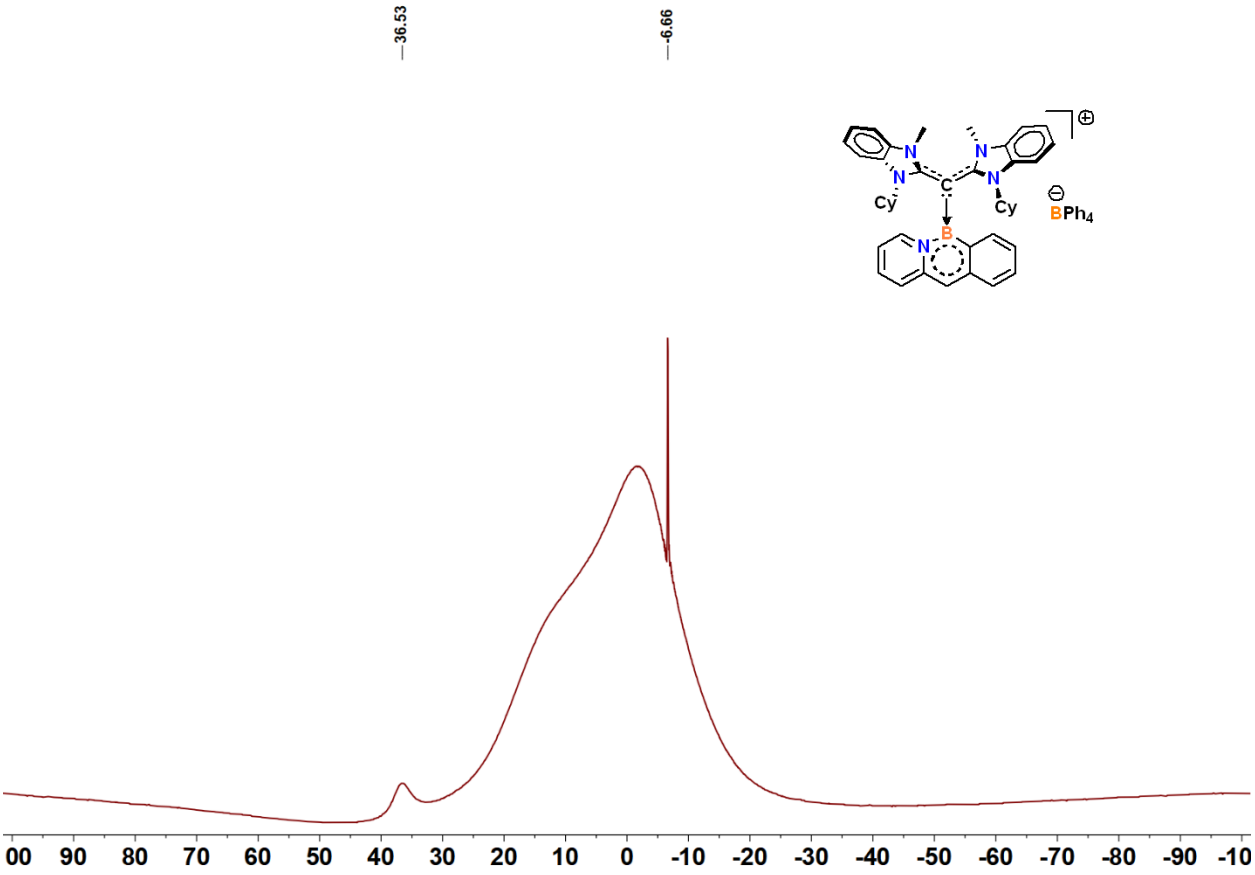

Supplementary Figure 13. $^{11}B\{^{1}H\}$ NMR (192 MHz, CD_3CN, 25 °C) spectrum for **2a**.

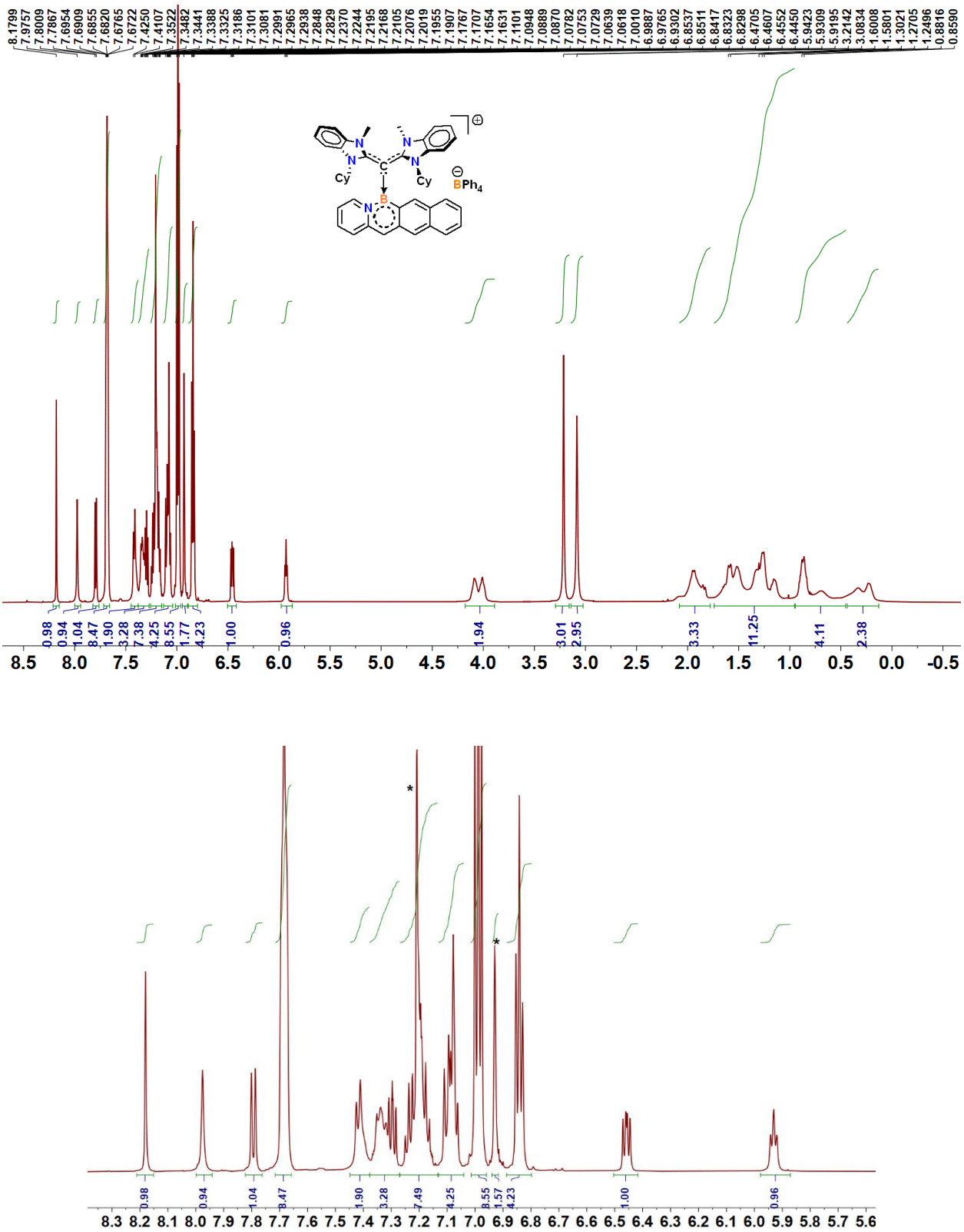

Supplementary Figure 14. ^{1}H NMR (600 MHz, *o*-DCB-d_4, 145 °C) spectra for **2b** (top) and its zoomed aromatic region (bottom). (*) denotes the *o*-DCB-d_4 residual protons.

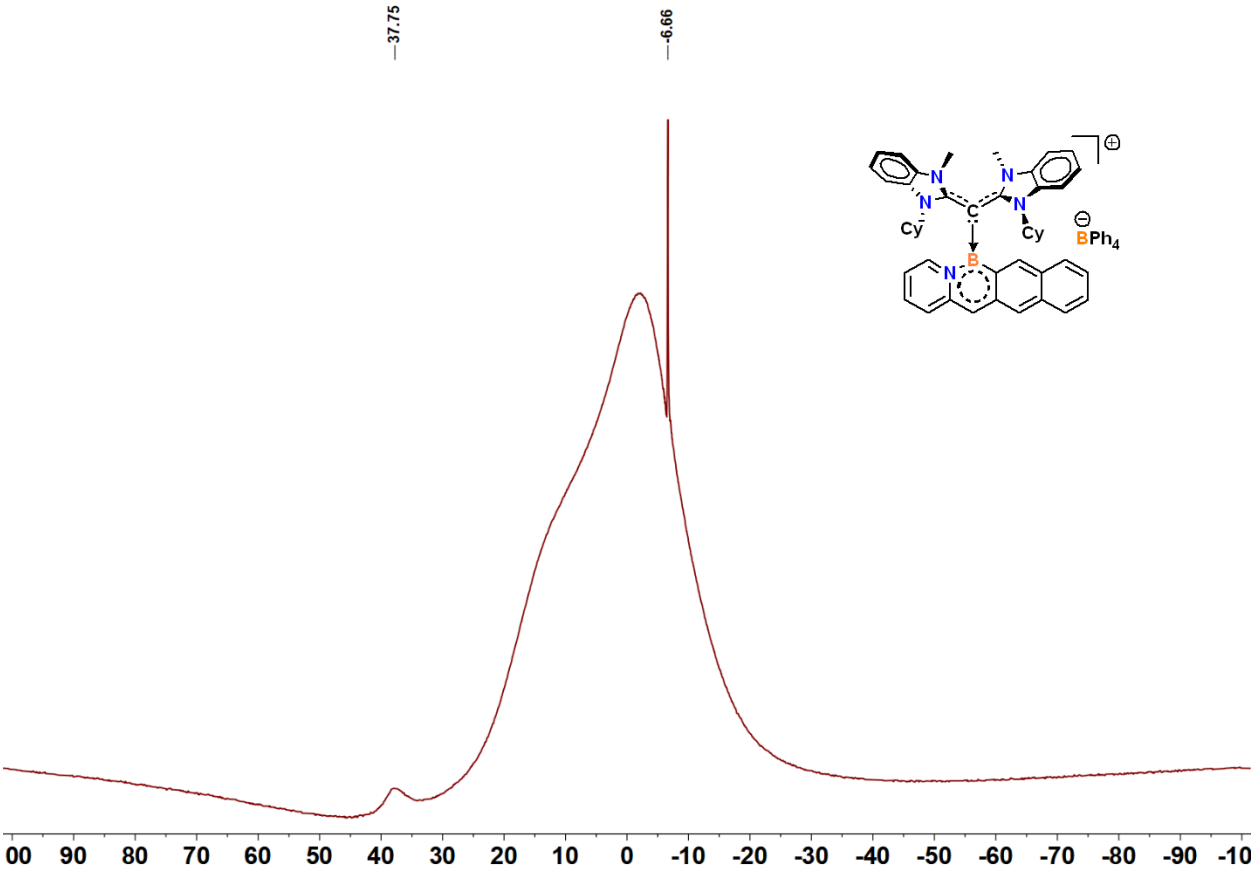

Supplementary Figure 15. $^{11}B\{^{1}H\}$ NMR (192 MHz, CD_3CN, 25 °C) spectrum for **2b**.

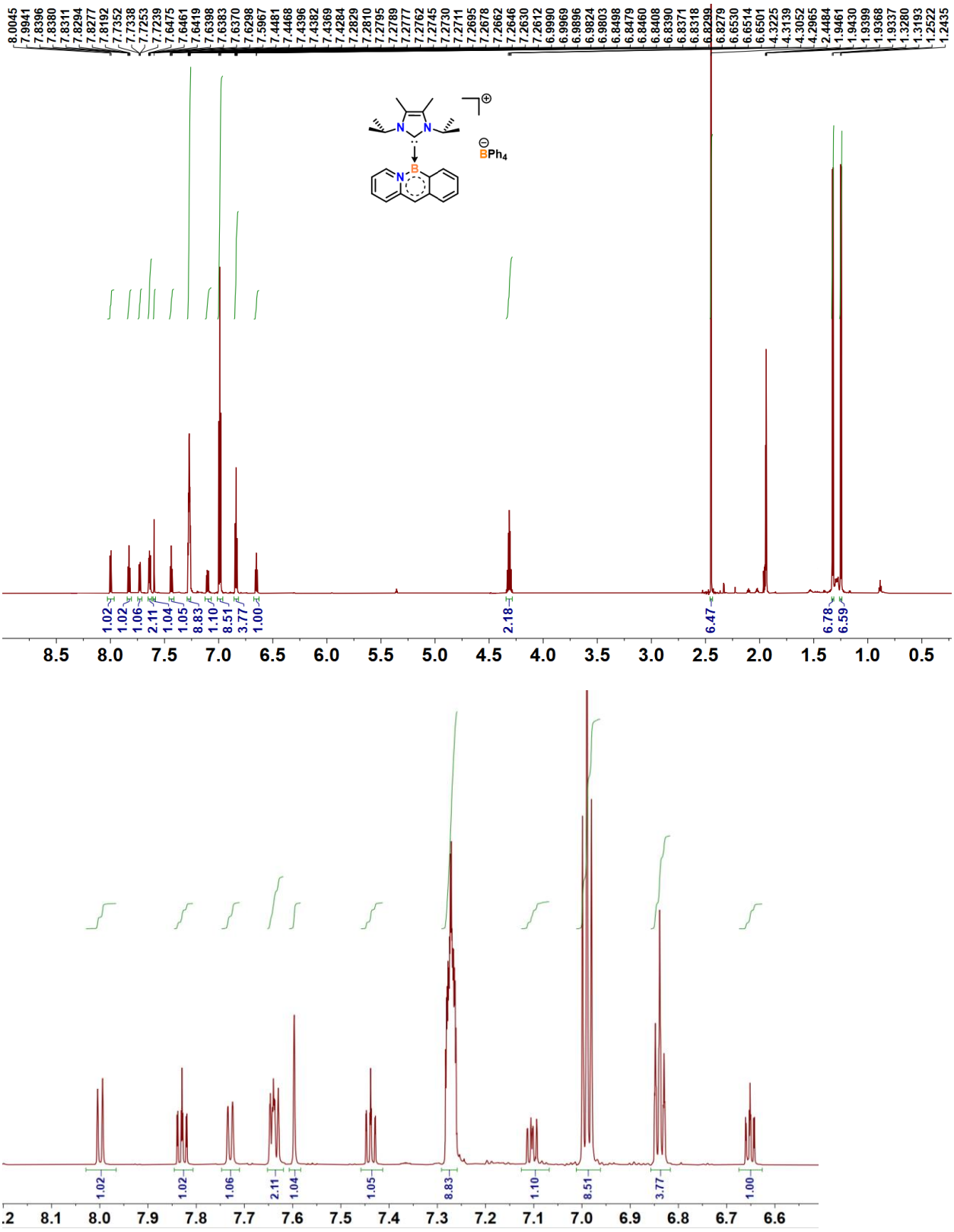

Supplementary Figure 16. ^{1}H NMR (600 MHz, CD_3CN, 25 °C) spectrum for **3a** (top) and its zoomed aromatic region (bottom). NMR solvent contaminate from the vapor (hexanes) in the glove box.

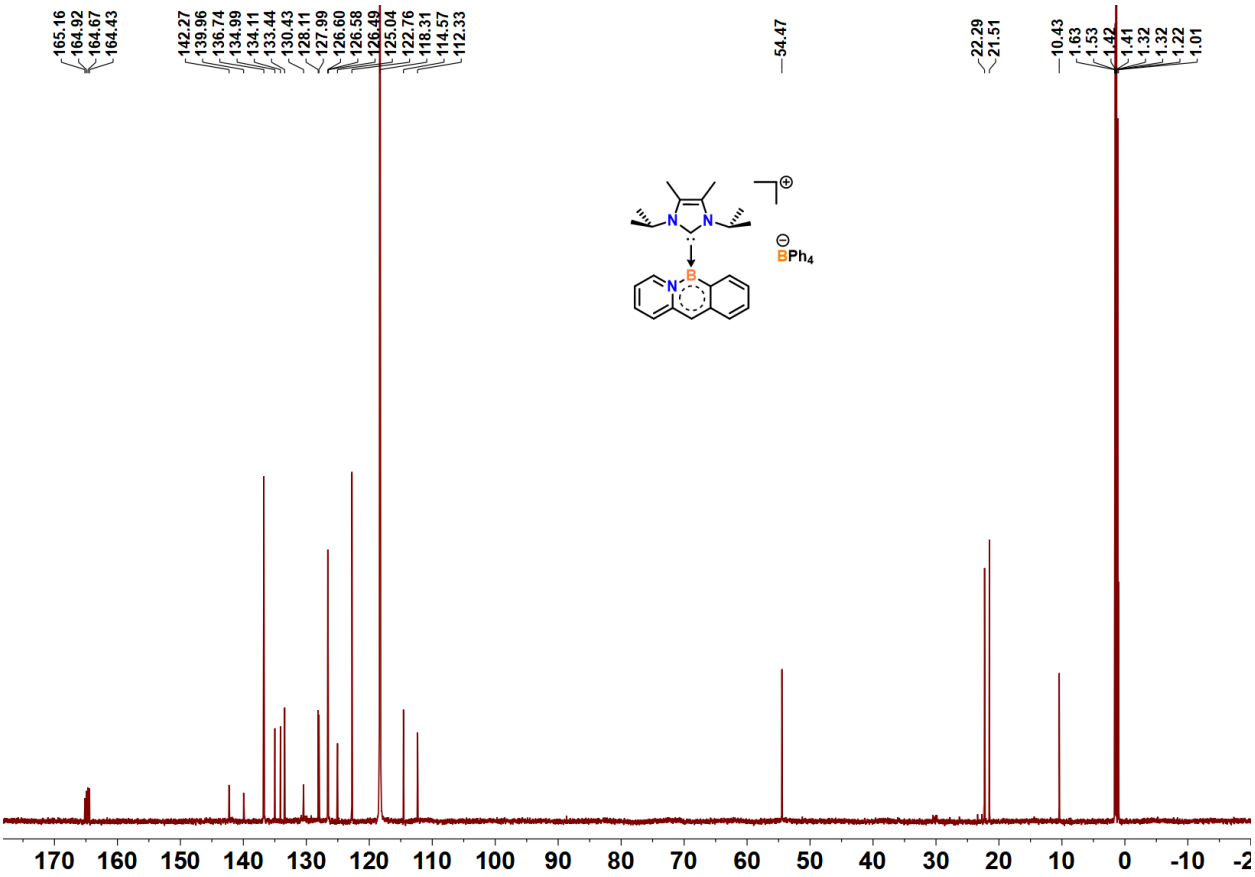

Supplementary Figure 17. ^{13}C NMR (201 MHz, CD_3CN, 25 °C) spectrum for **3a**.

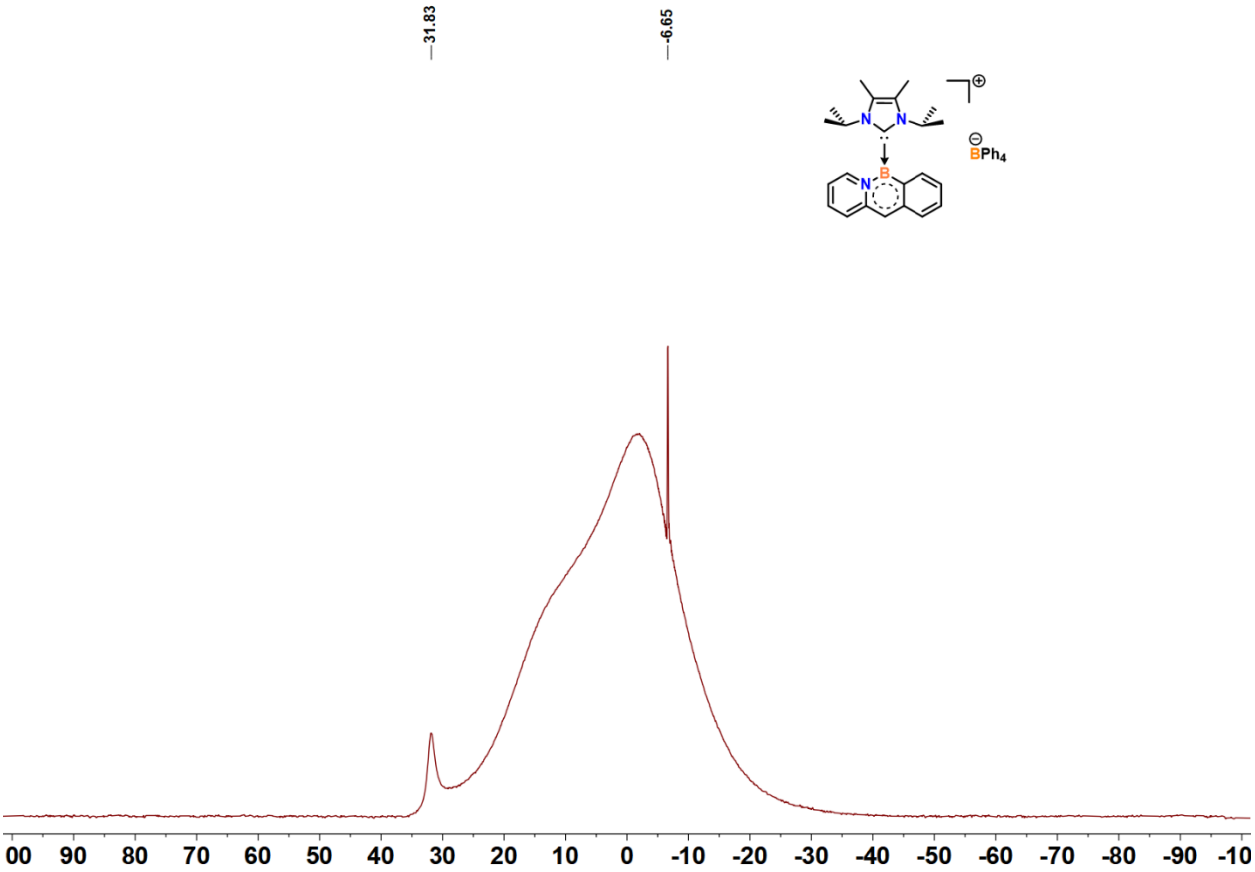

Supplementary Figure 18. $^{11}B\{^{1}H\}$ NMR (192 MHz, CD_3CN, 25 °C) spectrum for **3a**.

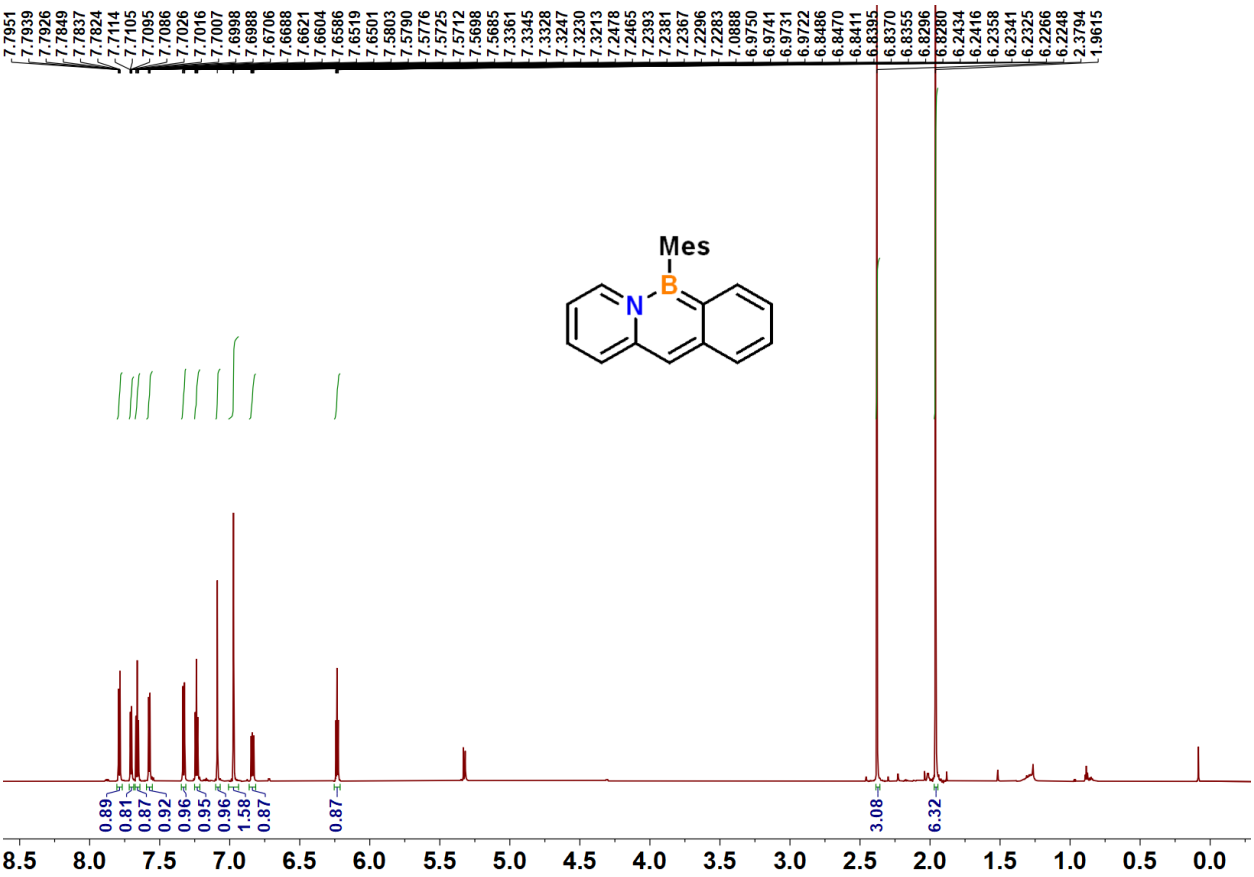

Supplementary Figure 19. ^{11}H NMR (600 MHz, CD_2Cl_2, 25 °C) spectrum for **6a**.

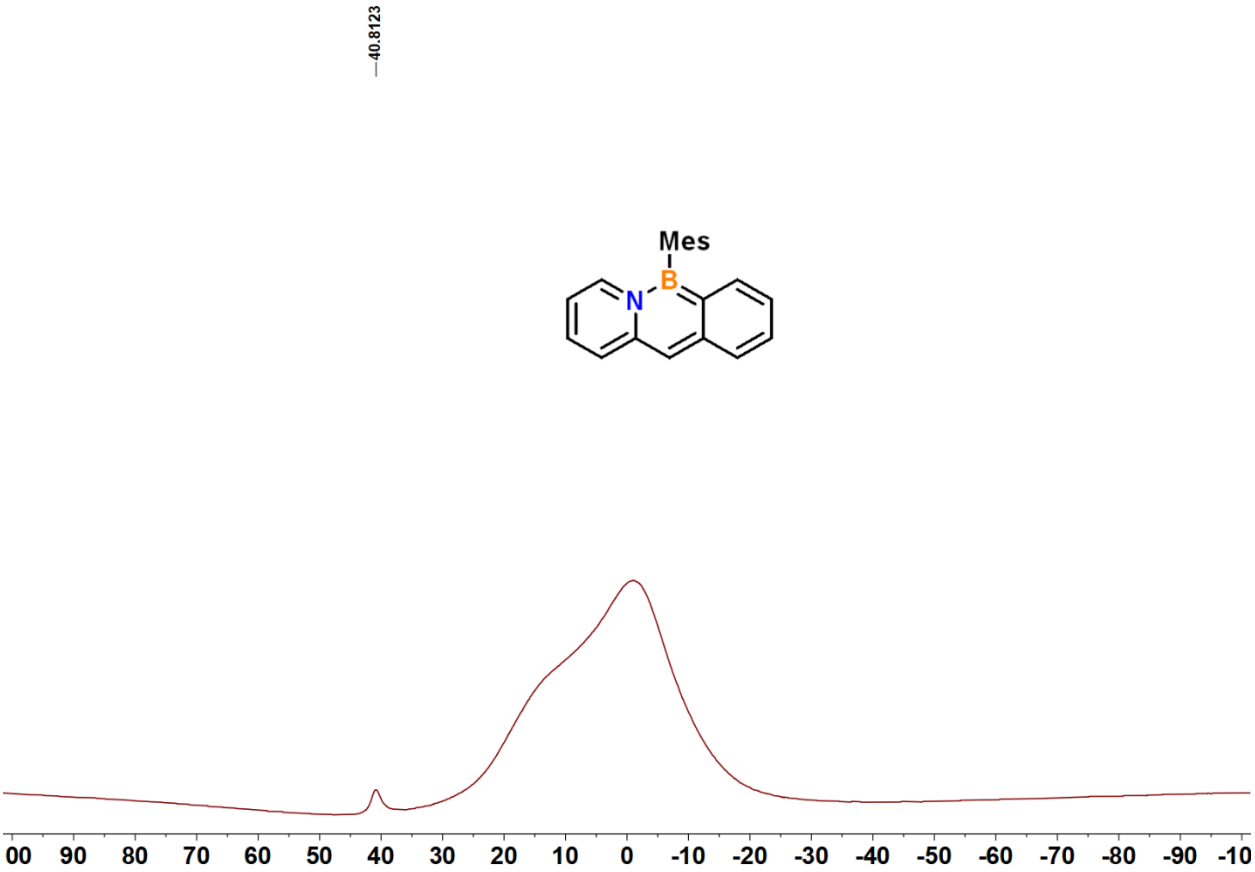

Supplementary Figure 20. $^{11}B\{^{1}H\}$ NMR (192 MHz, CD_2Cl_2, 25 °C) spectrum for **6a**.

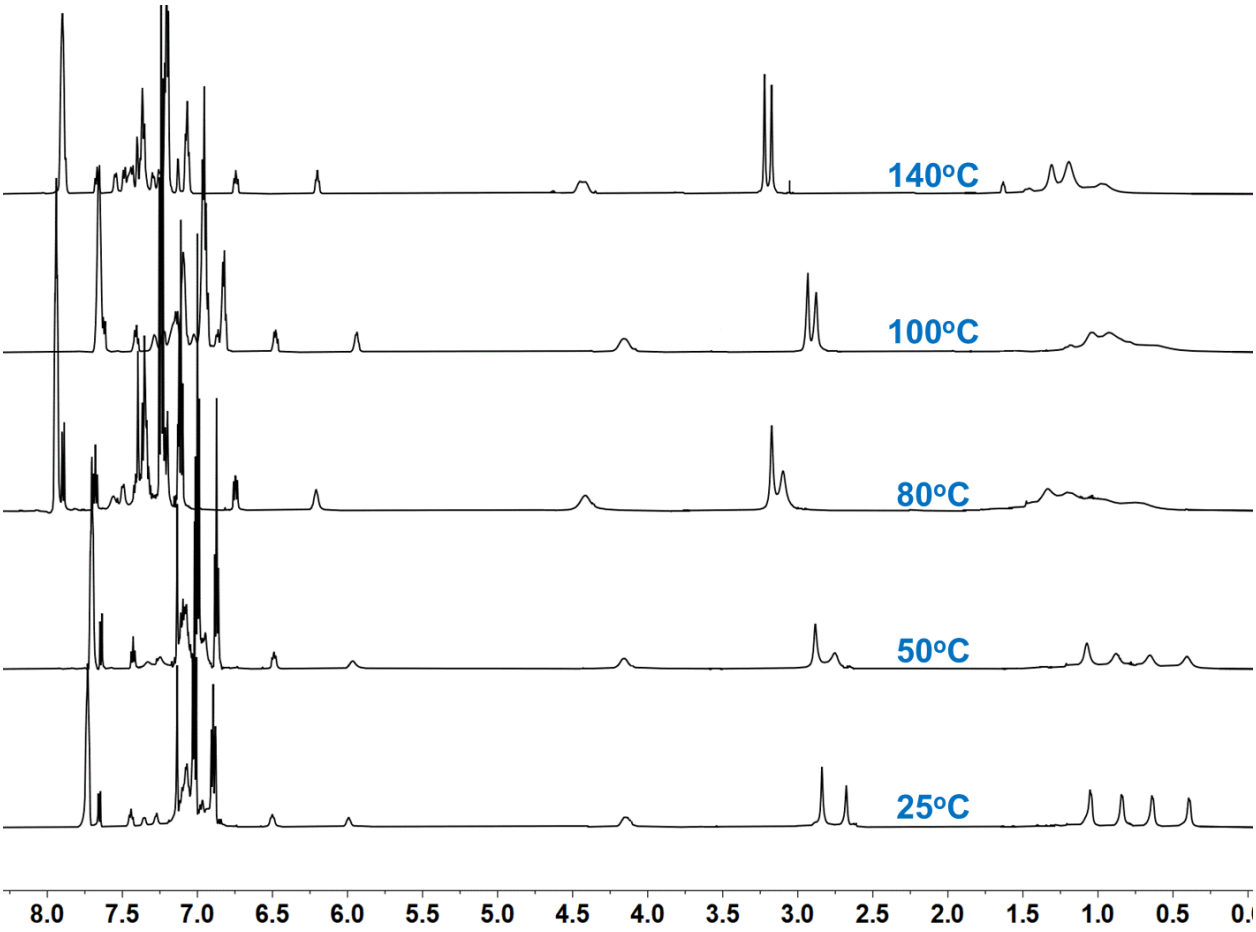

Supplementary Figure 21. Variable temperature ^{1}H NMR (600 MHz, *o*-DCB-d_4) spectra for **1a**. Peaks representing N-CH_3 and N-CH(CH_3)$_2$ protons split into several distinct signals at room temperature resulting from slowed rotation about the $C^{carbone}$–$C^{carbene}$ bond with increased rotation of the $^{carbone}C$–$C^{carbene}$ bonds and all of the respective peaks begin to coalesce at higher temperature and exist as one species. Note that compound **1a** gradually decomposed above 100°C (> 10 min).

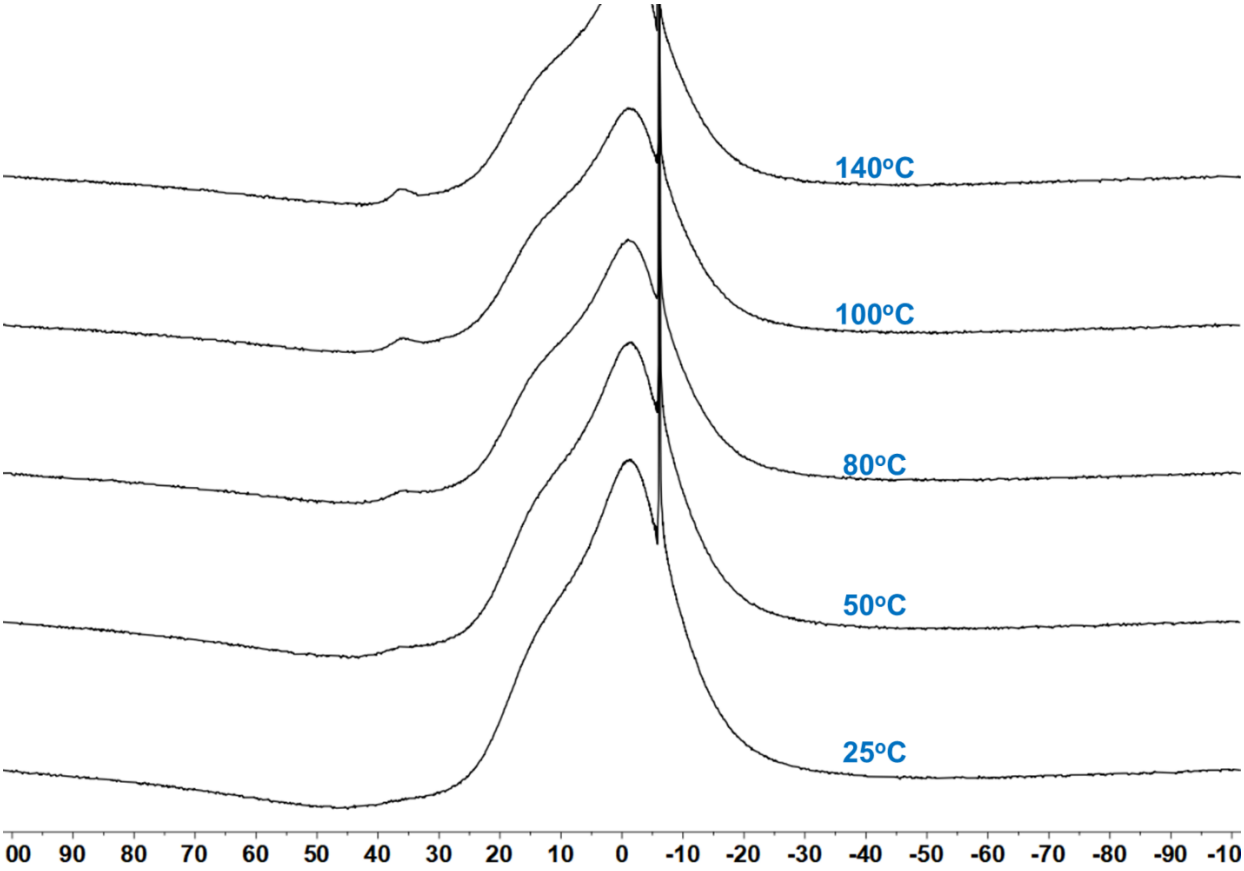

Supplementary Figure 22. Variable temperature ^{11}B NMR (192 MHz, *o*-DCB-d_4) spectra for **1a**.

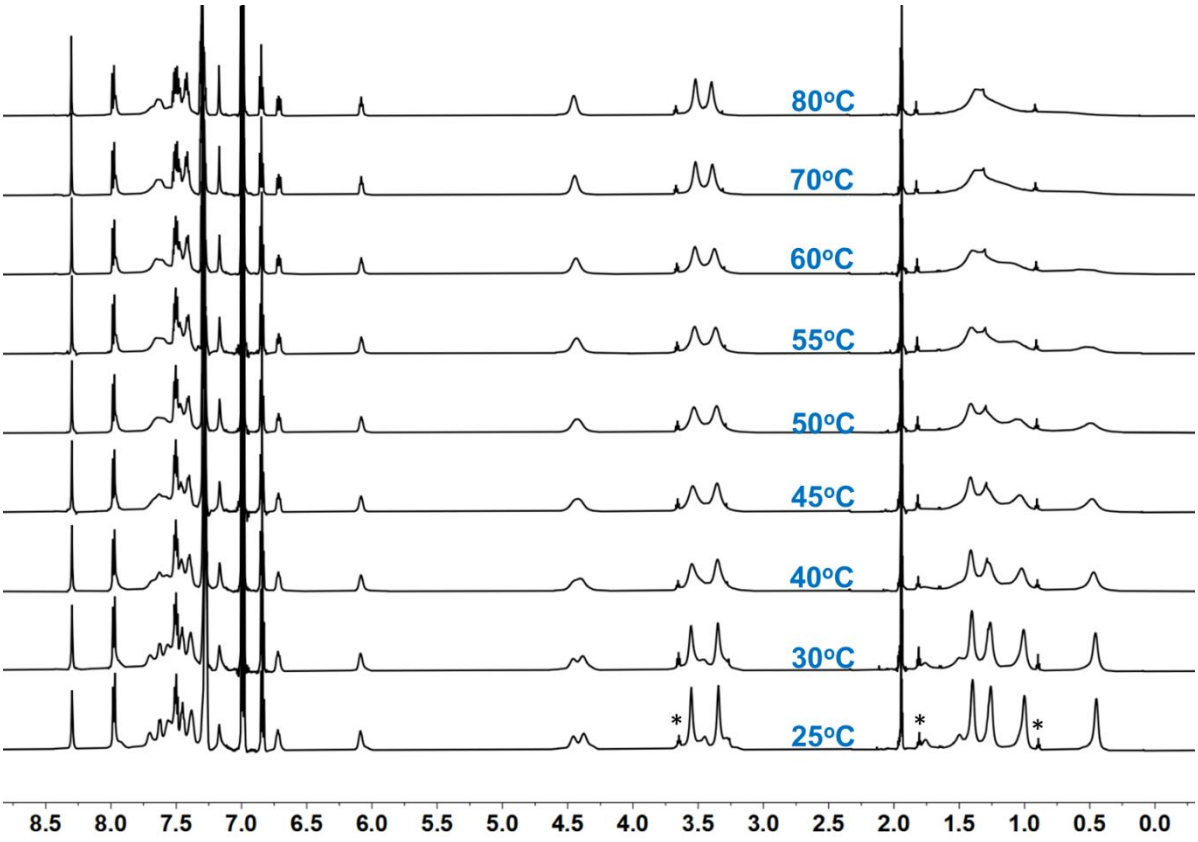

Supplementary Figure 23. Variable temperature ^{1}H NMR (600 MHz, CD_3CN) spectra for **1b**. Peaks representing N-CH_3 and N-CH(CH_3)$_2$ the protons split into several distinct signals at room temperature resulting from slowed rotation about the $C^{carbone}$–$C^{carbene}$ bond with increased rotation of the $^{carbone}C$–$C^{carbene}$ bonds and all of the respective peaks begin to coalesce at higher temperature, suggesting the presence of one species. CD_3CN was chosen as the NMR solvent for study. When *o*-DCB-d_4 was used as the NMR solvent, it was challenging to observe changes in peak splitting for the alkyl region. (*) Solvent residues (THF/hexanes) from recrystallization.

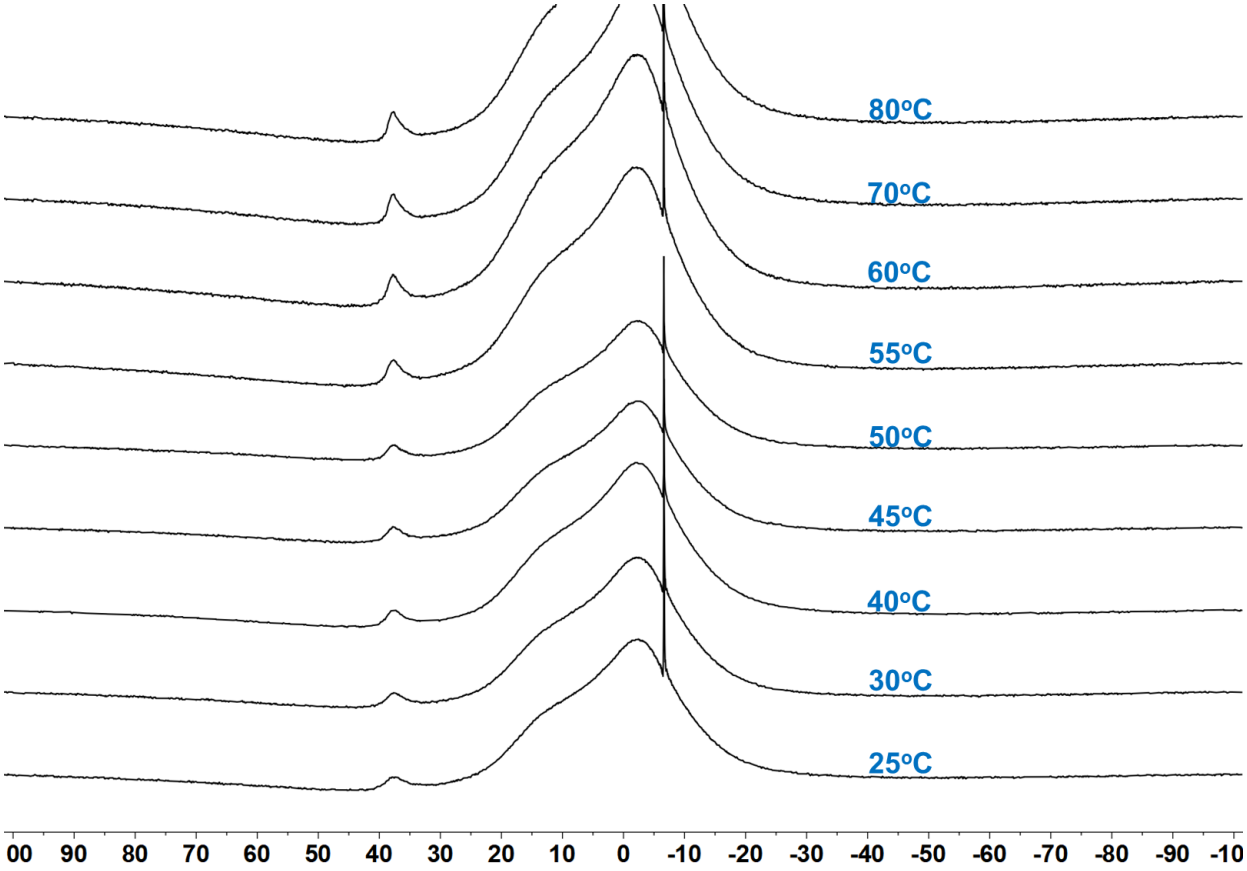

Supplementary Figure 24. Variable temperature ^{11}B NMR (192 MHz, CD_3CN) spectra for **1b**.

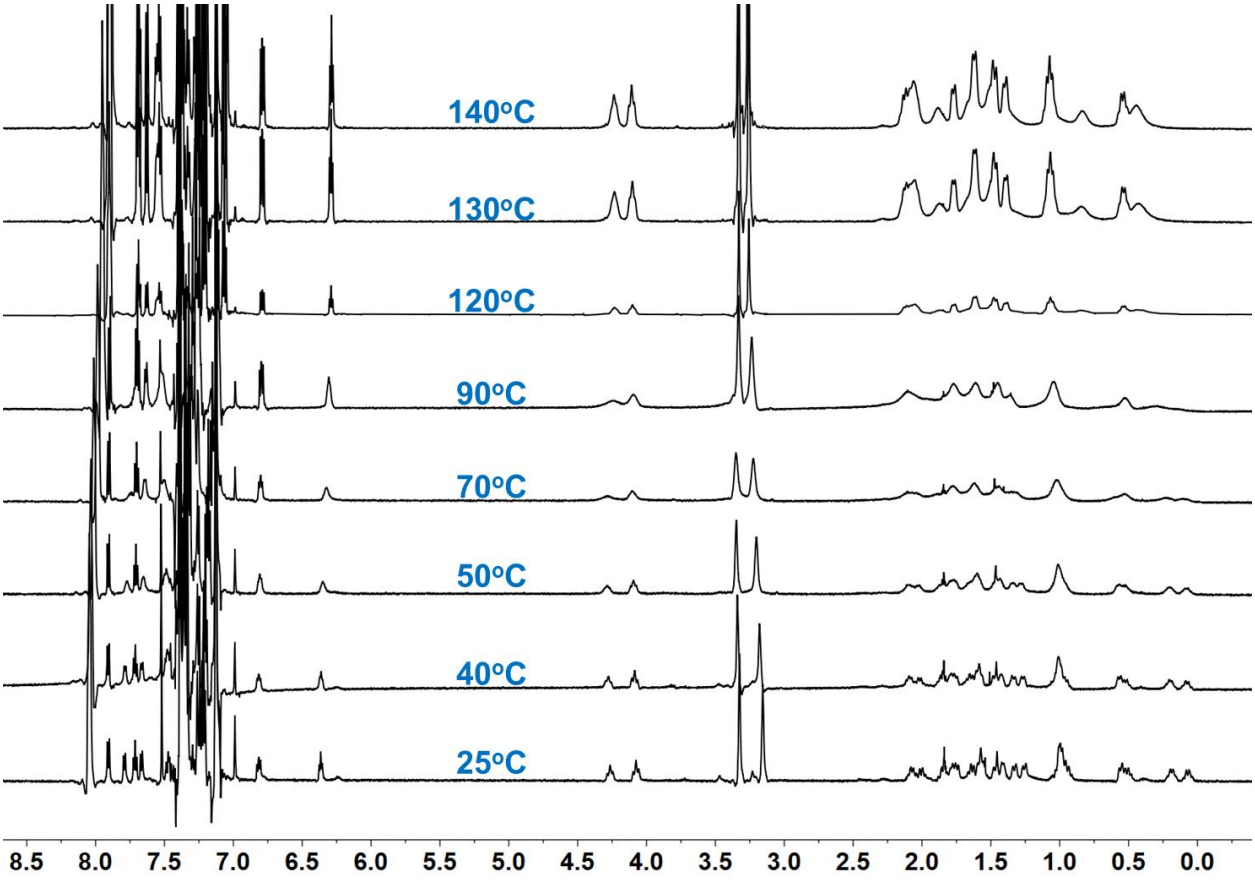

Supplementary Figure 25. Variable temperature ^{1}H NMR (600 MHz, *o*-DCB-d_4) spectra for **2a**.

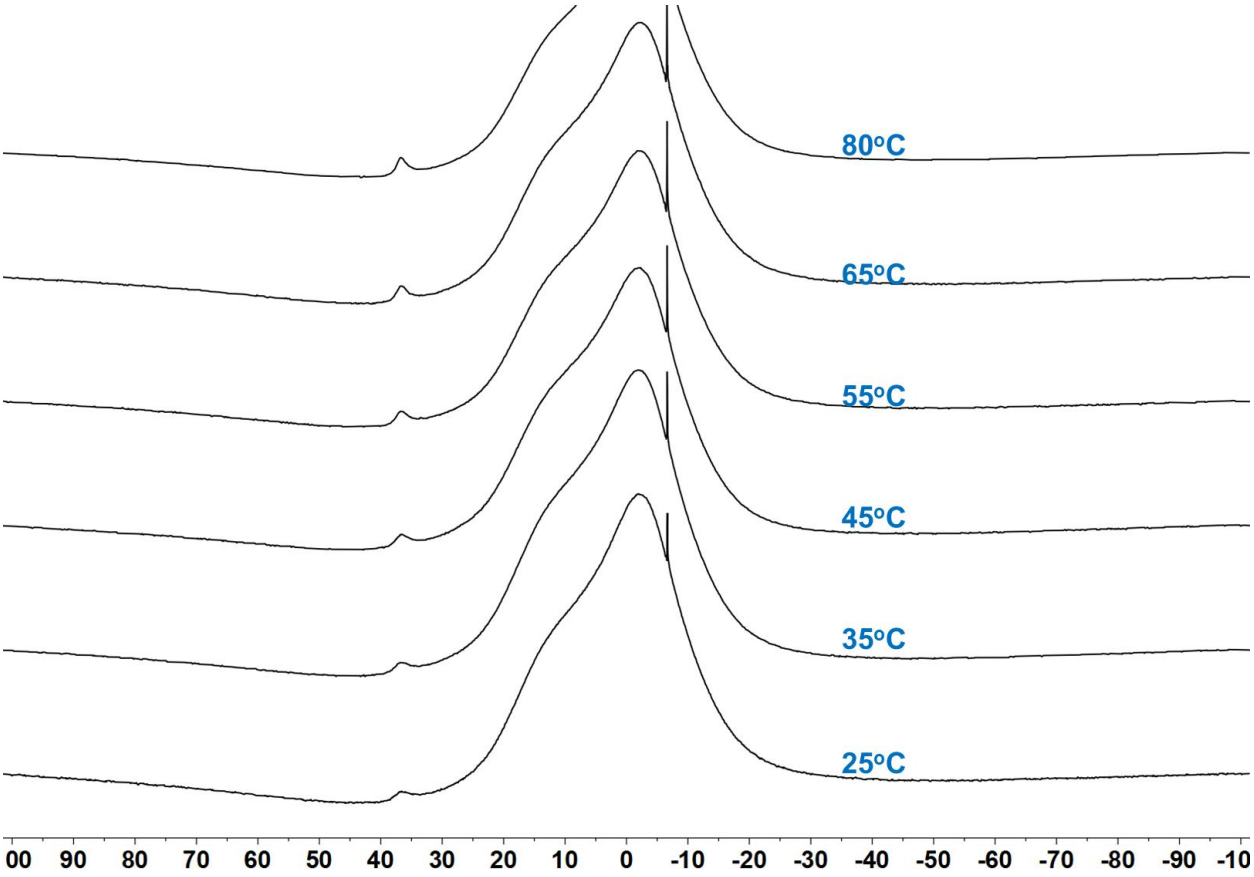

Supplementary Figure 26. Variable temperature ^{11}B NMR (192 MHz, CD_3CN) spectra for **2a**. The ^{11}B-NMR signals could not be detected in *o*-DCB-d_4 due to the limited solubility of **2a**.

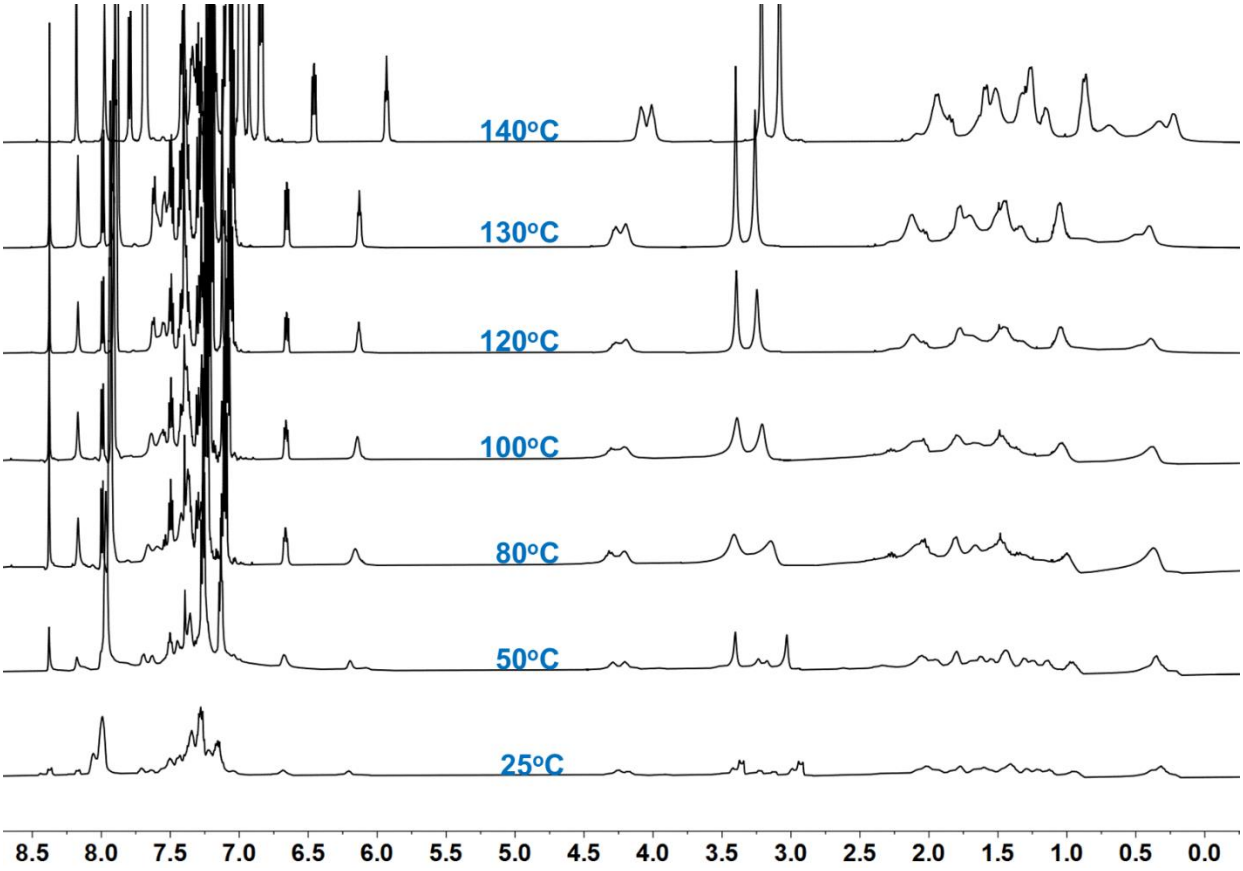

Supplementary Figure 27. Variable temperature ^{1}H NMR (600 MHz, *o*-DCB-d_4) spectra for **2b**. The solubility of **2b** in *o*-DCB-d_4 is limited at 25 ^{o}C.

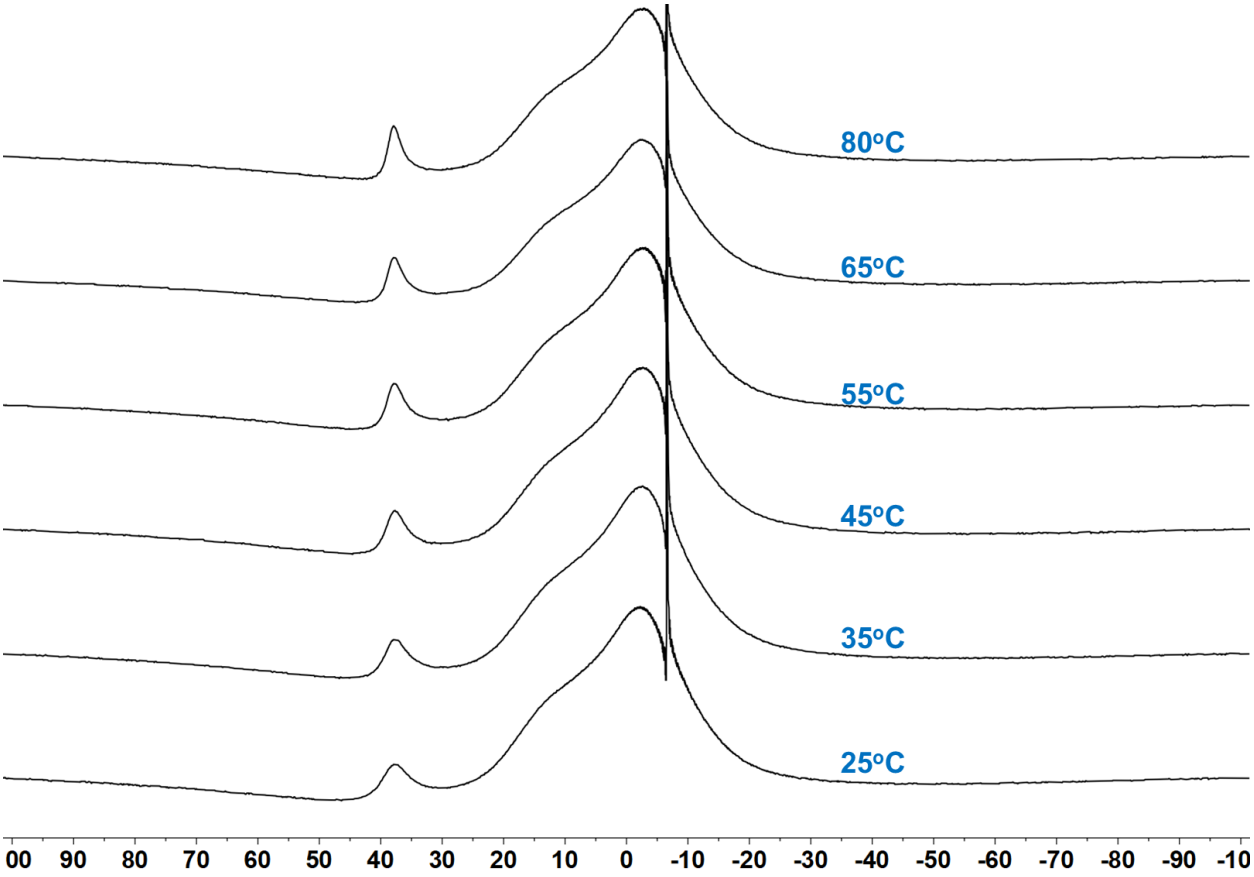

Supplementary Figure 28. Variable temperature ^{11}B NMR (192 MHz, CD_3CN) spectra for **2b**. The ^{11}B-NMR signals could not be detected in *o*-DCB-d_4 due to the limited solubility of **2b**.

Photophysical Data

All steady-state spectra were obtained using an Agilent Cary Eclipse Fluorescence spectrophotometer equipped with the photomultiplier tube (PMT) detector. Absolute fluorescence quantum yields were determined using a Hamamatsu C11347-11 Quantaurus-QY Absolute PL Quantum Yield Spectrometer. Samples were prepared inside the glovebox in quartz Petri dishes (solid sample) or 1 cm square quartz cuvettes (solutions). Solutions were prepared in toluene and data were collected with absorbance values below 0.05. Time-correlated single photon counting (TCSPC) was employed to obtain all fluorescence lifetime spectra, which was achieved with an Edinburgh Instruments FS5 spectrofluorometer equipped with pulsed LEDs at 340 nm. The signal level was kept below 5% of the light source repetition rate. Instrument response functions (IRF) were determined from the scatter signal solution of Ludox HS-40 colloidal silica (~1% particles in water w/w). The decay traces analysis was performed using the Fluoracle software (Edinburgh Instruments) and fitted with the mono-exponential function and/or multi-exponential decay function. The quality of fit was judged on the basis of the reduced *chi*-square statistic, χ^2, and the randomness of residuals.

Supplementary Table 1. Summary of QYs, lifetimes, and decay rate constants for **1**, **2** and **3a** in toluene at 298 K (under Argon).

Compound	**1a**	**1b**	**2a**	**2b**	**3a**
Φ_F[a]	0.53	0.29	0.62	0.34	0.31
τ/ns[b]	2.9	4.6	5.4	5.2	6.2
$k_r/\times10^8 s^{-1}$[c]	1.83	0.63	1.15	0.65	0.50
$k_{nr}/\times10^8 s^{-1}$ [c]	1.62	1.54	0.68	1.26	1.11

[a] Absolute QYs.
[b] Lifetime values were collected at λ_{ex} = 340 nm.
[c] Radiative constant $k_r = \Phi_F/\tau$, non-radiative constant $k_{nr} = (1-\Phi_F)/\tau$.

Supplementary Table 2. Summary of QYs, lifetimes, and decay rate constants for **1** and **2** in 2-MeTHF at 77 K (data at 298 K in 2-MeTHF are given in parentheses).

Compound	**1a**	**2a**	**1b**	**2b**
Φ_F[a]	0.88 (0.16)	0.98(0.30)	0.35(0.19)	0.32(0.23)
τ/ns[b]	11.7 (4.3)	12.2(6.5)	5.1(4.7)	6.0(5.4)
$k_r/\times10^8 s^{-1}$[c]	0.75 (0.37)	0.80 (0.46)	0.69 (0.40)	0.53(0.42)
$k_{nr}/\times10^8 s^{-1}$ [c]	0.18 (1.95)	0.02(1.08)	1.27 (1.72)	1.13(1.43)

[a] Absolute QYs.
[b] Lifetime values were collected at λ_{ex} = 340 nm.
[c] Radiative constant $k_r = \Phi_F/\tau$, non-radiative constant $k_{nr} = (1-\Phi_F)/\tau$.

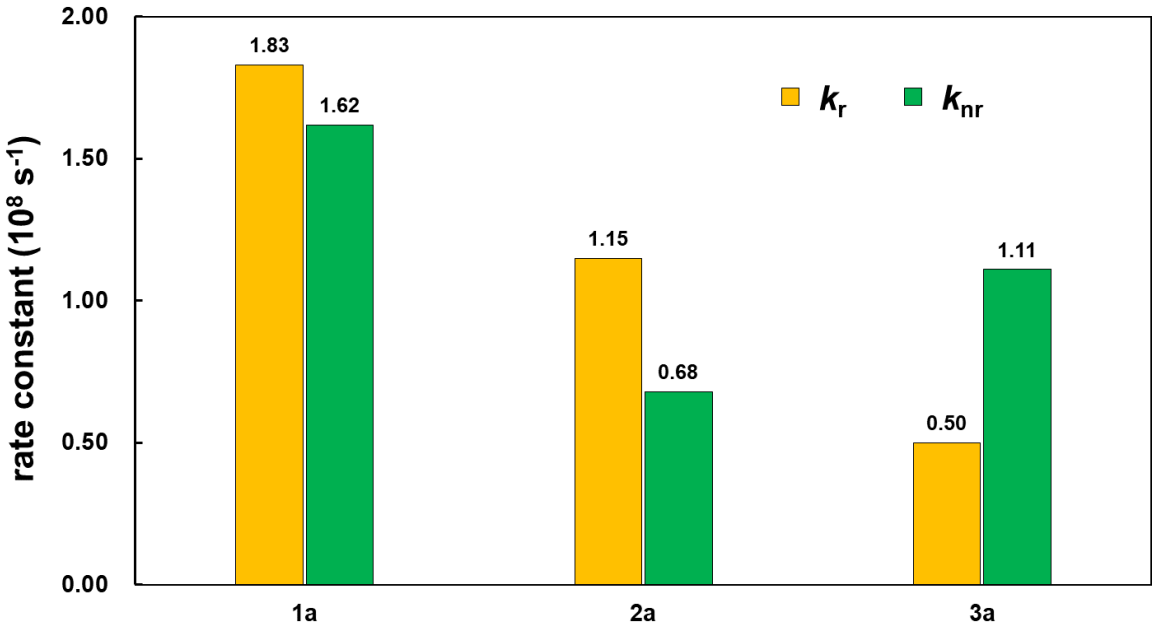

Supplementary Figure 29. Rate constants of radiative k_r (orange) and non-radiative decay k_{nr} (green) of azaboraanthracenium ions **1a**, **2a** and **3a** in toluene at 298 K.

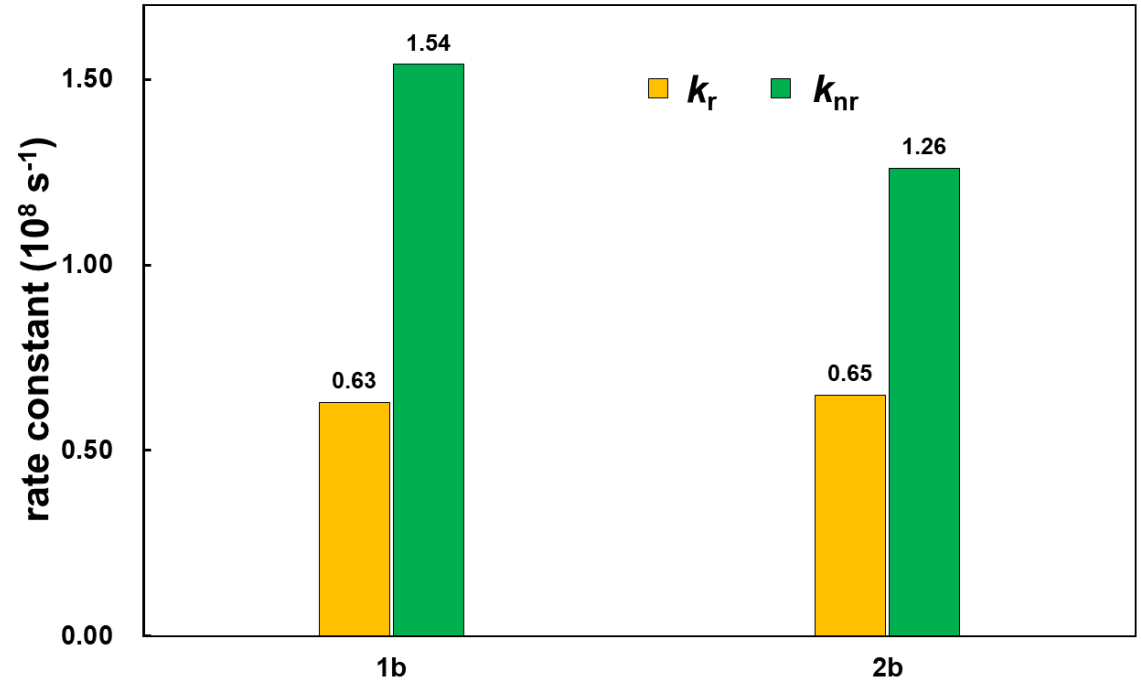

Supplementary Figure 30. Rate constants of radiative k_r (orange) and non-radiative decay k_{nr} (green) of azaboratetracenium ions **1b** and **2b** in toluene at 298 K.

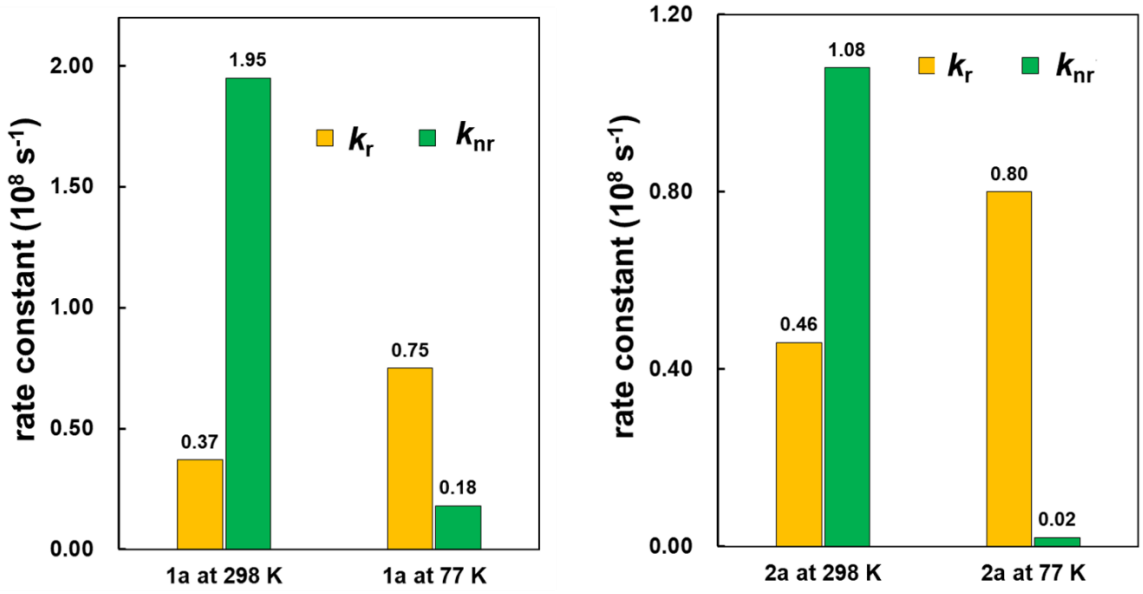

Supplementary Figure 31. Rate constants of radiative k_r (orange) and non-radiative decay k_{nr} (green) of azaboraanthracenium ions **1a** (left) and **2a** (right) in 2-MeTHF at 298 K and 77 K.

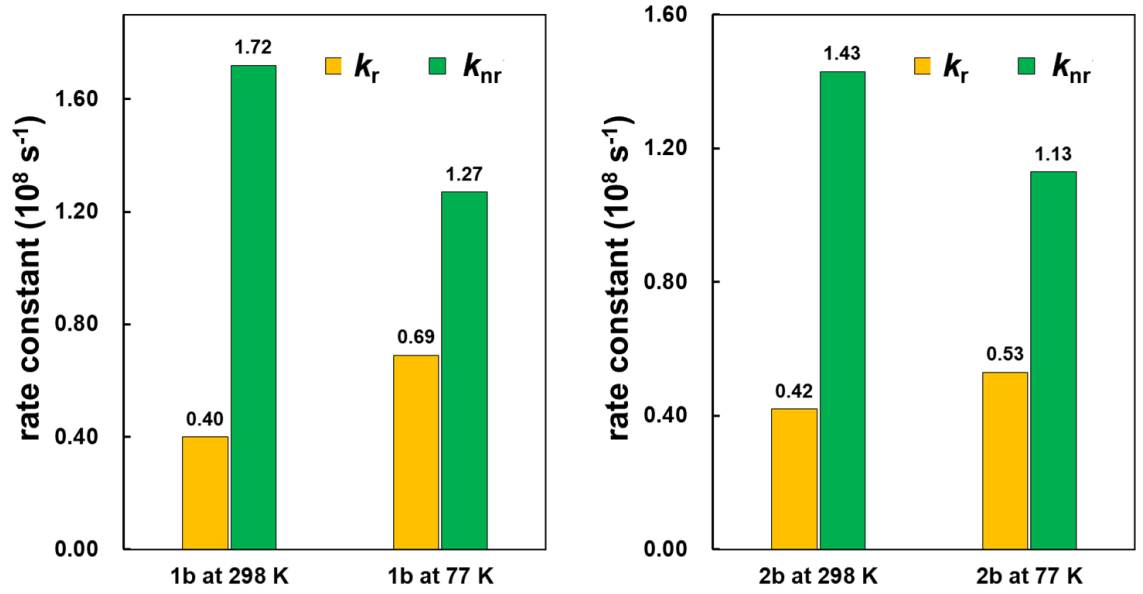

Supplementary Figure 32. Rate constants of radiative k_r (orange) and non-radiative decay k_{nr} (green) of azaboratetracenium ions **1b** (left) and **2b** (right) in 2-MeTHF at 298 K and 77 K.

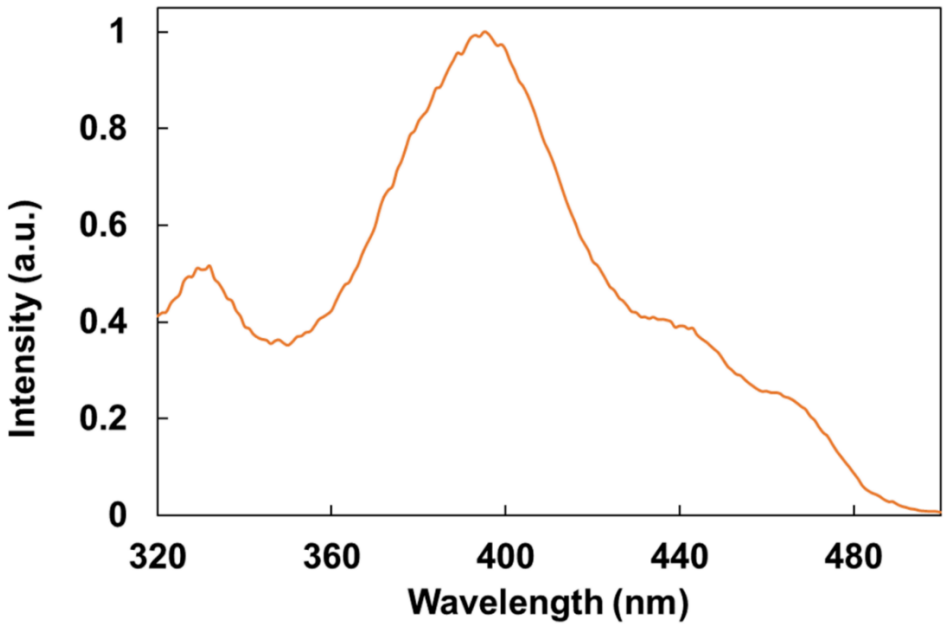

Supplementary Figure 33. Fluorescence excitation spectrum of **1a** in toluene at 298 K.

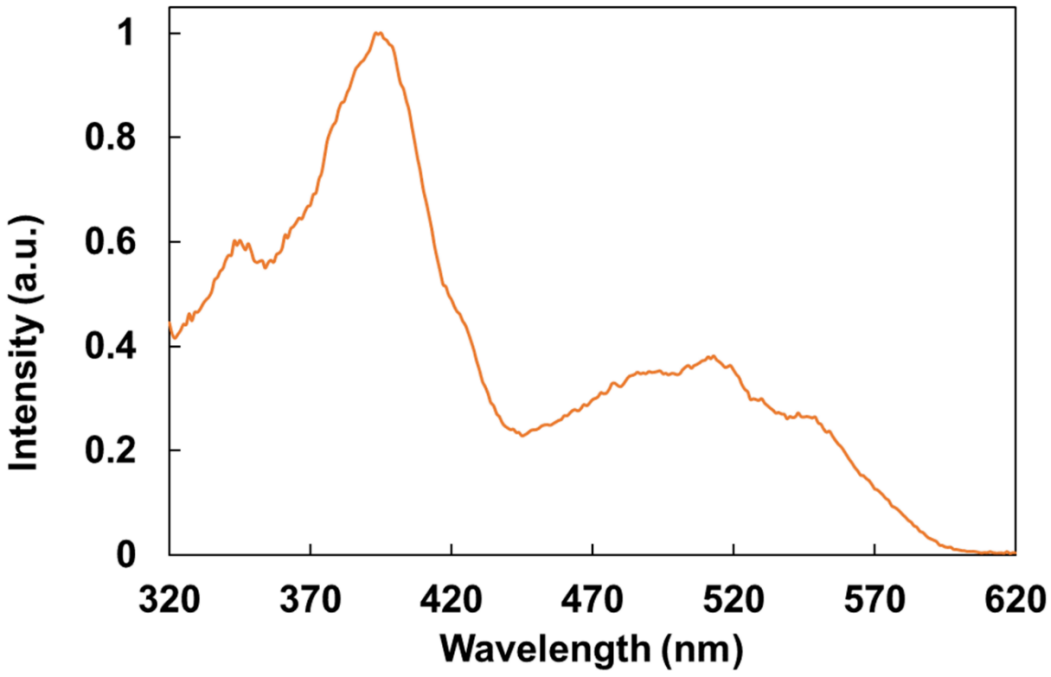

Supplementary Figure 34. Fluorescence excitation spectrum of **1b** in toluene at 298 K.

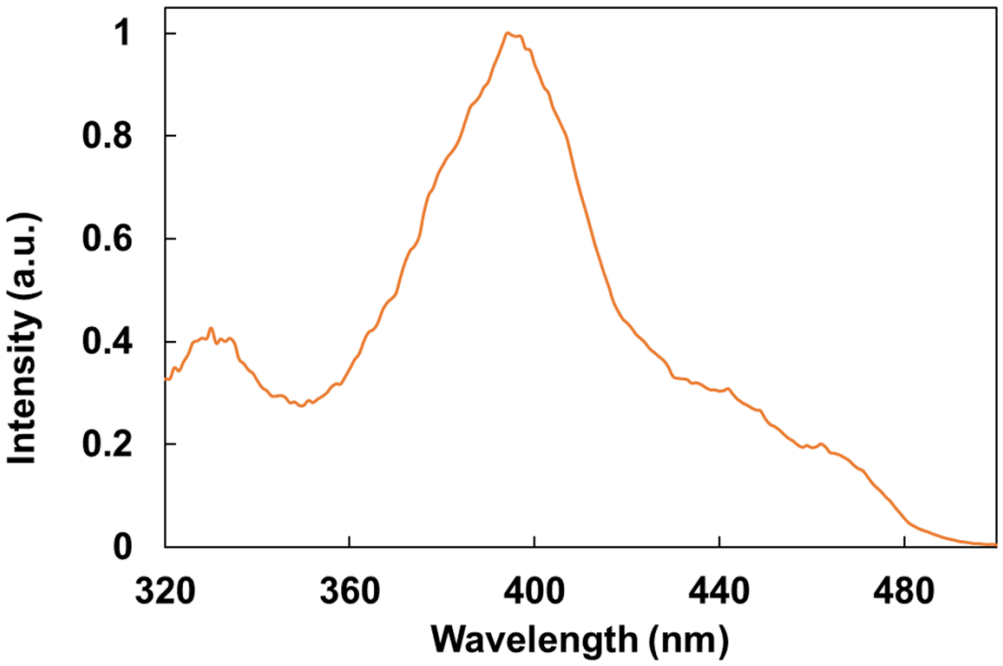

Supplementary Figure 35. Fluorescence excitation spectrum of **2a** in toluene at 298 K.

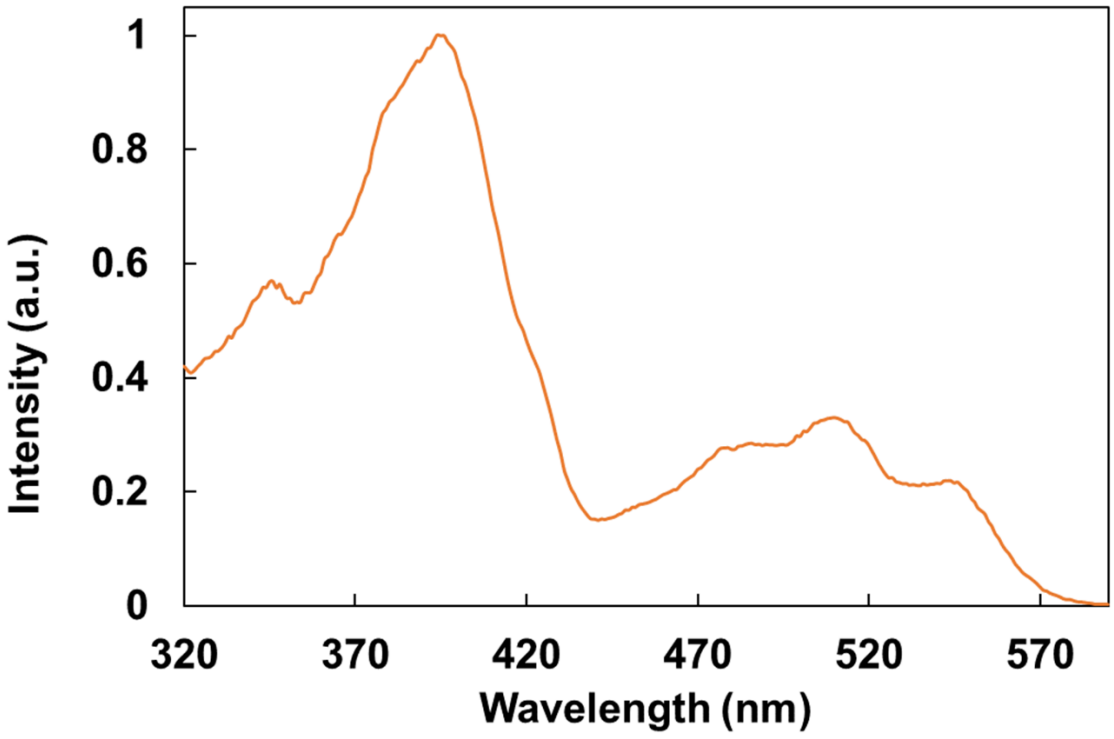

Supplementary Figure 36. Fluorescence excitation spectrum of **2b** in toluene at 298 K.

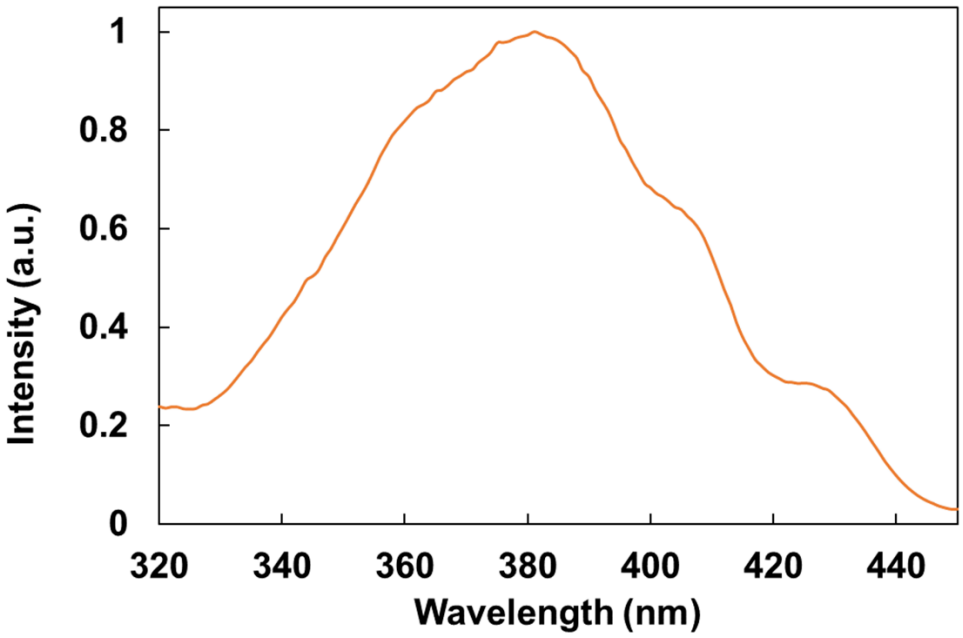

Supplementary Figure 37. Fluorescence excitation spectrum of **3a** in toluene at 298 K.

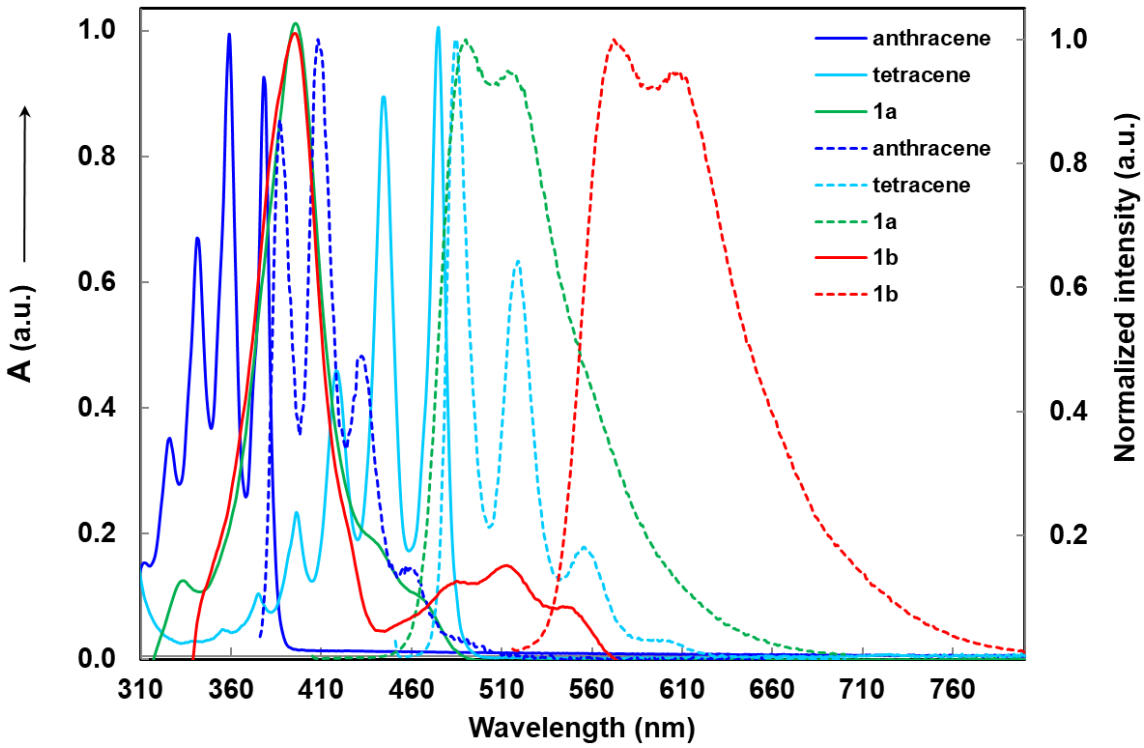

Supplementary Figure 38. UV–vis absorption (solid line) and fluorescence (dash line) spectra of anthracene, tetracene, **1a** and **1b** in toluene under argon at 298 K.

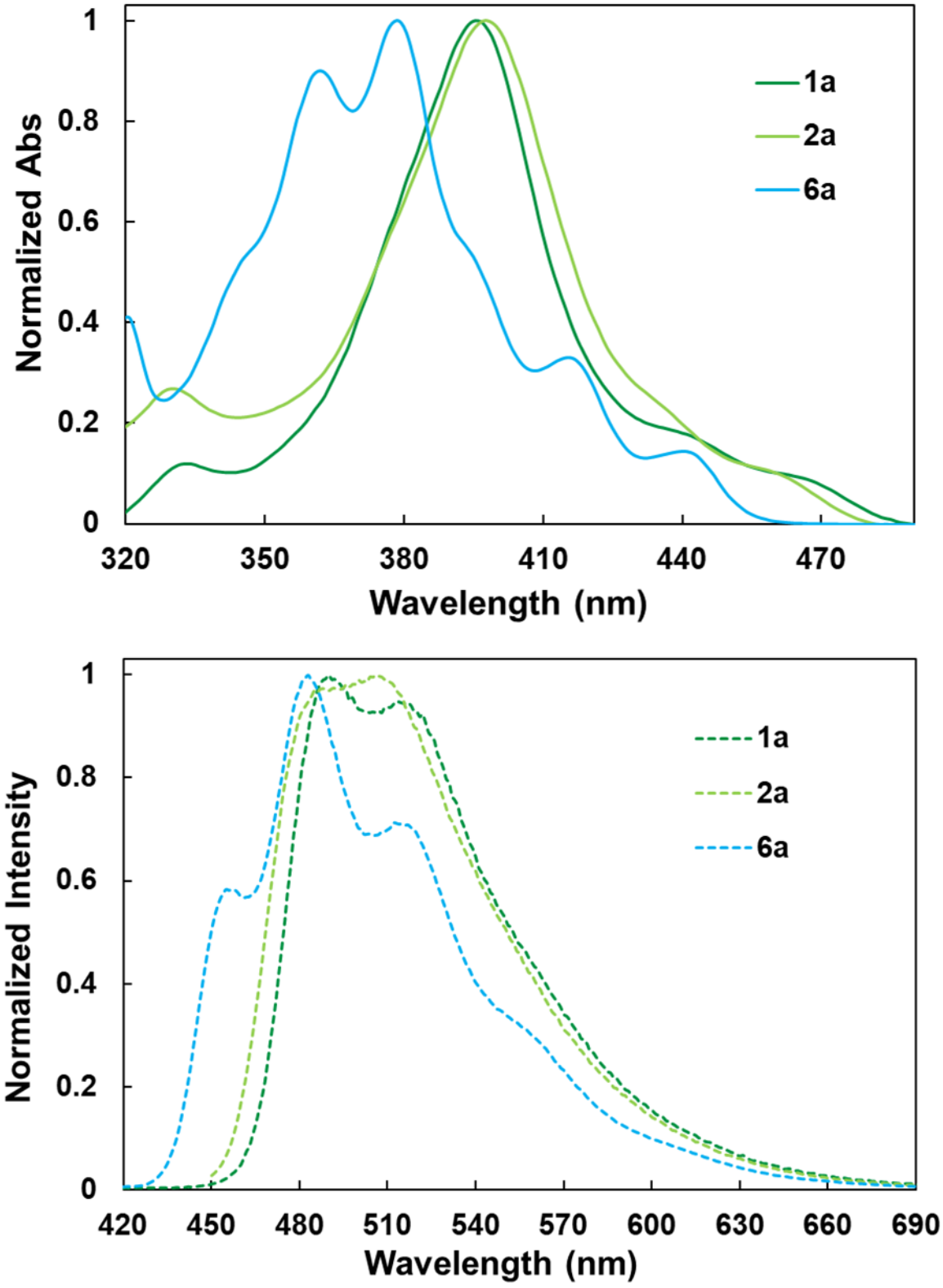

Supplementary Figure 39. Comparison of UV-vis absorption (top) and fluorescence (bottom) spectra of **1a**, **2a** and **6a** in toluene at 298 K.

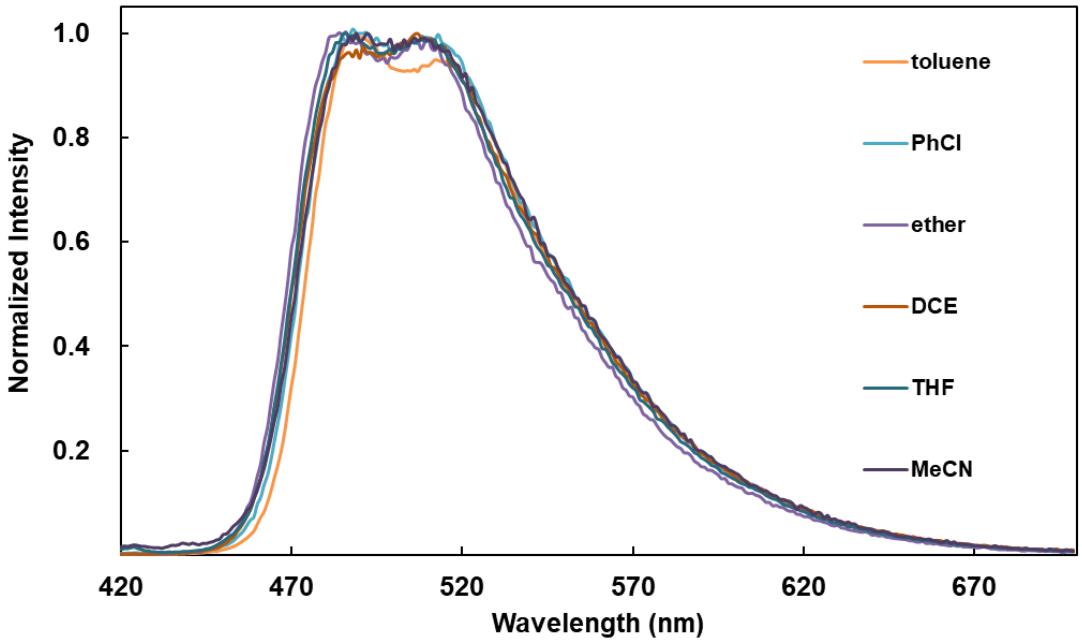

Supplementary Figure 40. Fluorescence spectra of **1a** in various solvents at 298 K. In polar solvents, the vibronic coupling gets weakened.

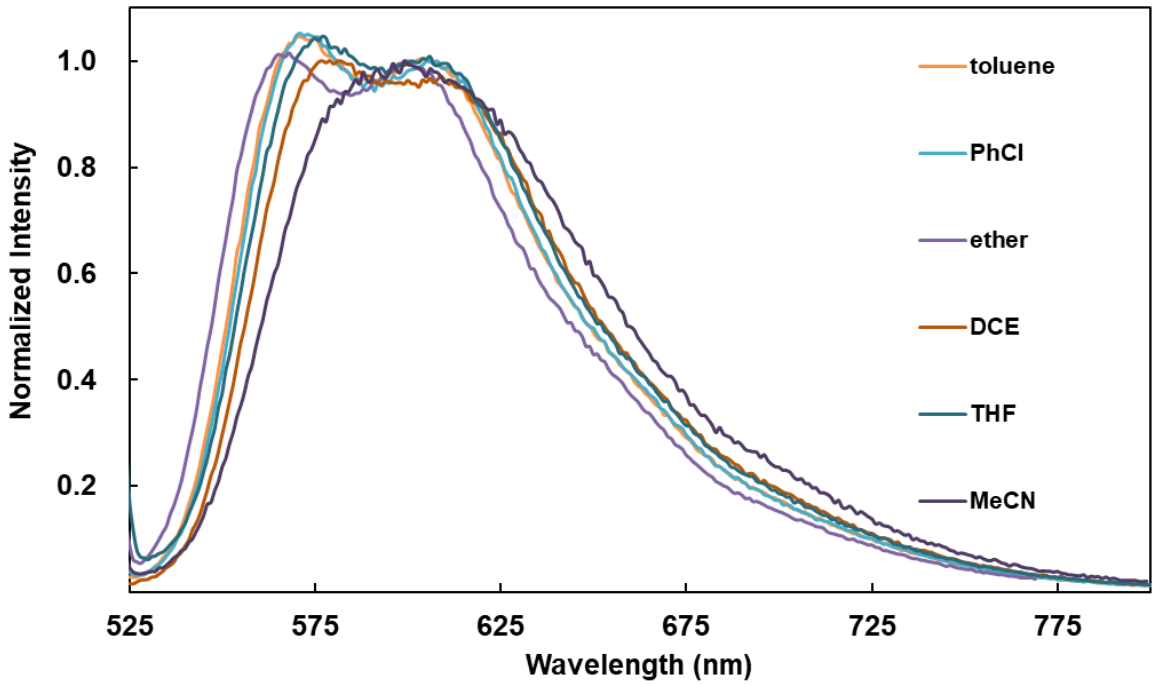

Supplementary Figure 41. Fluorescence spectra of **1b** in various solvents at 298 K. In polar solvents, the vibronic coupling gets weakened.

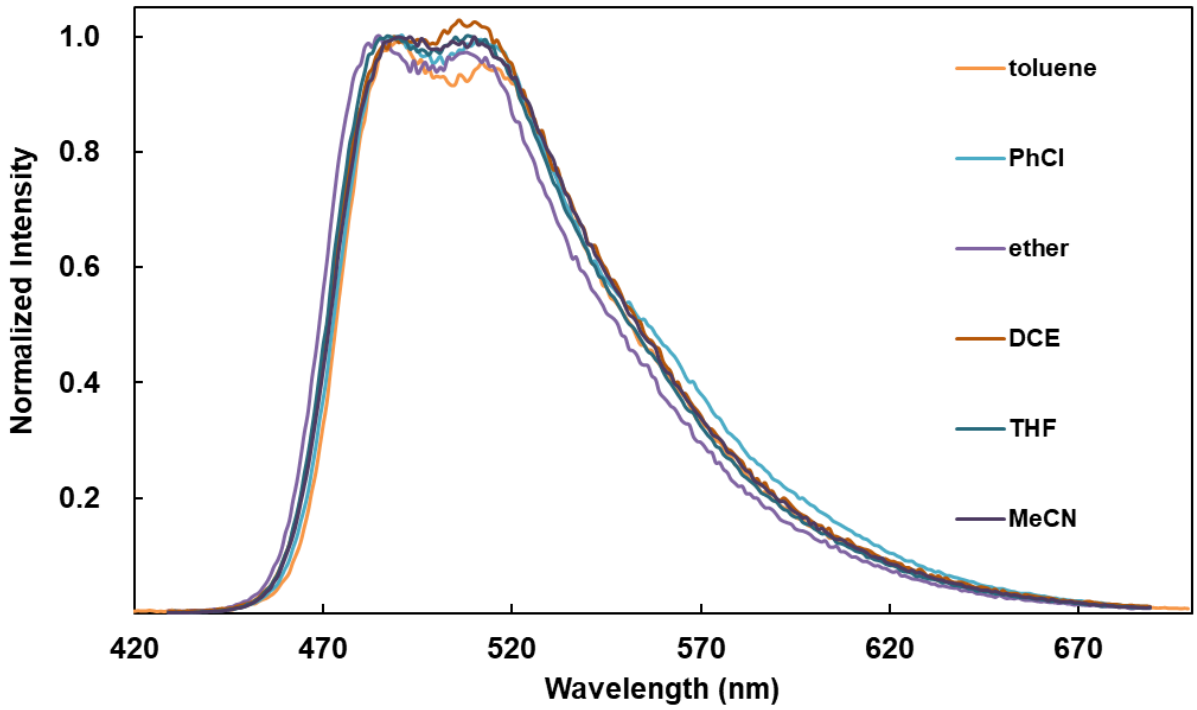

Supplementary Figure 42. Fluorescence spectra of **2a** in various solvents at 298 K.

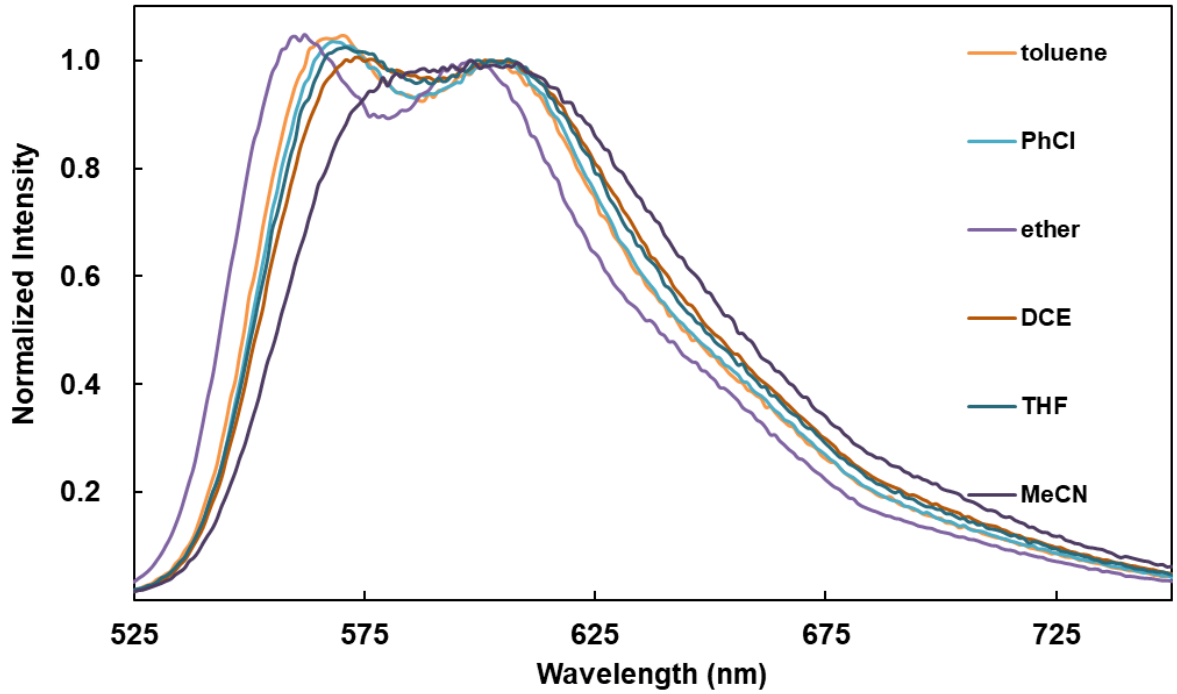

Supplementary Figure 43. Fluorescence spectra of **2b** in various solvents at 298 K.

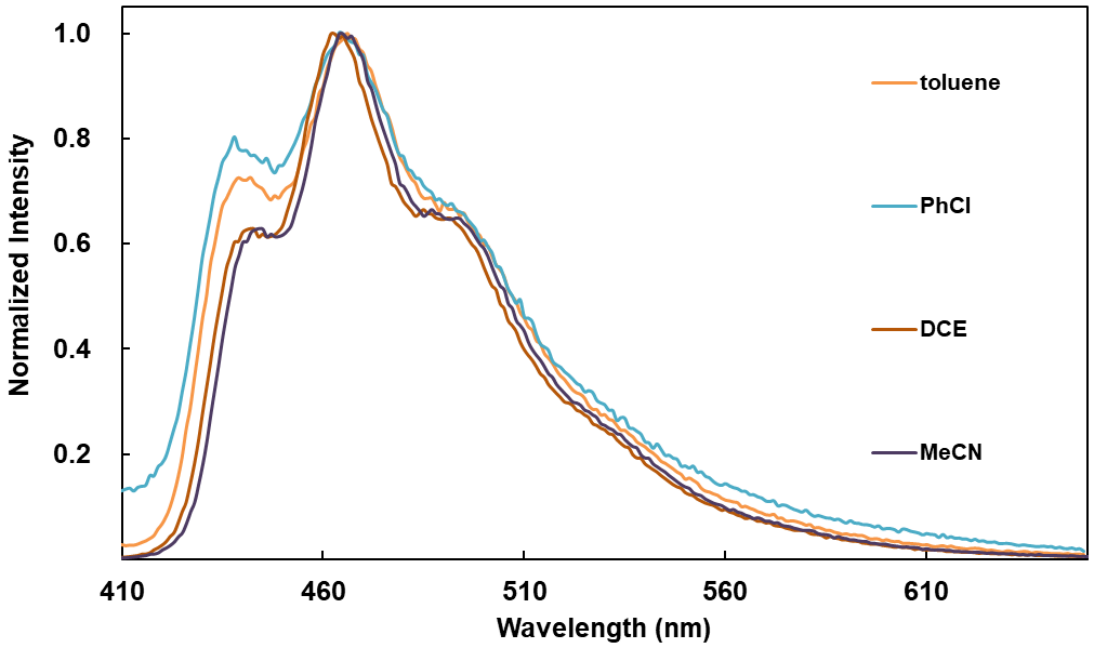

Supplementary Figure 44. Fluorescence spectra of **3a** in various solvents (compound **3a** reacted/activated ether-like solvents ether and THF, 2-MeTHF) at 298 K.

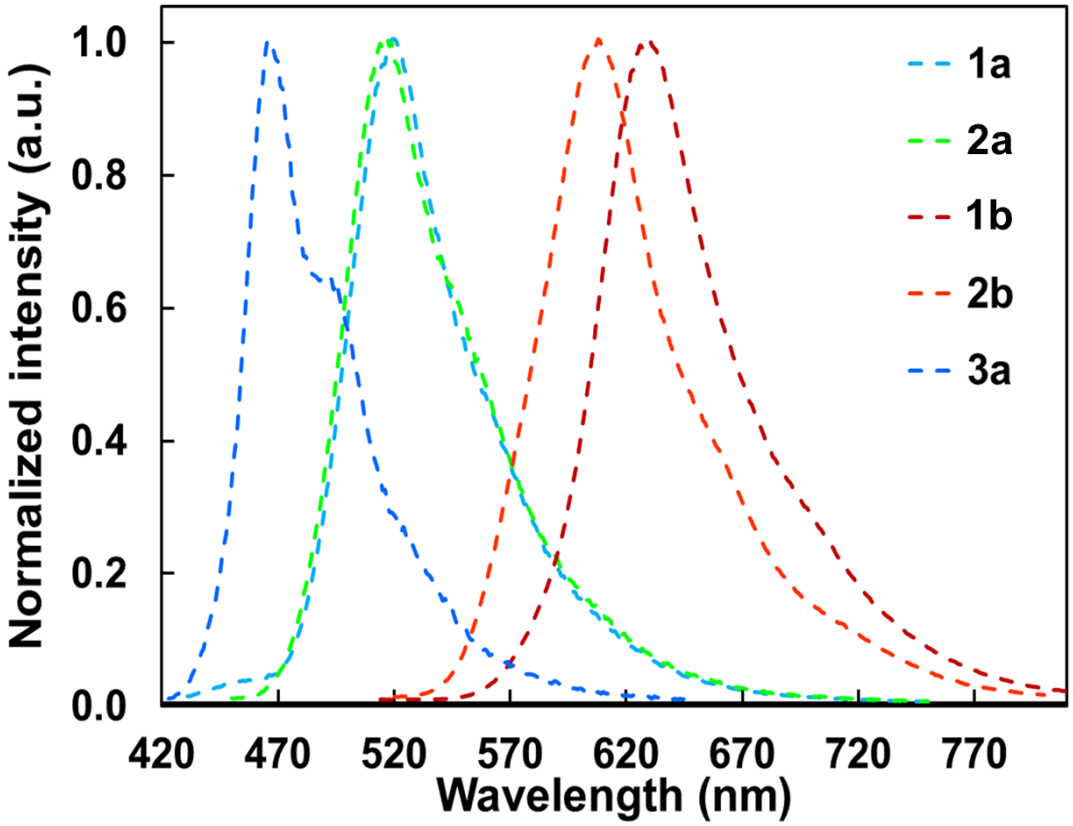

Supplementary Figure 45. Solid fluorescence spectra of **1**, **2** and **3a (**in crystalline states, at 298 K).

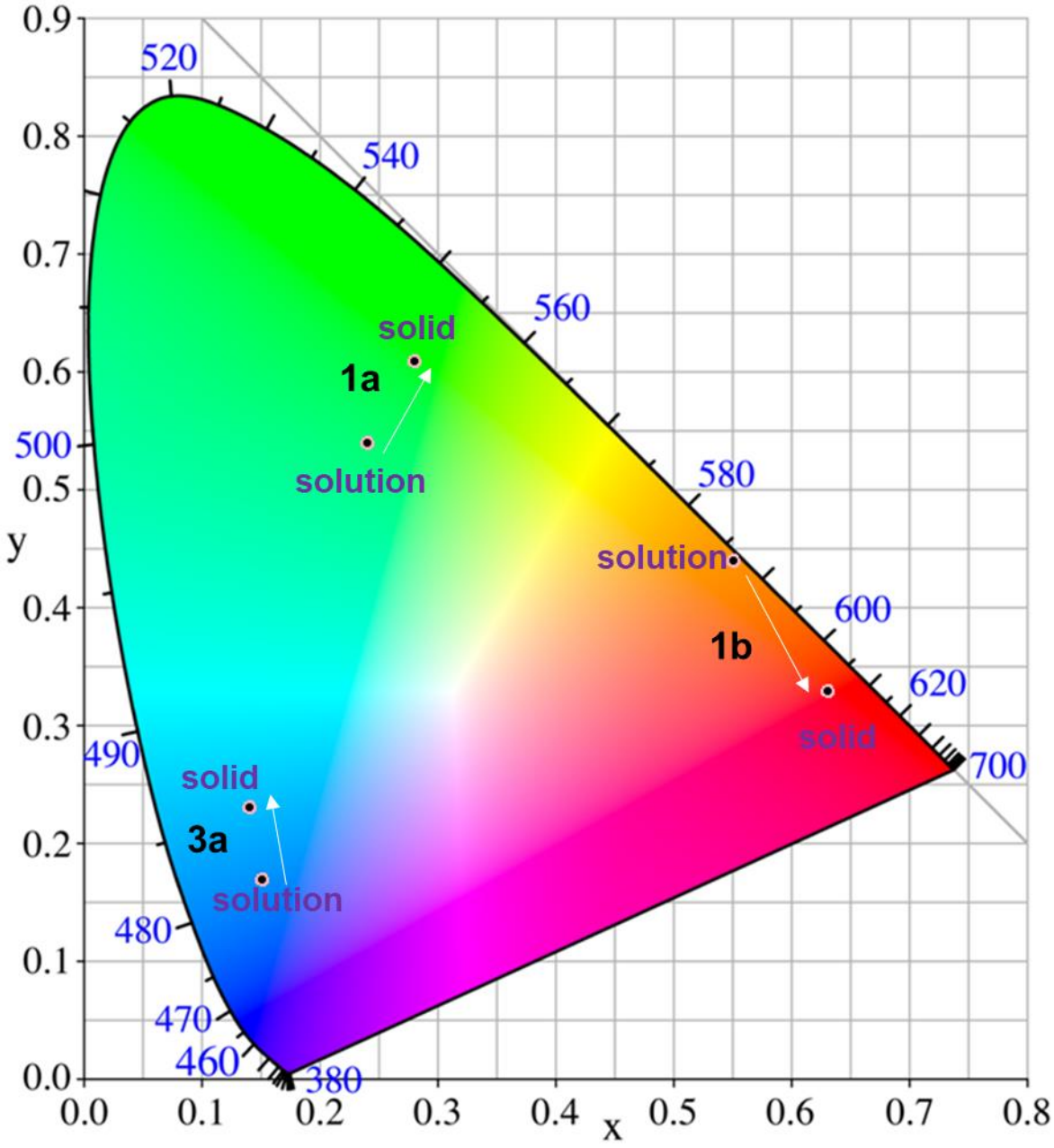

Supplementary Figure 46. CIE diagram of **1** and **3a** in toluene [coordinates for **1a**: (0.24, 0.54), **1b**: (0.55, 0.44), **3a**: (0.15, 0.17)] and solid states [coordinates for **1a**: (0.28, 0.61), **1b**: (0.63, 0.33), **3a**: (0.14, 0.23)].

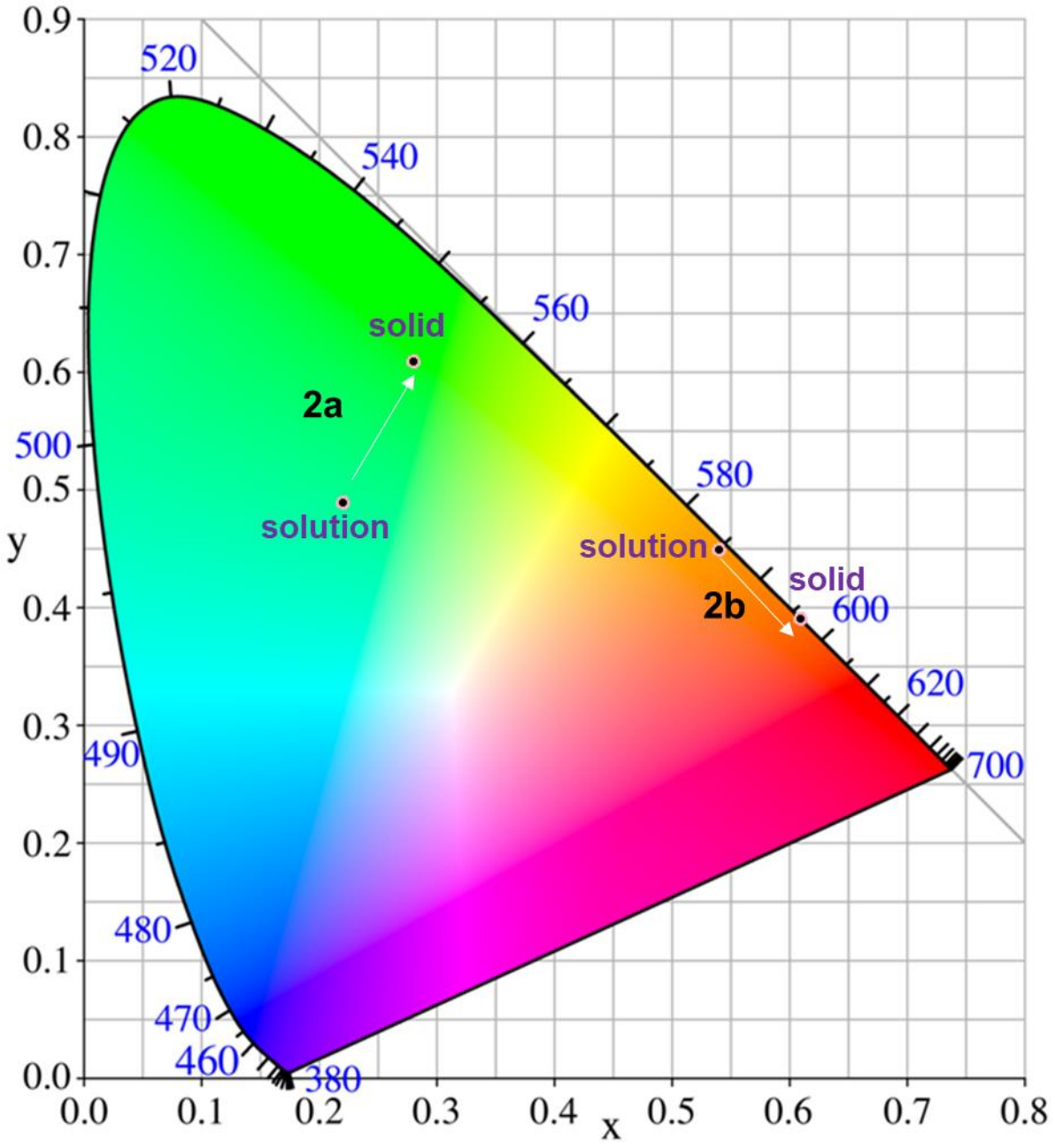

Supplementary Figure 47. CIE diagram of **2** in toluene [coordinates for **2a**: (0.22, 0.49), **2b**: (0.54, 0.45)] and solid states [coordinates for **2a**: (0.28, 0.61), **2b**: (0.61, 0.39)].

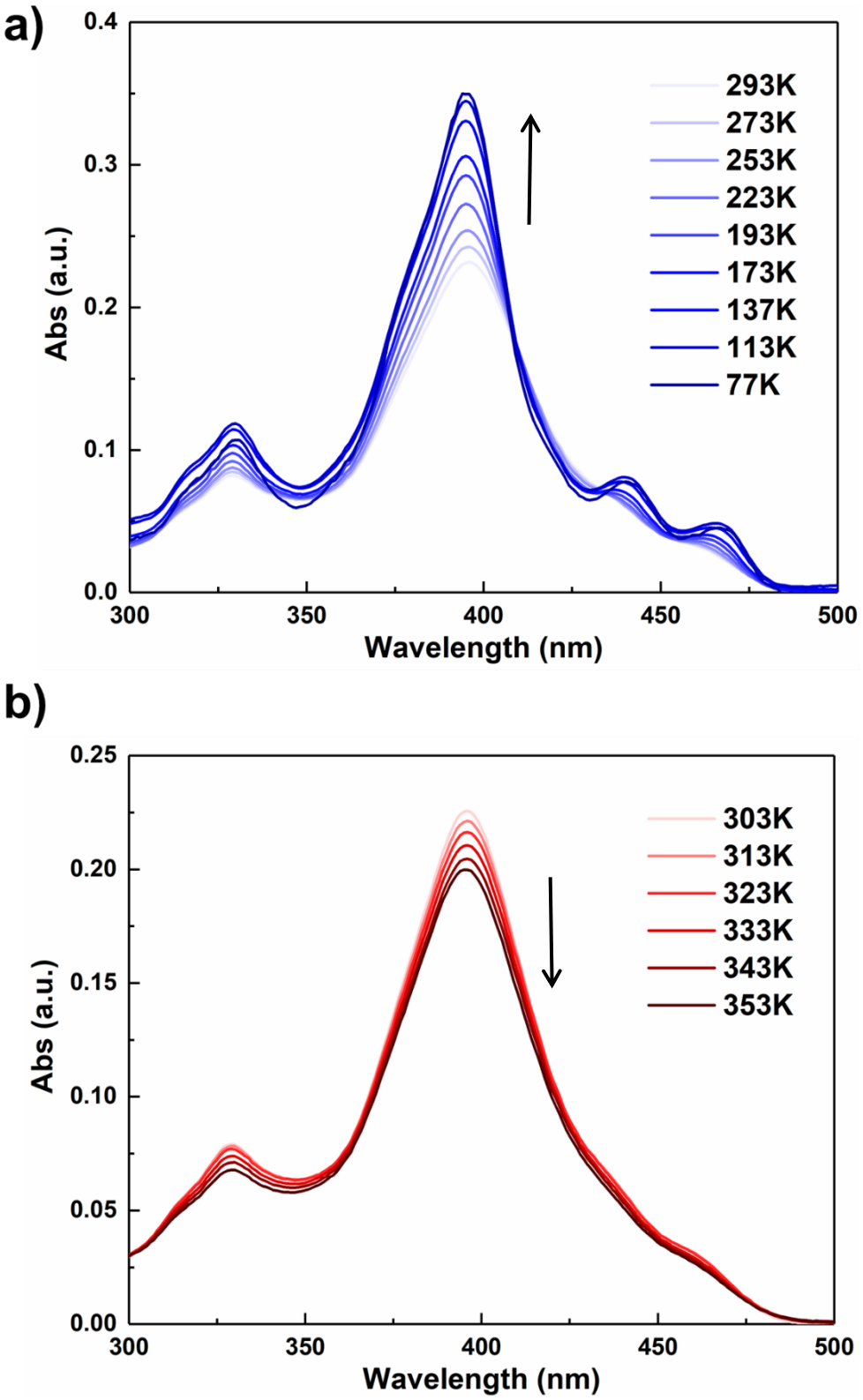

Supplementary Figure 48. Temperature-dependent UV-vis spectra of **1a** in 2-MeTHF (c = ~10^{-5} M) (a) cooling from 293 K to 77 K; (b) heating from 303 K to 353 K.

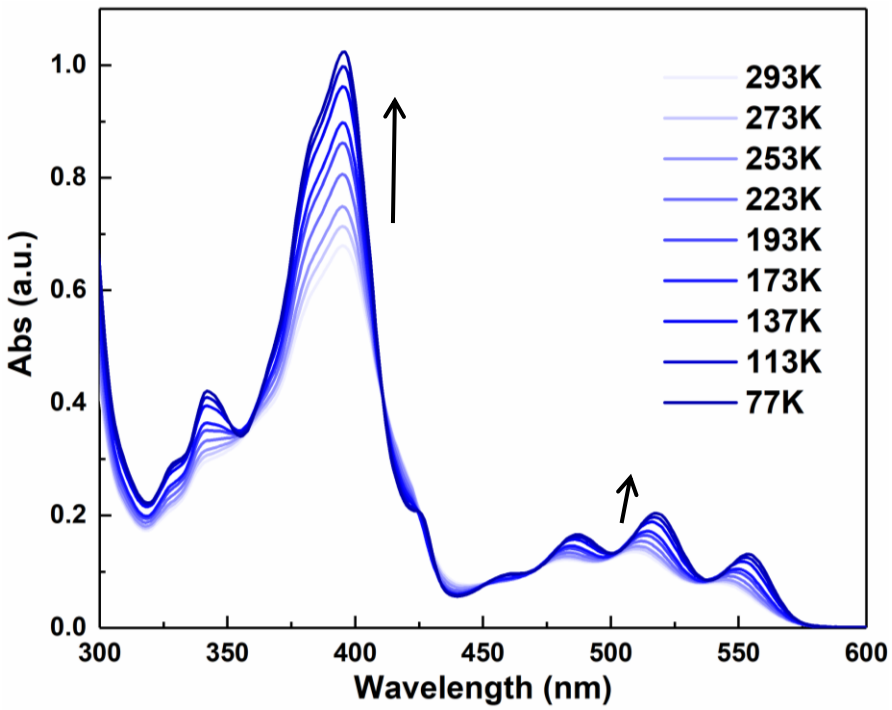

Supplementary Figure 49. Temperature-dependent UV-vis spectra of **1b** in 2-MeTHF (c = ~ 4 × 10^{-5} M) cooling from 293 K to 77 K. Heating above 313 K lead to a gradual decomposition in the ether solvent 2-MeTHF.

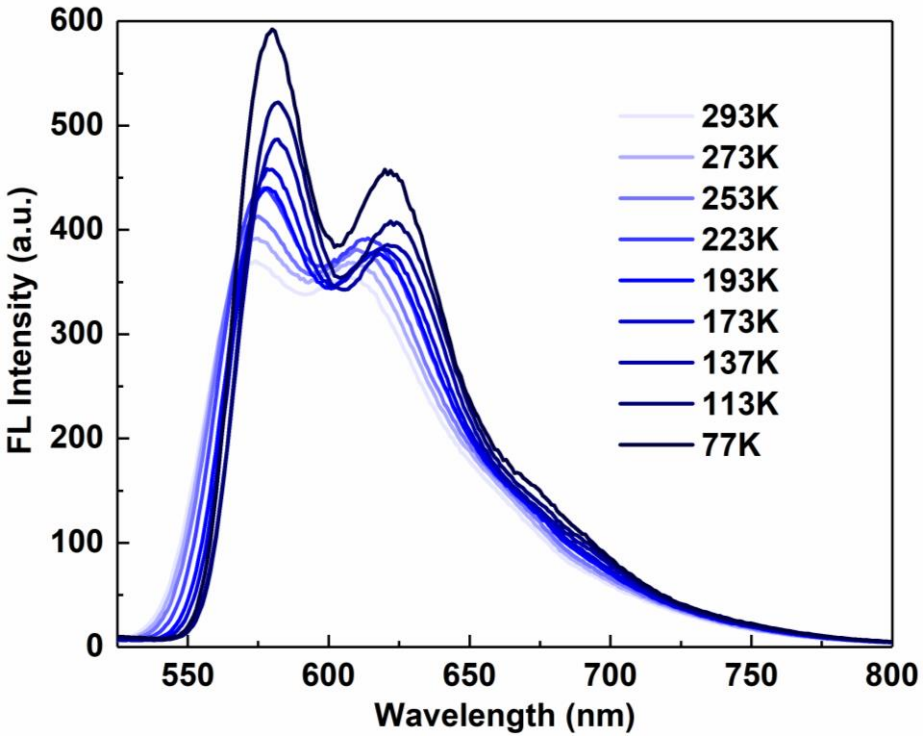

Supplementary Figure 50. Temperature-dependent fluorescence spectra of **1b** in 2-MeTHF (c = ~ 1 × 10^{-5} M) cooling from 293 K to 77 K.

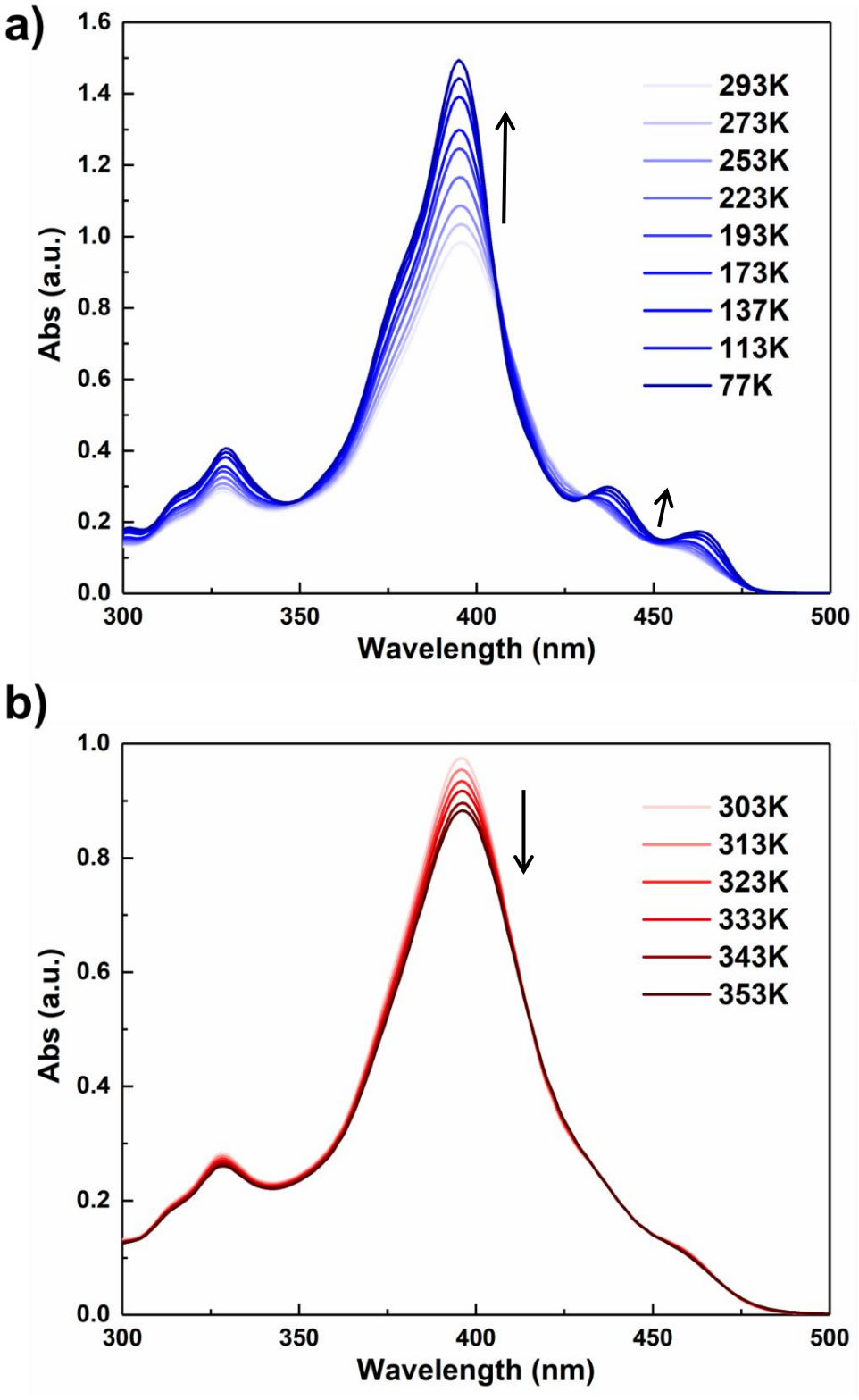

Supplementary Figure 51. Temperature-dependent UV-vis spectra of **2a** in 2-MeTHF (c = ~ 5 × 10^{-5} M) (a) cooling from 293 K to 77 K; (b)heating from 303 K to 353 K.

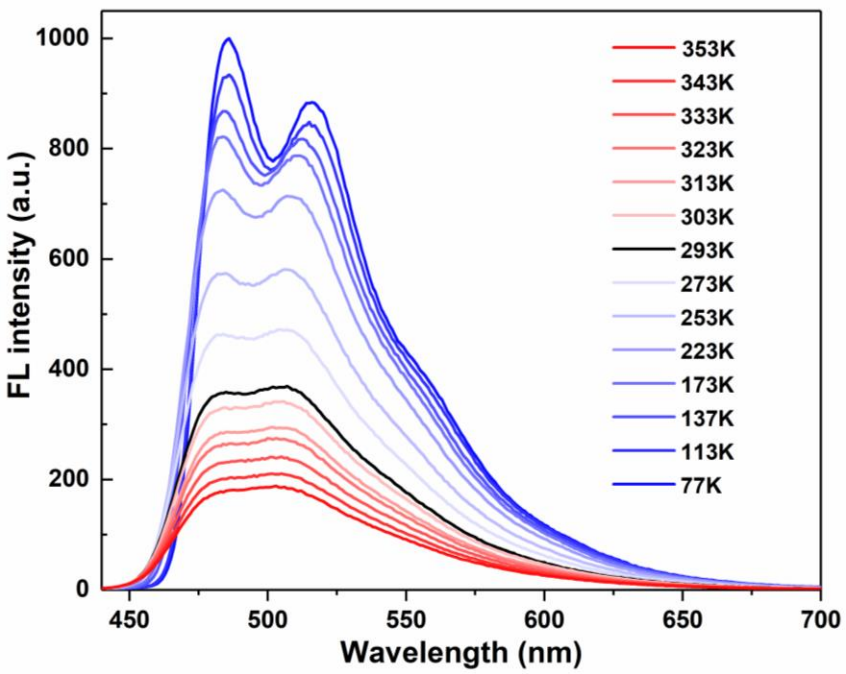

Supplementary Figure 52. Temperature-dependent fluorescence spectra of **2a** in 2-MeTHF (c = ~ 1 × 10^{-5} M) when cooling from 293 K to 77 K (blue line) and (red line) heating from 303 K to 353 K.

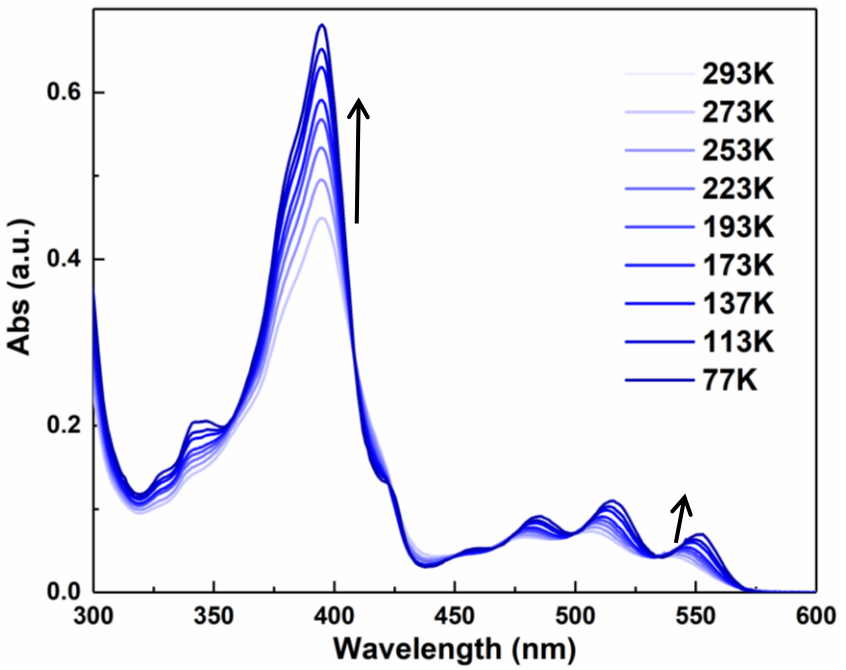

Supplementary Figure 53. Temperature-dependent UV-vis spectra of **2b** in 2-MeTHF (c = ~ 3 × 10^{-5} M) when cooling from 293 K to 77 K. Note: Heating above 313 K lead to a gradual decomposition in the ether solvent 2-MeTHF.

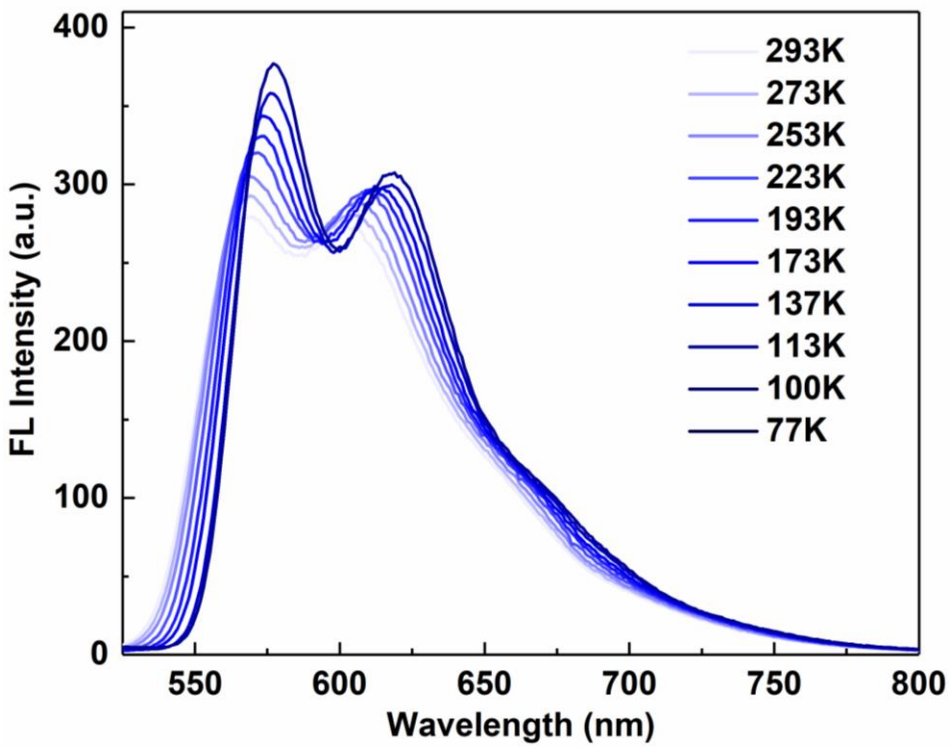

Supplementary Figure 54. Temperature-dependent fluorescence spectra of **2b** in 2-MeTHF (c = ~ 1 × 10^{-5} M) when cooling from 293 K to 77 K.

X-ray Crystallography Details

Single crystals of **1a, 1b, 2a, 2b, 3a, 3b,** or **7** were coated with Paratone oil and mounted on a MiTeGen MicroLoop. The X-ray intensity data were measured on a Bruker D8 Venture Kappa four-circle diffractometer system. An Incoatec IμS 3.0 micro-focus sealed X-ray tube (Mo Kα, λ = 0.71073 Å) and a HELIOS double bounce multilayer mirror monochromator were used for **1a, 1b**, **2b,** and **3a**. An Incoatec IμS 3.0 micro-focus sealed X-ray tube (Cu Kα, λ = 1.54178 Å) and a HELIOS EF double bounce multilayer mirror monochromator were used for **2a, 3b,** and **7**. The frames were integrated with the Bruker SAINT software package[4] using a narrow-frame algorithm. Data were corrected for absorption effects using the Multi-Scan method (SADABS).[5] Each structure was solved and refined using the Bruker SHELXTL Software Package[6] within APEX4[4] and OLEX2.[7] Non-hydrogen atoms were refined anisotropically. Hydrogen atoms were placed in geometrically calculated positions with U_{iso} = 1.2U_{equiv} of the parent atom (1.5U_{equiv} for methyl).

The relative occupancies of the disordered atoms in **1a**, **1b**, **2a**, **3b** and **7** were freely refined. In **3a**, the occupancy of the disordered atoms was set to 50% because of the symmetry of the atoms. Constraints and restraints were used on the anisotropic displacement parameters and/or bond lengths of most of the disordered atoms in these structures. In **1a**, **1b** and **7**, disordered solvent located in the crystal lattice was severely disordered and could not be adequately modeled with or without restraints. Thus, the structure factors were modified using the PLATON SQUEEZE[8] technique, in order to produce a "solvate-free" structure factor set. PLATON reported a total electron density of 639 e^- and total solvent accessible volume of 2344 $Å^3$ for **1a** (a mixture of CH_2Cl_2, hexanes, diethyl ether), 206 e^- and total solvent accessible volume of 571 $Å^3$ for **1b** (CH_2Cl_2), and 98 e^- and total solvent accessible volume of 428 $Å^3$ for **7** (a mixture of CH_2Cl_2, hexanes, benzene).

Supplementary Table 3: Crystallographic details for **1- 3** and **8**.

	1a	**1b**	**2a**	**2b**	**3a**	**3b**	**7**
CCDC number	2225725	2225726	2225727	2225728	2225729	2225730	2225731
Formula	$C_{59}H_{57}B2N5$	$C_{63}H_{59}B_2N_5$	$C_{65}H_{65}B_2N_5$	$C_{81}H_{91}B_2N_5O_3$	$C_{47}H_{49}B_2N_3$	$C_{51}H_{51}B_2N_3$	$C_{54}H_{46}B_5N_3O_8$
FW (g/mol)	854.90	907.77	937.84	1204.20	677.51	727.56	918.99
Temp (K)	100	100(2)	100(2)	100(2)	100(2)	100(2)	100(2)
λ (Å)	0.71073	0.71073	1.54178	0.71073	0.71073	1.54178	1.54178
Size (mm)	0.074 x 0.104 x 0.412	0.071 x 0.096 x 0.447	0.148 x 0.203 x 0.292	0.123 x 0.189 x 0.266	0.076 x 0.132 x 0.172	0.088 x 0.116 x 0.483	0.046 x 0.051 x 0.217
Crystal habit	yellow block	red block	yellow block	red block	yellow plate	orange rod	colorless needle
Crystal system	monoclinic	triclinic	orthorhombic	monoclinic	monoclinic	orthorhombic	triclinic
Space group	I 2/a	P -1	P $2_12_12_1$	P 2_1/n	P 2_1/m	P b c a	P -1
a (Å)	19.3990(13)	12.6109(13)	9.4399(3)	15.1099(7)	9.9515(7)	14.5365(7)	9.2128(4)
b(Å)	21.6314(13)	14.1407(17)	16.3313(5)	21.1608(7)	12.8852(8)	14.9501(8)	13.0444(5)
c (Å)	27.018(3)	18.621(2)	33.5958(11)	20.9358(9)	14.9575(11)	36.7509(19)	22.7905(8)
α (°)	90	110.223(3)	90	90	90	90	106.151(2)
β (°)	90.114(2)	99.411(3)	90	98.421(2)	101.502(2)	90	90.725(3)
γ (°)	90	105.537(4)	90	90	90	90	96.145(3)
Volume ($Å^3$)	11337.5(15)	2879.1(6)	5179.3(3)	6621.8(5)	1879.4(2)	7986.8(7)	2613.06(18)
Z	8	2	4	4	2	8	2
Density (g/cm^3)	1.002	1.047	1.203	1.208	1.197	1.210	1.168
μ (mm^{-1})	0.058	0.061	0.528	0.072	0.068	0.523	0.616
F(000)	3636	964	2000	2584	724	3104	960

θ range (°)	2.06 to 25.71	1.93 to 25.73	4.79 to 74.60	2.04 to 28.27	2.09 to 26.39	3.88 to 68.30	3.55 to 68.38
Index ranges	-23 ≤ h ≤ 23 -23 ≤ k ≤ 26 -32 ≤ l ≤ 32	-15 ≤ h ≤ 15 -17 ≤ k ≤ 17 -22 ≤ l ≤ 22	-11 ≤ h ≤ 11 -20 ≤ k ≤ 20 -42 ≤ l ≤ 39	-20 ≤ h ≤ 20 -25 ≤ k ≤ 28 -27 ≤ l ≤ 27	-12 ≤ h ≤ 12 -13 ≤ k ≤ 16 -18 ≤ l ≤ 18	-17 ≤ h ≤ 17 -17 ≤ k ≤ 18 -44 ≤ l ≤ 44	-10 ≤ h ≤ 11 -15 ≤ k ≤ 15 -27 ≤ l ≤ 27
Reflns collected	60971	77830	52515	105352	29294	61268	41611
Independent reflns	10799 [R_{int} = 0.0616]	10957 [R_{int} = 0.0933]	10393 [R_{int} = 0.0269]	16409 [R_{int} = 0.0574]	4030 [R_{int} = 0.1070]	7298 [R_{int} = 0.0995]	9526 [R_{int} = 0.0564]
Data / restraints /parameters	10799 / 1411 / 873	10957 / 426 / 730	10393 / 2 / 652	16409 / 0 / 822	4030 / 2 / 276	7298 / 0 / 542	9526 / 126 / 674
GOF on F^2	1.048	1.051	1.039	1.051	1.024	1.102	1.064
R_1 (I>2σ(I))	0.0621	0.0834	0.0276	0.0467	0.0571	0.0709	0.0549
wR_2 (all data)	0.1679	0.2230	0.0688	0.1230	0.1223	0.1821	0.1684

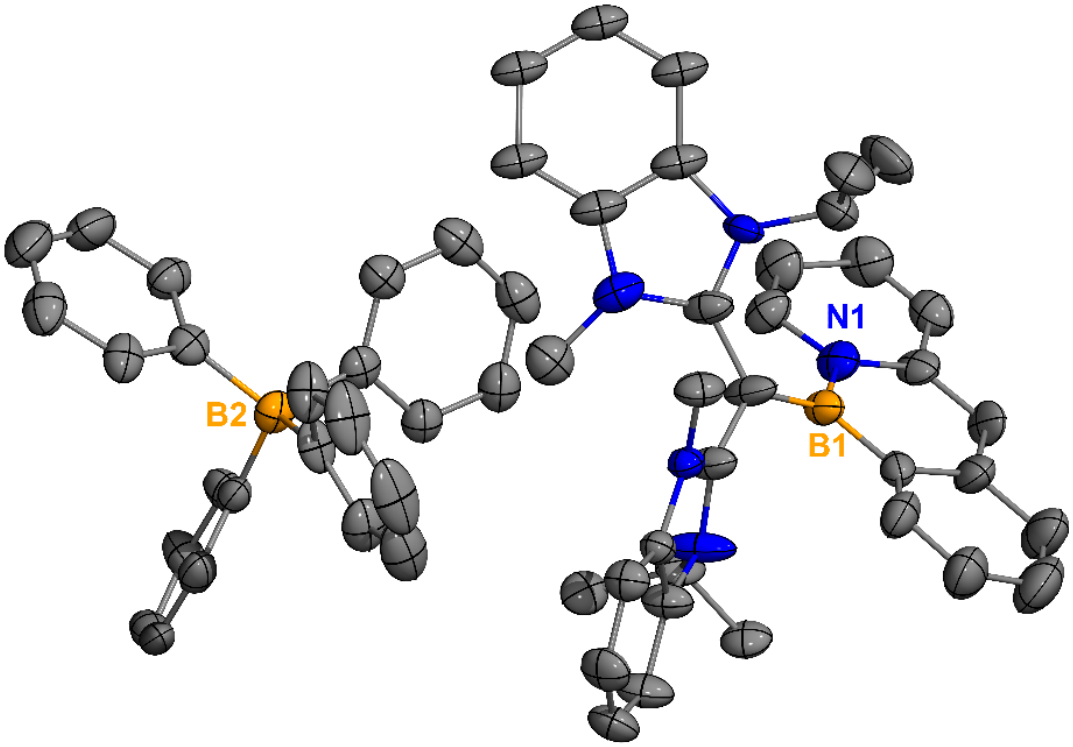

Supplementary Figure 55. Molecular structure of **1a**. Thermal ellipsoids are shown at 50% probability and H atoms were omitted for clarity. Note: positional disorders were found among the crystal lattices, especially for the BN backbone, thus the bond lengths are not summarized here.

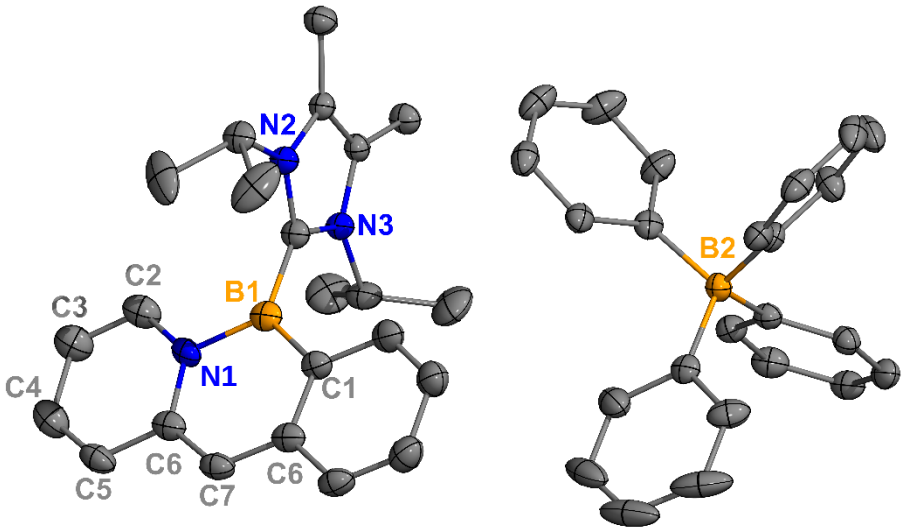

Supplementary Figure 56. Molecular structure of **3a**. Thermal ellipsoids are shown at 50% probability and H atoms were omitted for clarity. For the disordered atoms, only the component with the highest occupancy is shown. Selected bond lengths (in Å): B1–C1 1.56(7), C1–C2 1.37(3), C2–C3 1.352(3), C3–C4 1.419(3), C4–C5 1.359(3), C5–C6 1.422(3), C6–C7 1.391(3), C2–C3 1.352(3), C6–N1 1.46(3).

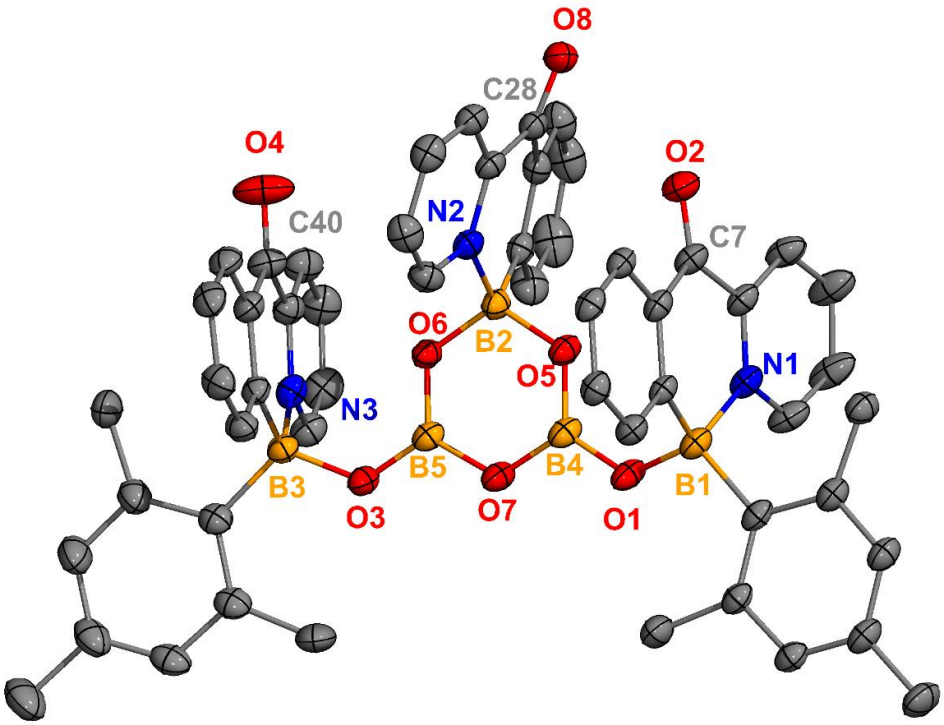

Supplementary Figure 57. Molecular structure of **7**. Thermal ellipsoids are shown at 30% probability and H atoms were omitted for clarity. Selected bond lengths (in Å): B1–O1 1.451(3), B2–O5 1.446(2), B2–O6 1.444(3), B3–O3 1.451(3), B4–O1 1.347(3), B4–O5 1.361(3), B4–O7 1.388(3), B5–O7 1.392(3), B5–O6 1.363(3), B5–O3 1.338(3), C7–O2 1.220(2), C28–O8 1.228(3), C40–O4 1.220(3), B1–N1 1.656(4), B2–N2 1.639(3), B3–N3 1.639(3).

Theoretical Calculations

General

All geometries were optimized with ORCA 5.0.2.,[9,10] using the B3LYP[11,12] (B3LYP/G) functional in conjunction with a triple-ζ quality basis set (def2-TZVP).[13,14] The dispersion corrections were introduced using the Grimme D3-parametrized correction[15] and the Becke Johnson damping to the DFT energy.[16] The RIJCOSX approximation[17] was used to reduce the computational cost of calculations. The initial structures were generated from the above X-ray crystallography data while the counter anions (BPh_4^-) were not included. The bond lengths errors for all optimized structures are within 0.02 Å when compared to the crystal structure. In addition, characterization of stationary points as minima were verified by analytical vibrational mode analysis.

Natural bond order (NBO) and natural population analysis (NPA) were performed using NBO 6.0 program[18] at the B3LYP-D3(BJ)/def2-TZVP level of theory. The out-of-plane nucleus-independent chemical shift [NICS(1)] and [$NICS(1)_{zz}$] were calculated at the GIAO-B3LYP/pcSseg-2 level of theory[19] at the geometrical center of the ring. Due to the nonplanarity of the BN-acene backbone, the NICS(1) and $NICS(1)_{zz}$ values are the average of NICS(1)/ NICS(−1) and $NICS(1)_{zz}$ /$NICS(-1)_{zz}$, respectively. In that analysis the aromatic rings have negative values and nonaromatic rings have positive values. The anisotropy of the current (induced) density (ACID)[20] and localized orbital locator for π electrons (LOL-π)[21] calculations were carried out at B3LYP-D3(BJ)/def2-TZVP level of theory. Except for the NBO analysis, all the calculations were performed with Gaussian 16,[22] the wavefunction analysis were conducted using Multiwfn program.[23] Coordination of the azaboraacenes and ligands were investigated using the extended transition state method for energy decomposition analysis combined with the natural orbitals for chemical valence theory (ETS-NOCV)[24,25] as implemented in the ORCA. For the intrinsic bond orbitals (IBOs) calculations,[26] wave functions were obtained in the ORCA and structural depictions were made using the IboView.[27] The spin-orbit coupling (SOC) matrix elements between S_m/T_n states were calculated with PySOC[28] interfaced to the Gaussian 16 program. The detailed electronic structures of **1a** and **1b** were investigated using the fractional occupation weighted density (FOD) analyses[29,30] were performed at the TPSS/def2-TZVP level of theory. The T1 diagnostics value[31] were extracted from the domain-based local pair natural orbital (DLPNO)[32] coupled cluster singles and doubles with perturbative triple excitations [CCSD(T)][33] calculations at the cc-pVTZ[34] levels of theory. Both of wavefunction theory calculations are performed by using the ORCA package.

Calculated Frontier Orbital Energies

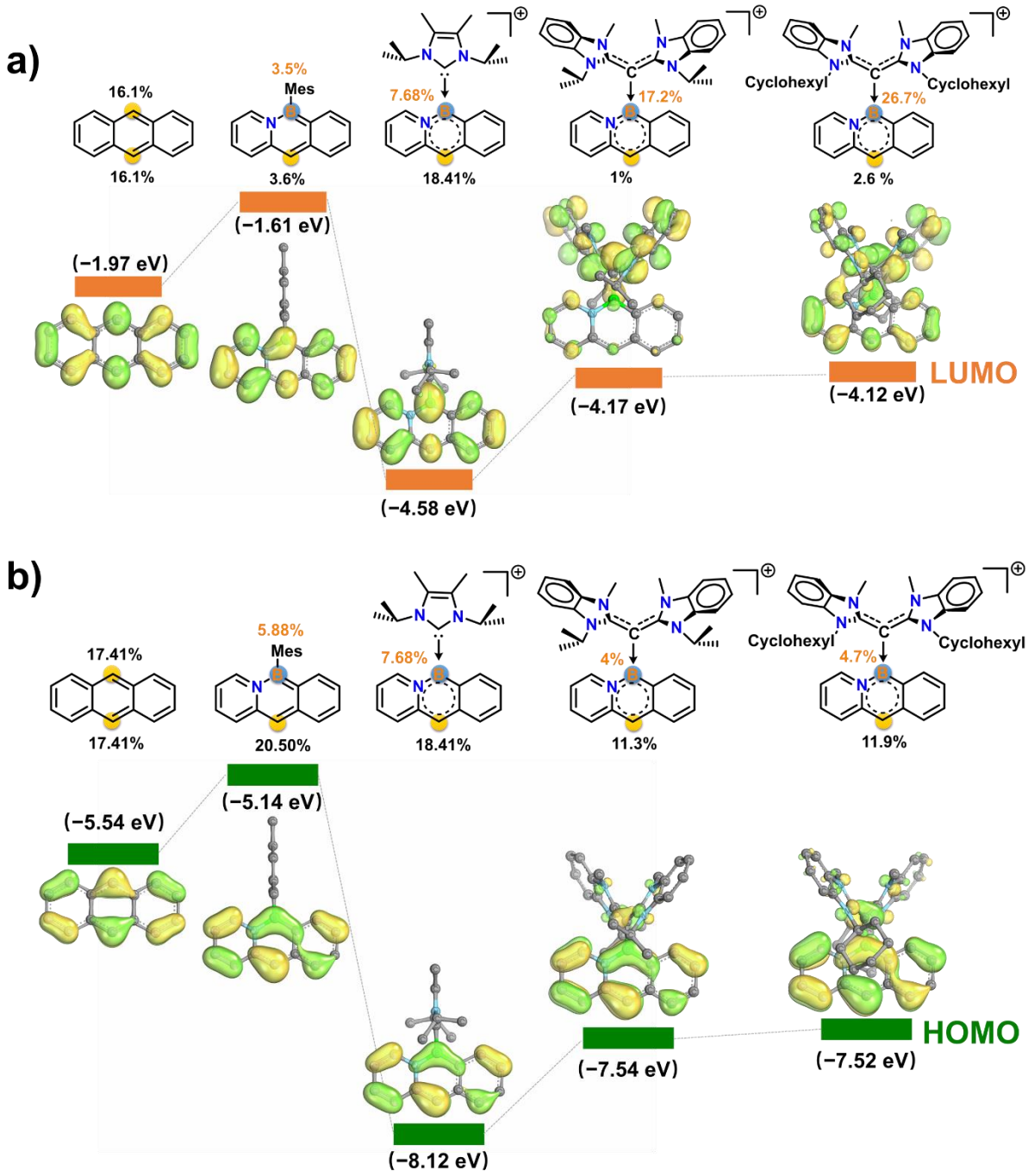

Supplementary Figure 58. Atomic orbital coefficients of "C" and "B" in (a) LUMOs (b) HOMOs and their orbital energies (in eV, calculated at the B3LYP-D3(BJ)/def2-TZVP level of theory in gas phase) for anthracene, **6a**, **3a** and **1a** (from left to right). The coefficients of carbon and boron atoms are marked with orange and cyan circles, respectively. The higher stability of **1a** *vs* **6a** towards O_2/light may be due to the significantly decreased energy levels of HOMOs and their atomic coefficients and on the reactive sites of acenes. The B atoms in **1a**/**2a** have the most abundant atomic coefficients, which reflect their borenium characters.

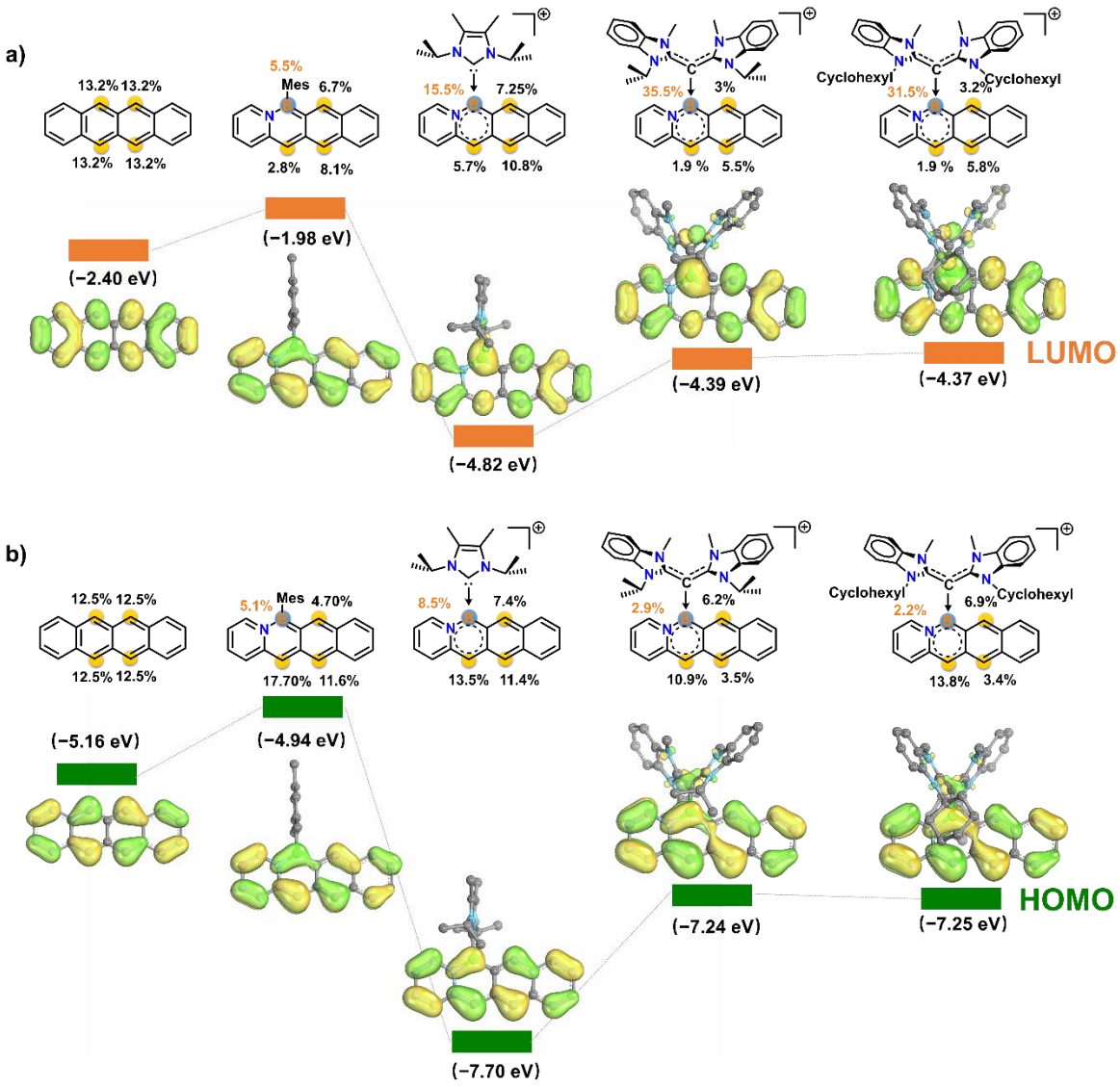

Supplementary Figure 59. Atomic orbital coefficients of "C" and "B" in (a) LUMOs (b) HOMOs and their orbital energies (in eV, calculated at the B3LYP-D3(BJ)/def2-TZVP level of theory in gas phase) for tetracene, **6b**, **3b**, **1b** and **2b** (from left to right). The coefficients of carbon and boron atoms are marked with orange and cyan circles, respectively. The higher stability of **1b/2b** *vs* tetracene towards O_2/light may be due to the significantly decreased energy levels of FMOs and their atomic coefficients and on the reactive sites of acenes. The B atoms in **1b/2b** have the most abundant atomic coefficients, which reflect their borenium characters.

Bond Order Analysis

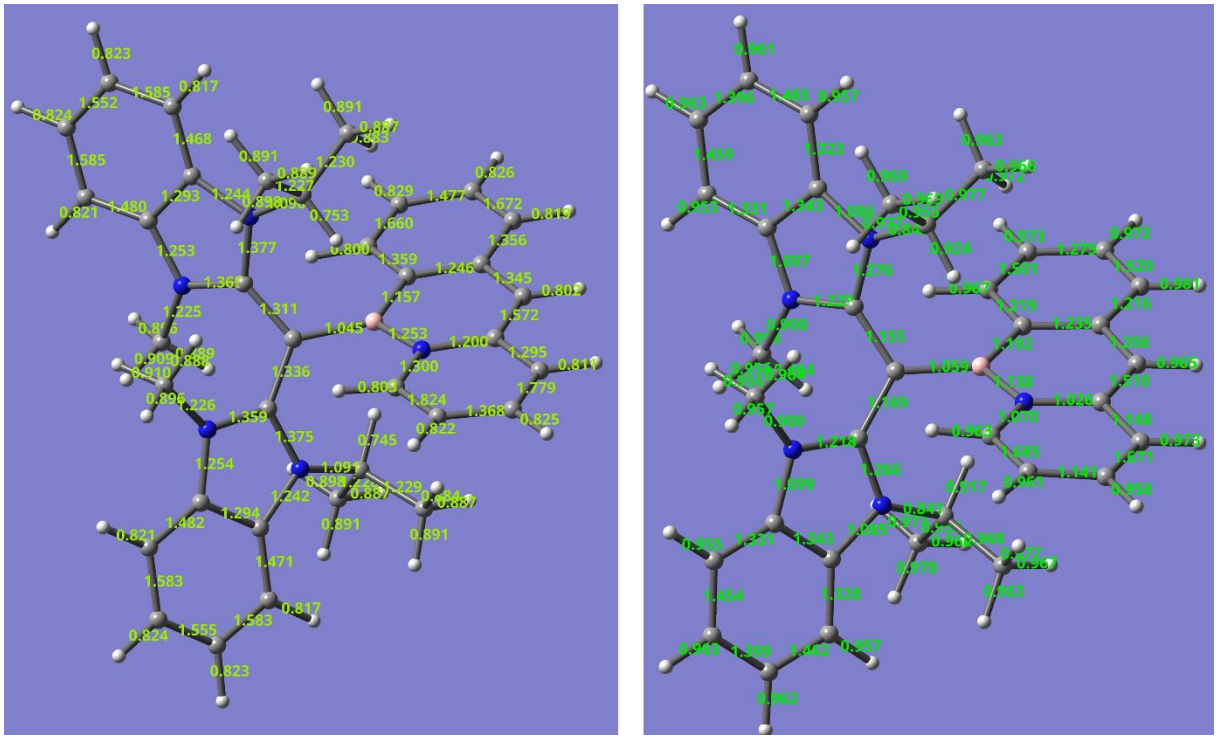

Supplementary Figure 60. Wiberg bond indices (WBI) (left, shown in yellow-green color) and Mayer bond indices (MBI) (right, shown in green color) for **1a**.

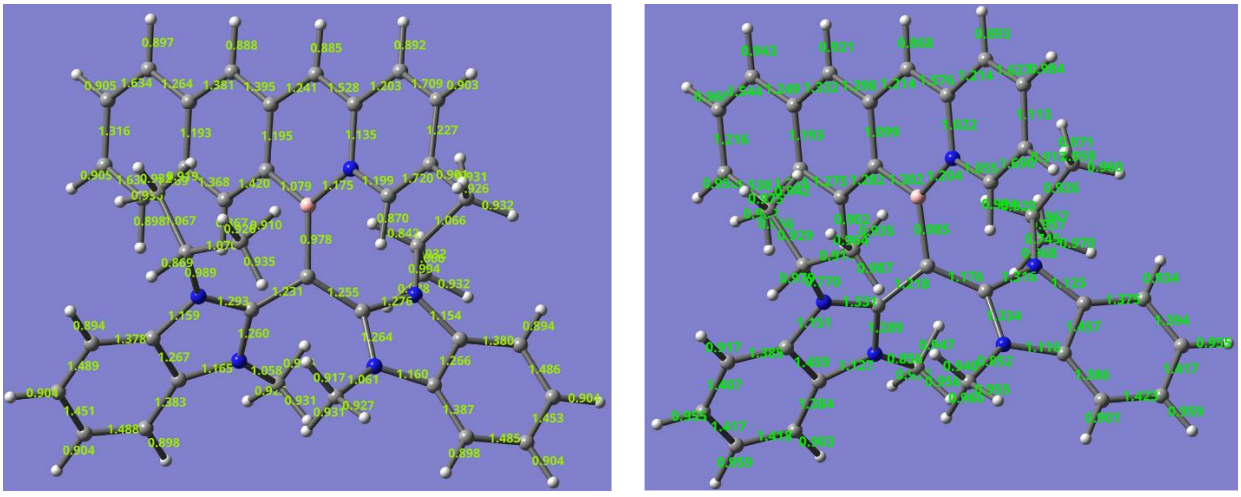

Supplementary Figure 61. Wiberg bond indices (WBI) (left, shown in yellow-green color) and Mayer bond indices (MBI) (right, shown in green color) for **1b**.

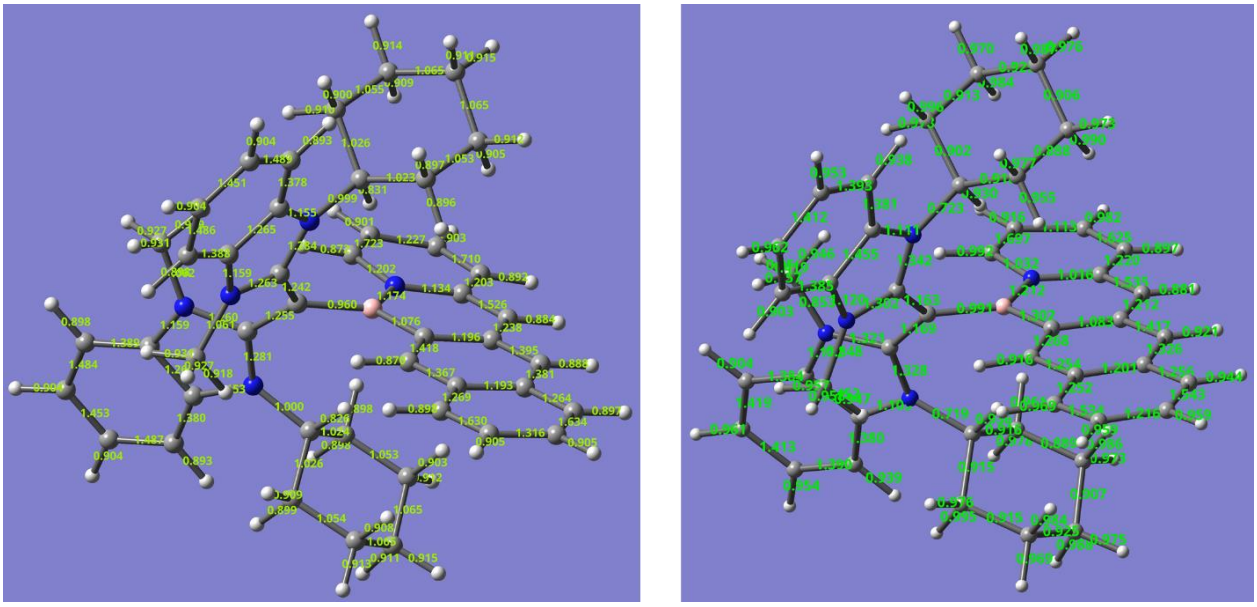

Supplementary Figure 62. Wiberg bond indices (WBI) (left, shown in yellow-green color) and Mayer bond indices (MBI) (right, shown in green color) for **2a**.

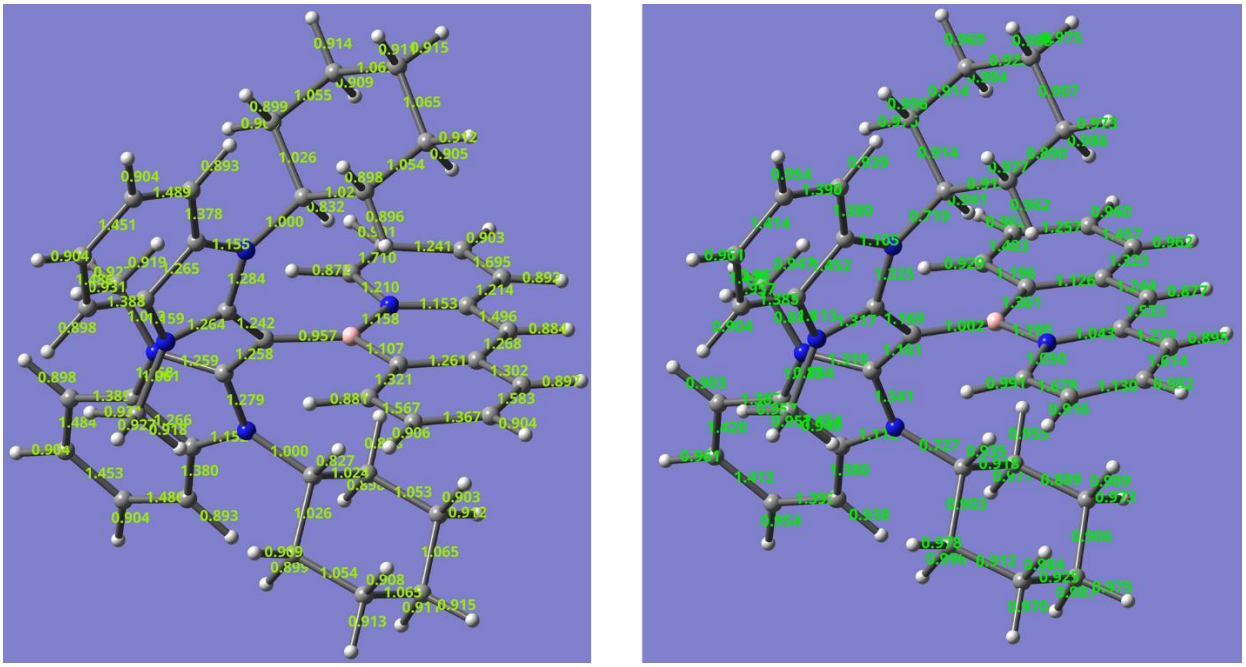

Supplementary Figure 63. Wiberg bond indices (WBI) (left, shown in yellow-green color) and Mayer bond indices (MBI) (right, shown in green color) for **2b**.

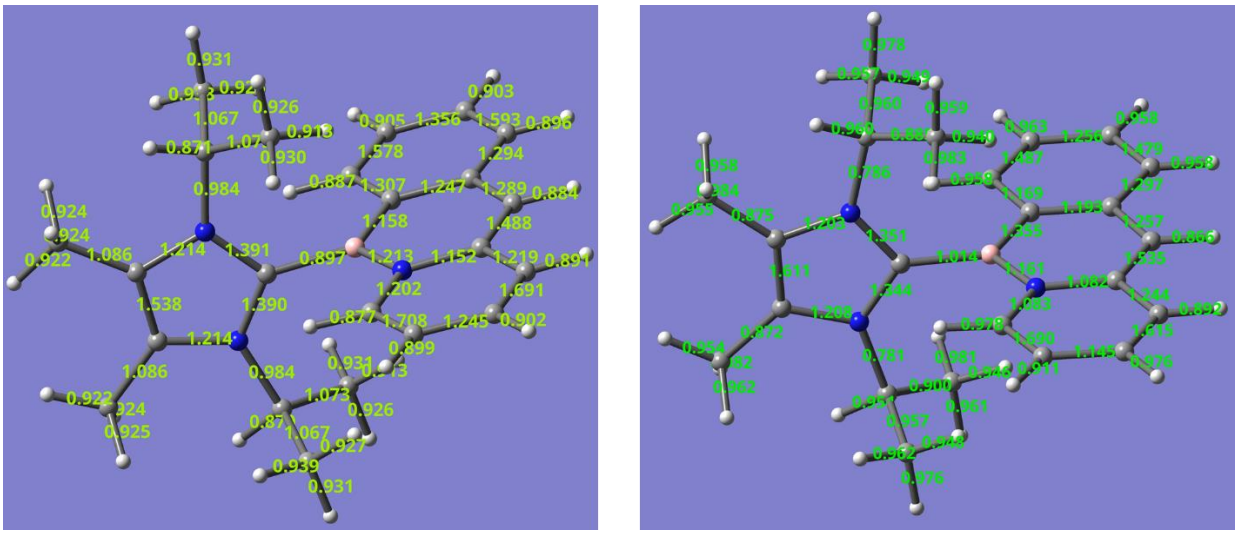

Supplementary Figure 64. Wiberg bond indices (WBI) (left, shown in yellow-green color) and Mayer bond indices (MBI) (right, shown in green color) for **3a**.

QTAIM Analysis and Non-Covalent Interactions (NCI) Plot

The QTAIM[35] analyses were conducted based on the optimized geometries. A bonding critical point (BCP) in accordance with the AIM theory locates between two atoms containing the considered bond. The most important parameters for description of the interaction are the electron density ρ(r) and the Laplacian of the electron density [$\nabla^2\rho(r)$]. In general, large values of the electron density ρ(r) indicate a strong bonding interaction (for the same type of chemical bond). A negative $\nabla^2\rho(r)$ shows the excess potential energy at the BCP which means that the electronic charge is contracted between two nuclei (covalent interaction), while a positive $\nabla^2\rho(r)$ reveals that the kinetic energy contribution is greater than the potential energy (closed-shell interaction). QTAIM topological parameter $G(r)$ is the Lagrangian kinetic energy and $V(r)$ is the local potential electron energy density. The sign of electronic energy $H(r)$ on the Hamiltonian at BCP determines whether the accumulation of charge at a given point is stabilizing [$H(r) < 0$] or destabilizing [$H(r) > 0$]. The nature of bond can be evaluated by means of the $|V(r)|/G(r)$.[36] If $|V(r)|/G(r) > 2$, then the bond has covalent character while for the $1 < |V(r)|/G(r) < 2$, the bond has partially covalent character. If $|V(r)|/G(r) < 1$, suggesting the bonding is closed-shell interaction (Supplementary Table 4).

To visualize the position and different types of non-covalent interactions in 3D space, the gradient isosurfaces (cutoff = 0.5 a.u.) of the reduced density gradient (RDG)[37] at low densities, colored on a blue–green–red scale according to values of sign $(\lambda_2)\rho(r)$ (ranging from −0.025 to 0.03 a.u.) were obtained. The blue isosurface represents strong attractive interactions, green indicates van der Waals interactions and red indicates repulsive/steric interactions.

Supplementary Table 4 Values of the density of all electrons ρ(r), Laplacian of electron density $\nabla^2\rho(r)$, local potential electron energy density $V(r)$, energy density $H(r)$, Lagrangian kinetic energy $G(r)$ (in a.u.) at the bond critical points (BCPs) for C1−B1 bonds among the structure of **1**, **2** and **3a**, calculated at B3LYP-D3(BJ)/def2-TZVP level of theory

	BCPs for C1−B1 bond					
	ρ(r)	**$\nabla^2\rho(r)$**	$V(r)$	$H(r)$	$G(r)$	$\|V(r)\|/G(r)$
1a	0.17925	−0.15834	−0.34642	−0.19301	0.15342	2.258
1b	0.17669	−0.11600	−0.33324	−0.18112	0.15212	2.191
2a	0.17481	−0.12936	−0.32564	−0.17900	0.14665	2.220
2b	0.17550	−0.13080	−0.32170	−0.32732	0.14731	2.184
3a	0.16690	−0.01448	−0.32170	−0.16266	0.15904	2.023

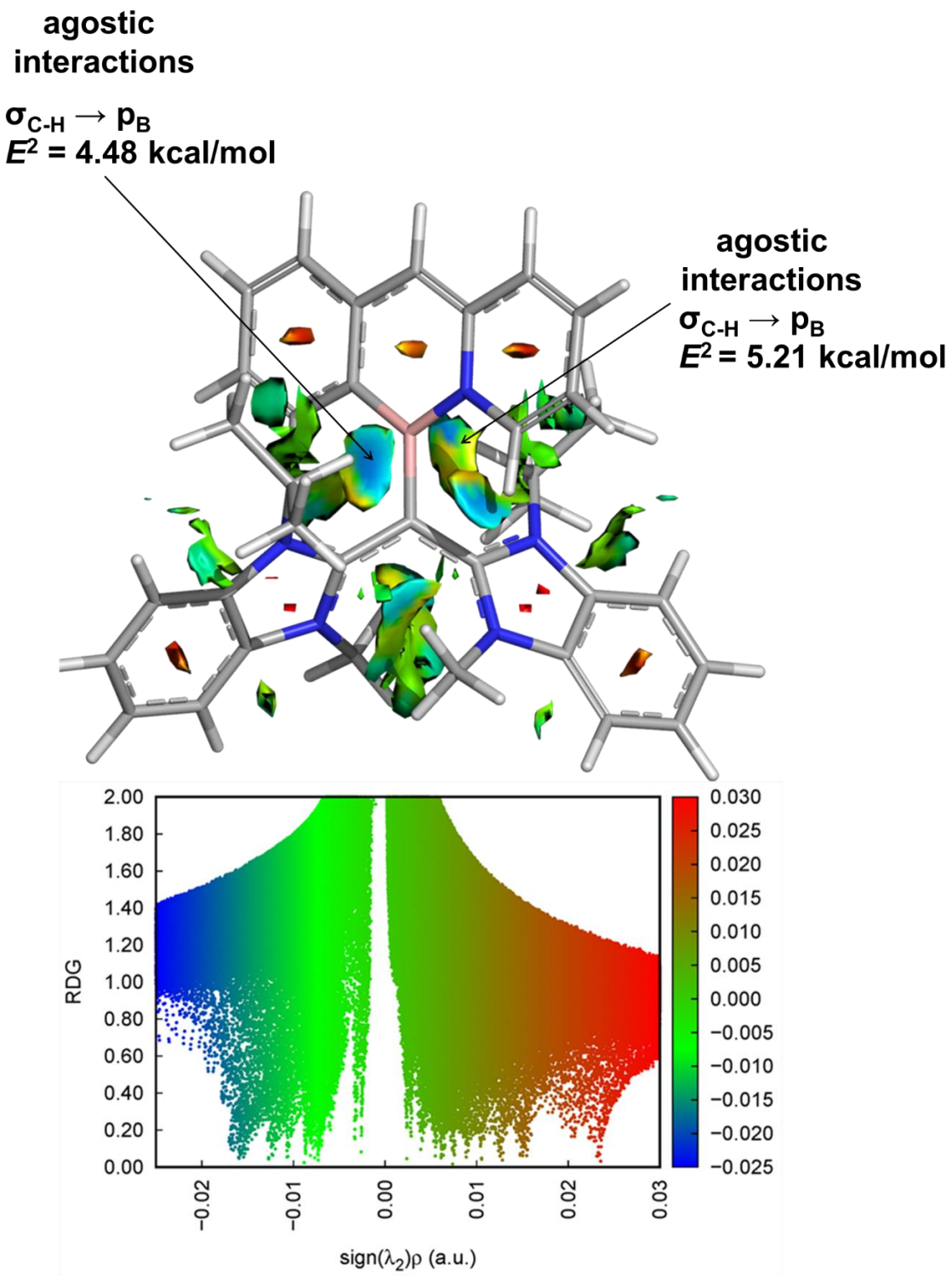

Supplementary Figure 65. Non-covalent interactions (NCI) plots (top) and RDG scatter plots (bottom) of **1a (**calculated from the B3LYP-D3(BJ)/def2-TZVP level of theory). The isosurfaces are colored according to the values of sign (λ_2)ρ(r) (ranging from −0.025 to 0.03 a.u., blue to green). The stronger agostic interactions are marked

with arrows. The related donor-acceptor NBO interactions and second-order perturbation energies (E^2) are also given.

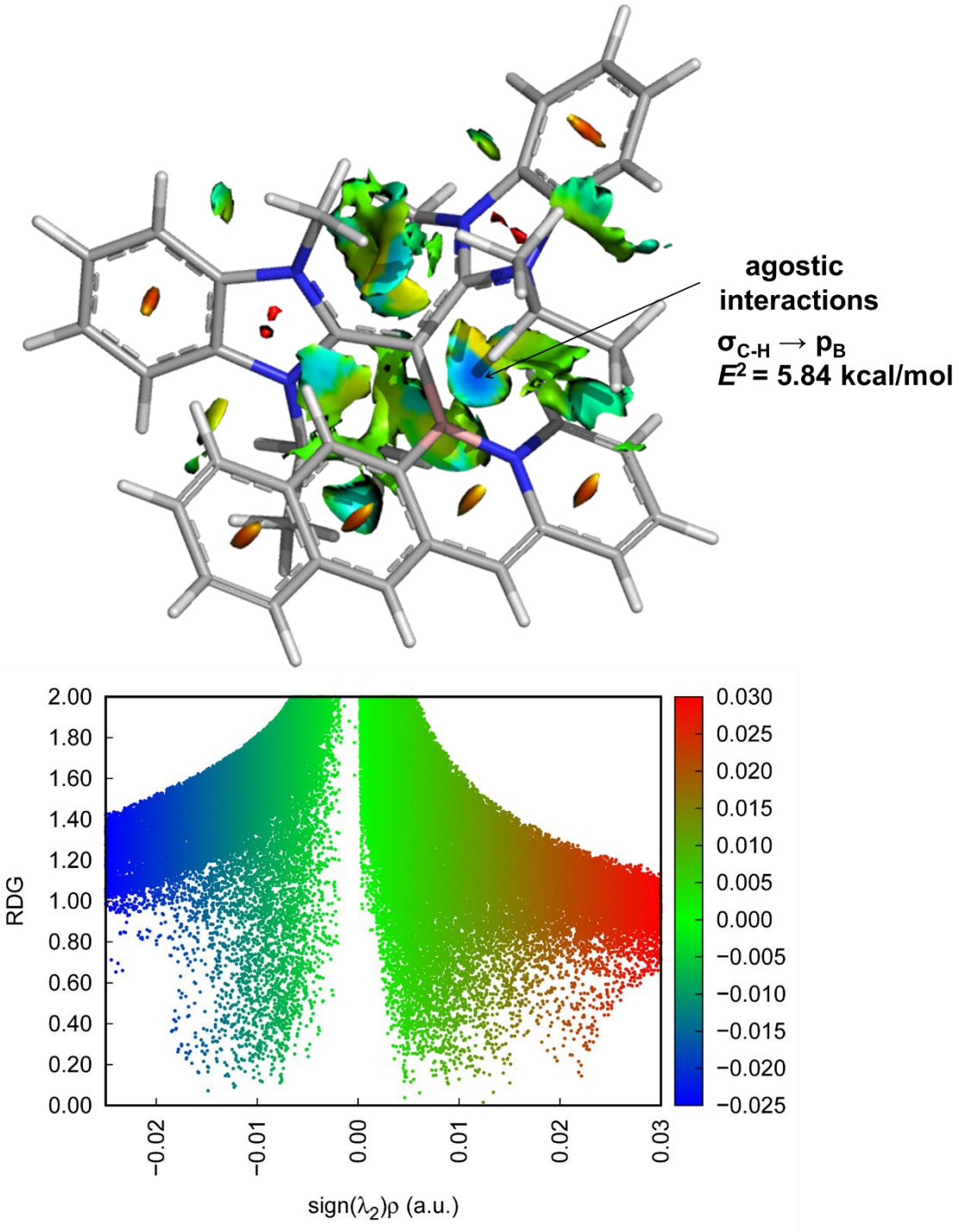

Supplementary Figure 66. Non-covalent interactions (NCI) plots (top) and RDG scatter plots (bottom) of **1b (**calculated from the B3LYP-D3(BJ)/def2-TZVP level of theory). The isosurfaces are colored according to the values of sign (λ_2)ρ(r) (ranging from −0.025 to 0.03 a.u., blue to green). The agostic interactions are marked with

arrows. The stronger interactions are marked with arrows. The related donor-acceptor NBO interactions and second-order perturbation energies (E^2) are also given.

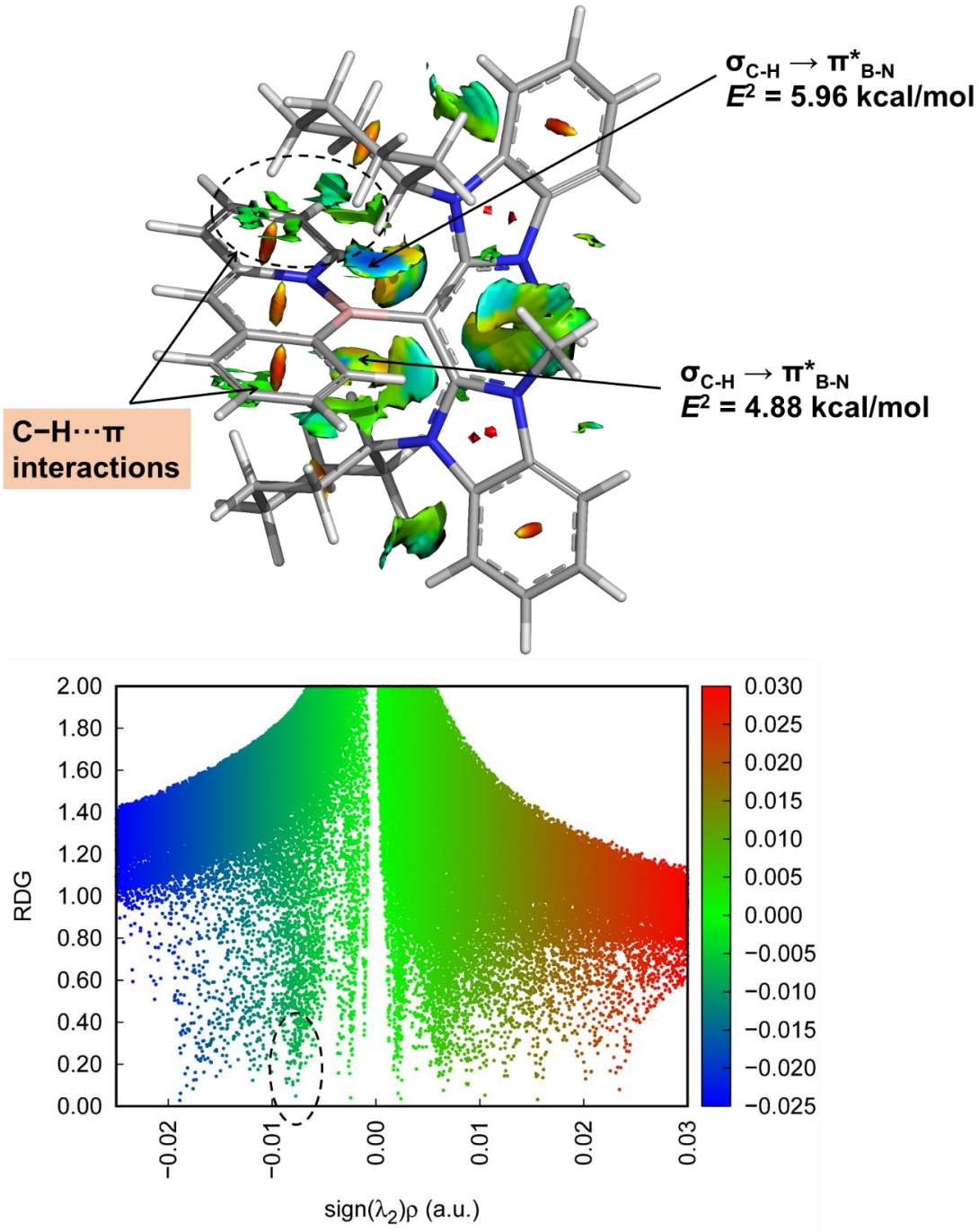

Supplementary Figure 67. Non-covalent interactions (NCI) plots (top) and RDG scatter plots (bottom) of **2a (**calculated from the B3LYP-D3(BJ)/def2-TZVP level of theory). The isosurfaces are colored according to the values of sign (λ_2)ρ(r) (ranging from −0.025 to 0.03 a.u., blue to green). The agostic interactions and the C-H···π interactions among the cyclohexyl sidearms and the heterocyclic molecular plane are marked with arrows. The

stronger interactions are marked with arrows. The related donor-acceptor NBO interactions and second-order perturbation energies (E^2) were also given.

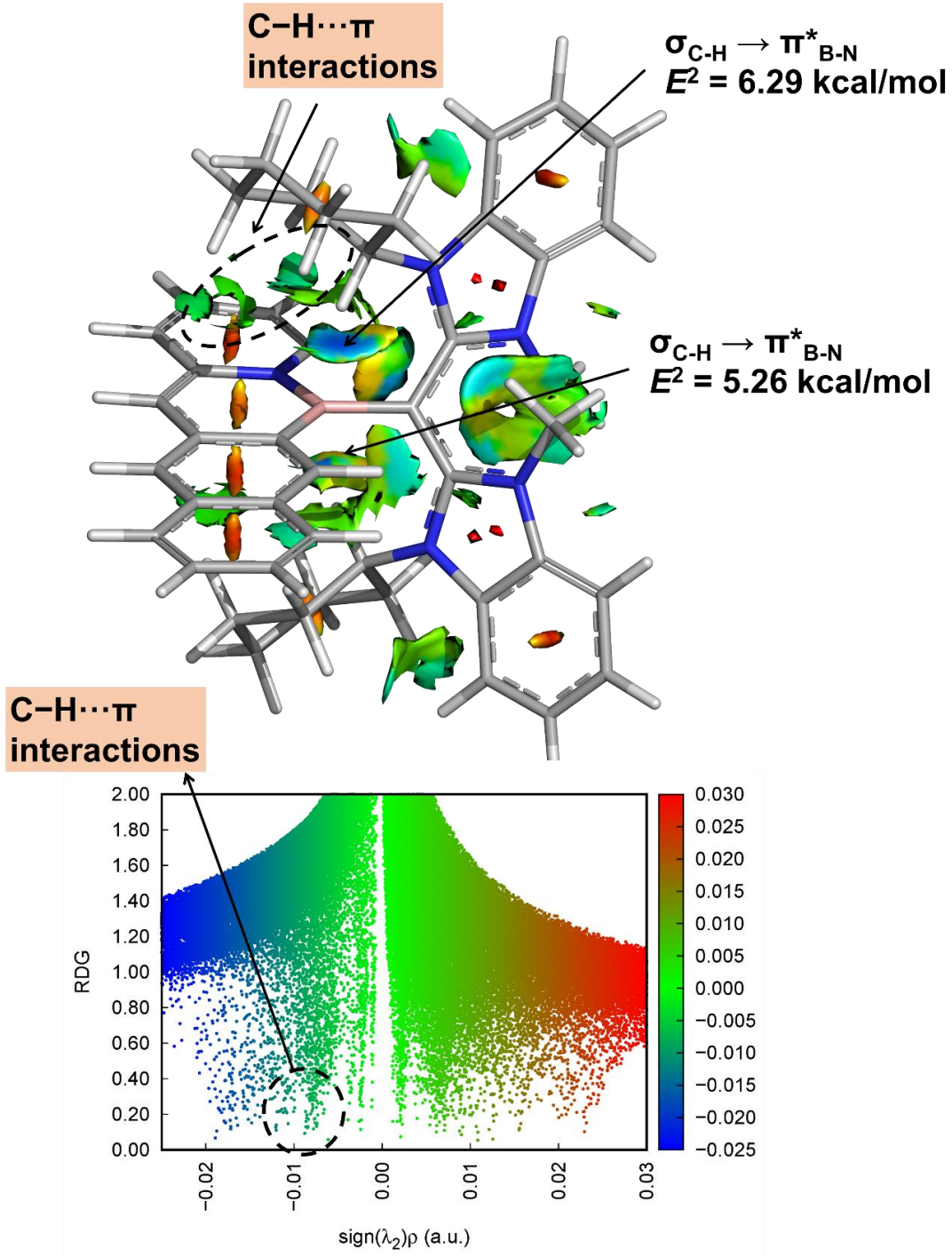

Supplementary Figure 68. Non-covalent interactions (NCI) plots (top) and RDG scatter plots (bottom) of **2b (**calculated from the B3LYP-D3(BJ)/def2-TZVP level of theory). The isosurfaces are colored according to the values of sign (λ_2)ρ(r) (ranging from −0.025 to 0.03 a.u., blue to green). The agostic interactions and the C-H···π interactions among the cyclohexyl sidearms and the heterocyclic molecular plane are marked with arrows. The

stronger interactions are marked with arrows. The related donor-acceptor NBO interactions and second-order perturbation energies (E^2) are also given.

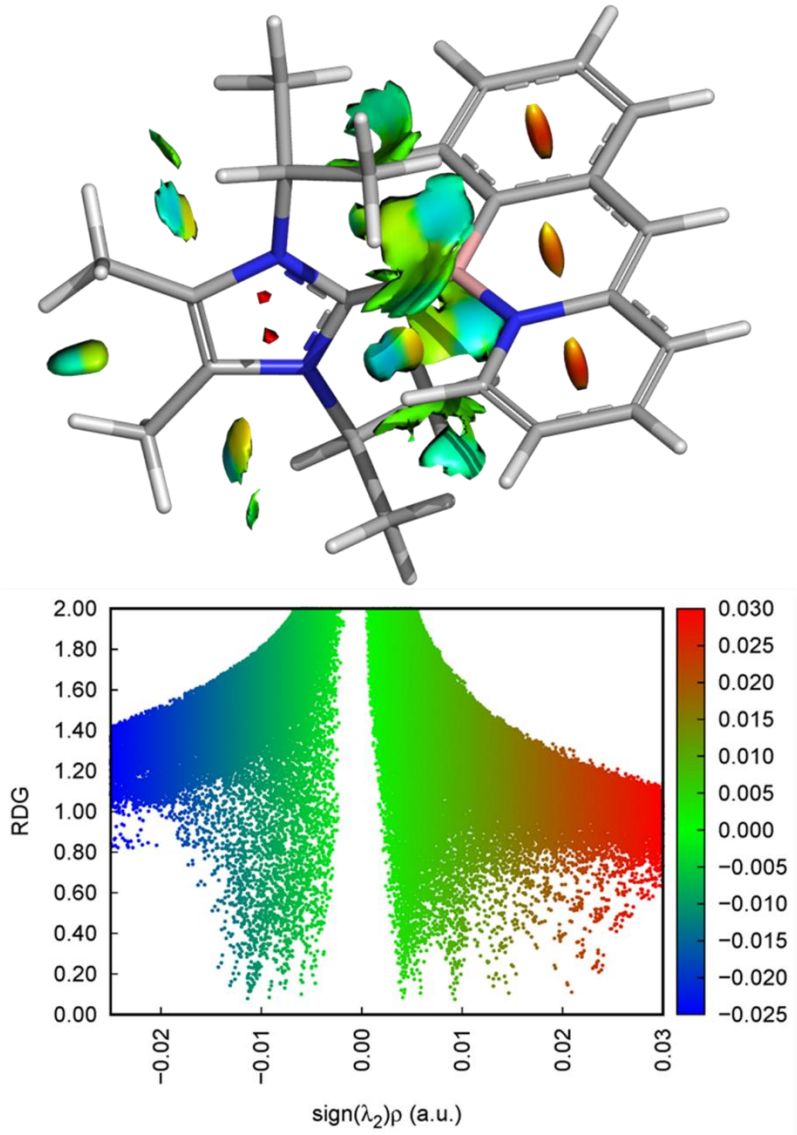

Supplementary Figure 69. Non-covalent interactions (NCI) plots (top) and RDG scatter plots (bottom) of **3a (**calculated from the B3LYP-D3(BJ)/def2-TZVP level of theory). The isosurfaces are colored according to the values of sign $(\lambda_2)\rho(r)$ (ranging from −0.025 to 0.03 a.u., blue to green).

IBO and ETS-NOCV Analysis

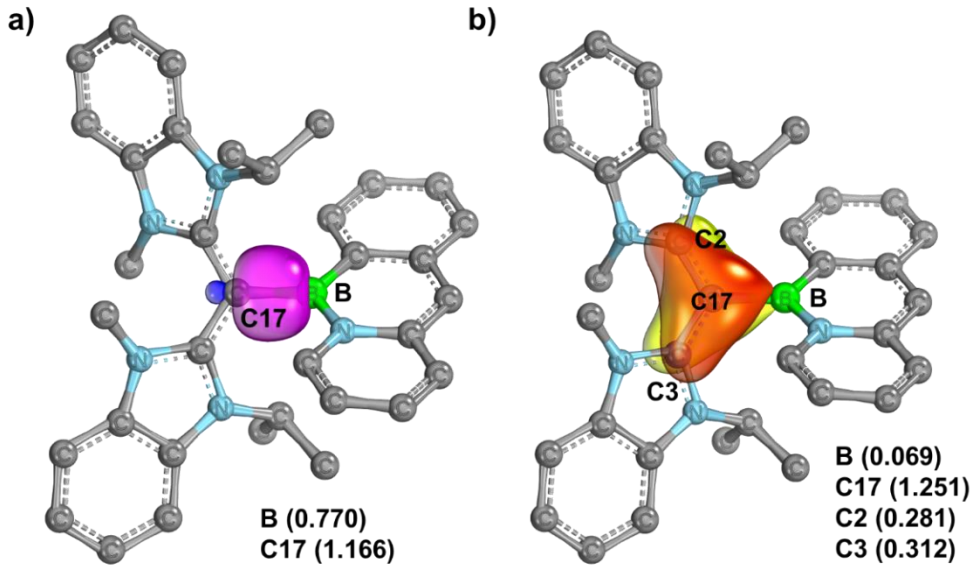

Supplementary Figure 70. Intrinsic bond orbitals depiction of the C1−B σ bond (a) and delocalized 4c-2e$^-$ $\pi_\perp$ bond (b) over the four atoms (C1, C2, C3 and B) associated with C1−B bond within the complex **1a.** Values (in e$^-$) in parentheses are the partial charges for a given IBO assigned to the individual atoms. Hydrogen atoms are removed for clarity. Similar results were obtained for **2a**.

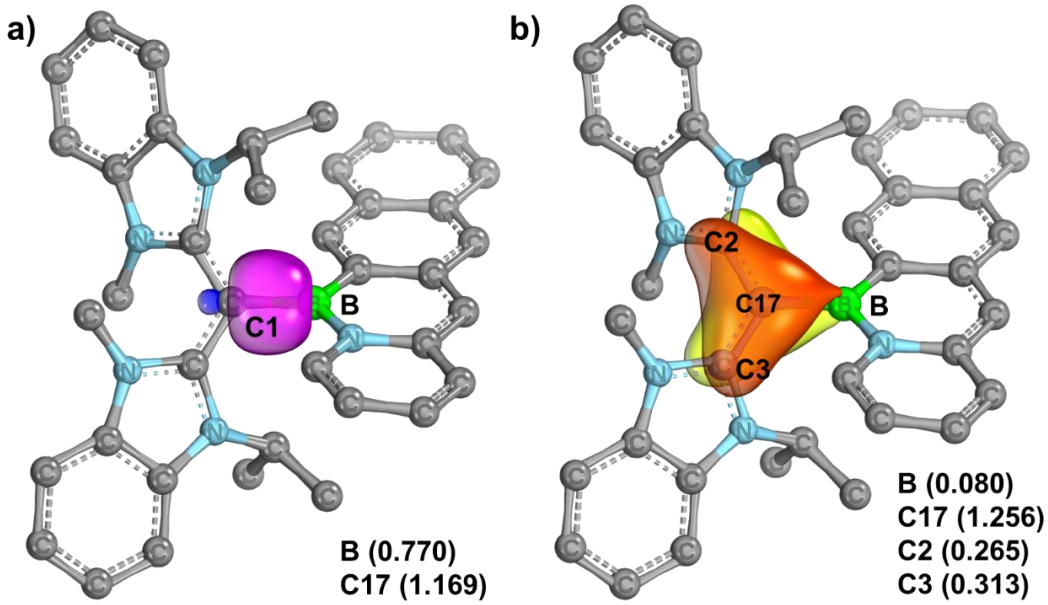

Supplementary Figure 71. Intrinsic bond orbitals depiction of C1−B σ bond (a) and delocalized 4c-2e$^-$ $\pi_\perp$ bond (b) over the four atoms (C1, C2, C3 and B) associated with C1−B bond within the complex **1b**. Values (in e$^-$) in parentheses are the partial charges for a given IBO assigned to the individual atoms. Hydrogen atoms are removed for clarity. Similar results were obtained for **2b**.

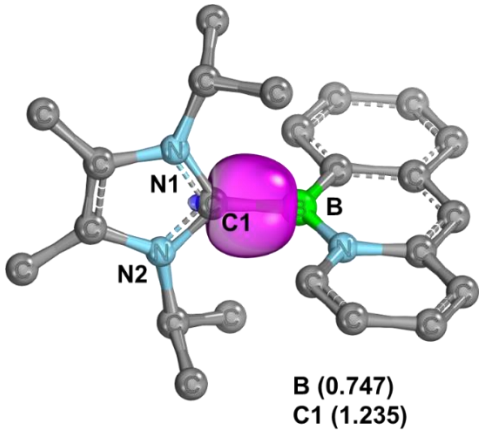

Supplementary Figure 72. Intrinsic bond orbitals depiction for the C1−B σ bond in the complex **3a**. Values (in e^-) in parentheses are the partial charges for the given IBO assigned to the individual atoms. Hydrogen atoms are removed for clarity. No π bond character for the C1−B bond bonding is identified within the charge centering print threshold (0.02 e^-).

Supplementary Table 5. Selected ETS-NOCV results for **1**, **2** and **3a** at B3LYP-D3(BJ)/def2-TZVP level of theory. Energies given in kcal mol^{-1}.

	1a	**2a**	**1b**	**2b**	**3a**
$\Delta E_{\rho 1}$ [a]	−166.38 (72.8%)	−166.11 (72.4%)	−180.70 (72.7%)	−180.21 (72.9%)	−123.91 (74.5%)
$\Delta E_{\rho 2}$ [a]	−14.96 (6.5%)	−14.64 (6.4%)	−18.96 (7.6%)	−17.70 (7.1%)	−10.01 (6.0%)
$\Delta E_{\rho 3}$ [a]	−21.48 (9.4%)	−21.33 (9.3%)	−22.99 (9.2%)	−22.58 (9.1%)	-
$\Delta E_{\text{orb, others}}$ [a]	−25.80 (11.3%)	−27.45 (12.0%)	−25.77 (10.4%)	−25.58 (10.9%)	32.44 (19.5%)
$\Delta E_{\text{orb total}}$	−228.62	−229.53	−248.42	−247.21	−166.35

[a] Values in parentheses give the percentage contribution to the total orbital interactions ΔE_{orb}.

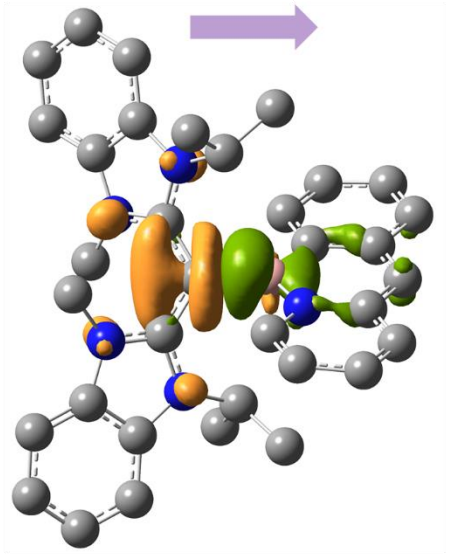

$\Delta E\rho_1 = -166.38$ kcal/mol
$v_1 = 1.035$

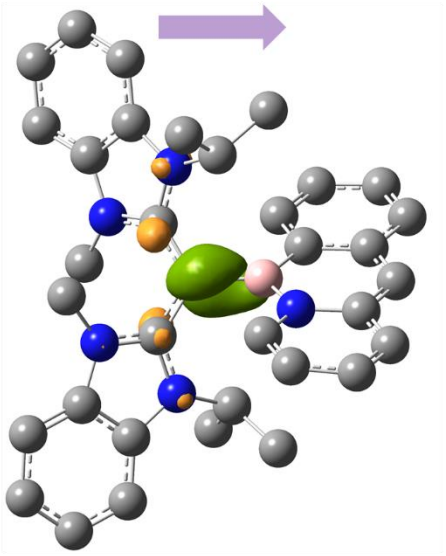

$\Delta E\rho_2 = -14.96$ kcal/mol
$v_2 = 0.431$

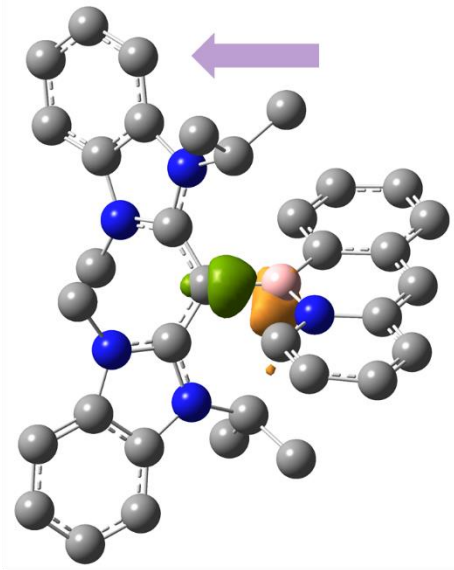

$\Delta E\rho_3 = -21.48$ kcal/mol
$v_3 = 0.366$

Supplementary Figure 73. Contour plots for the deformation densities associated with the dominant orbital interactions $\Delta E\rho_1$, $\Delta E\rho_2$ and $\Delta E\rho_3$ for **1a**. The colors of the deformation densities indicate the flow of electrons from orange to green (isosurface = 0.004 a.u.). $\Delta\rho_1$: σ donation from the ligand to azaboraacene moiety; $\Delta\rho_2$: π donation from the ligand to B−$C_{(carbone)}$ bond; $\Delta\rho_3$: B→C polarization of the B−$C_{(carbone)}$ bond.

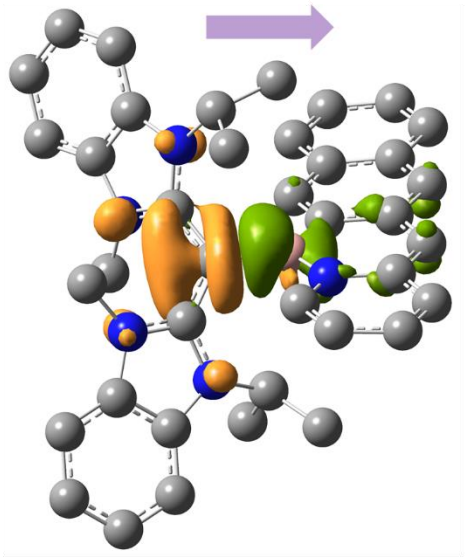

$\Delta E\rho_1 = -180.70$ kcal/mol
$v_1 = 1.109$

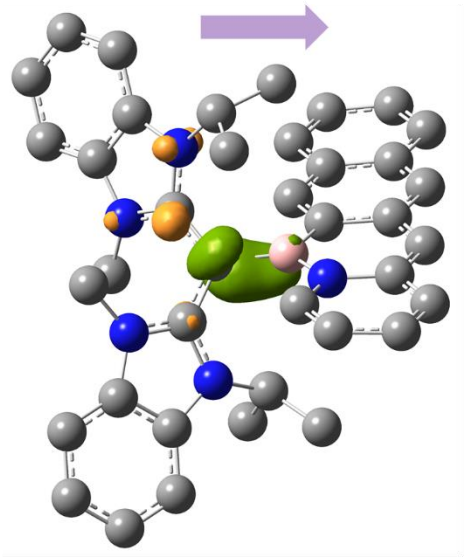

$\Delta E\rho_2 = -18.96$ kcal/mol
$v_2 = 0.464$

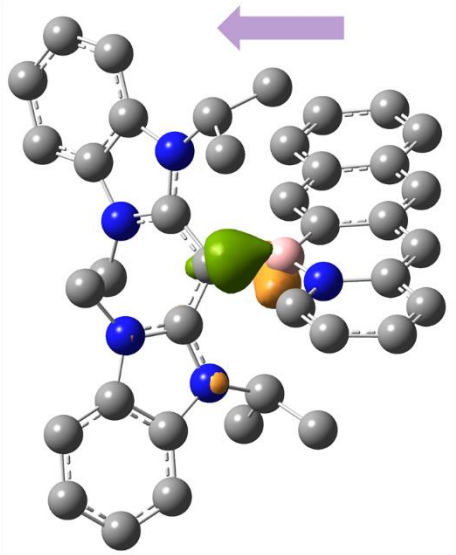

$\Delta E\rho_3 = -22.99$ kcal/mol
$v_3 = 0.386$

Supplementary Figure 74. Contour plots for the deformation densities associated with the dominant orbital interactions $\Delta E\rho_1$, $\Delta E\rho_2$ and $\Delta E\rho_3$ for **1b**. The colors of the deformation densities indicate the flow of electrons from orange to green (isosurface = 0.004 a.u.). $\Delta\rho_1$: σ donation from the ligand to azaboraacene moiety; $\Delta\rho_2$: π donation from the ligand to B−$C_{(carbone)}$ bond; $\Delta\rho_3$: B→C polarization of the B−$C_{(carbone)}$ bond.

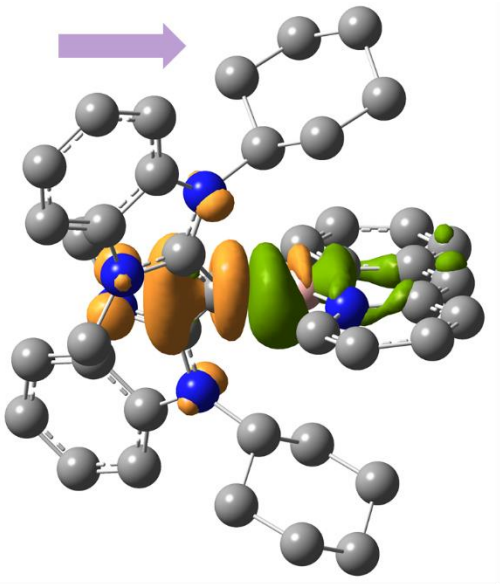

$\Delta E\rho_1 = -166.11$ kcal/mol
$v_1 = 1.032$

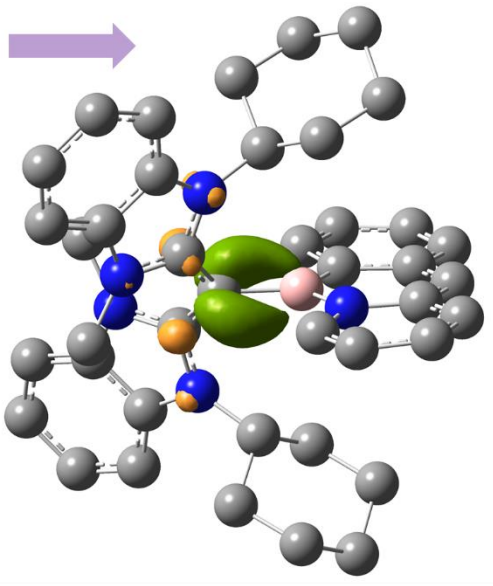

$\Delta E\rho_2 = -14.64$ kcal/mol
$v_2 = 0.426$

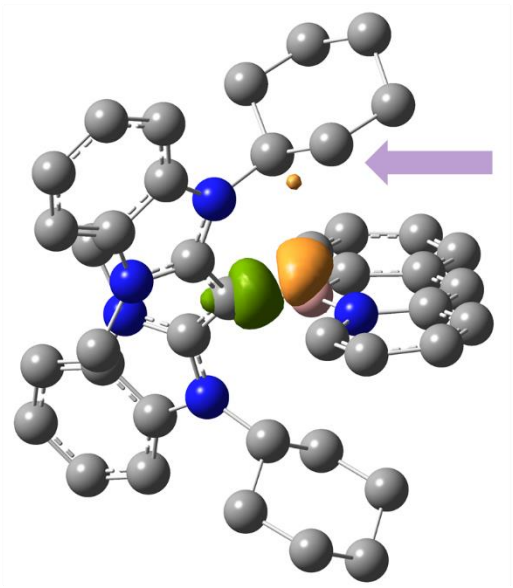

$\Delta E\rho_3 = -21.33$ kcal/mol
$v_3 = 0.365$

Supplementary Figure 75. Contour plots for the deformation densities associated with the dominant orbital interactions $\Delta E\rho_1$, $\Delta E\rho_2$ and $\Delta E\rho_3$ for **2a**. The colors of the deformation densities indicate the flow of electrons from orange to green (isosurface = 0.004 a.u.). $\Delta\rho_1$: σ donation from the ligand to azaboraacene moiety; $\Delta\rho_2$: π donation from the ligand to B−$C_{(carbone)}$ bond; $\Delta\rho_3$: B→C polarization of the B−$C_{(carbone)}$ bond.

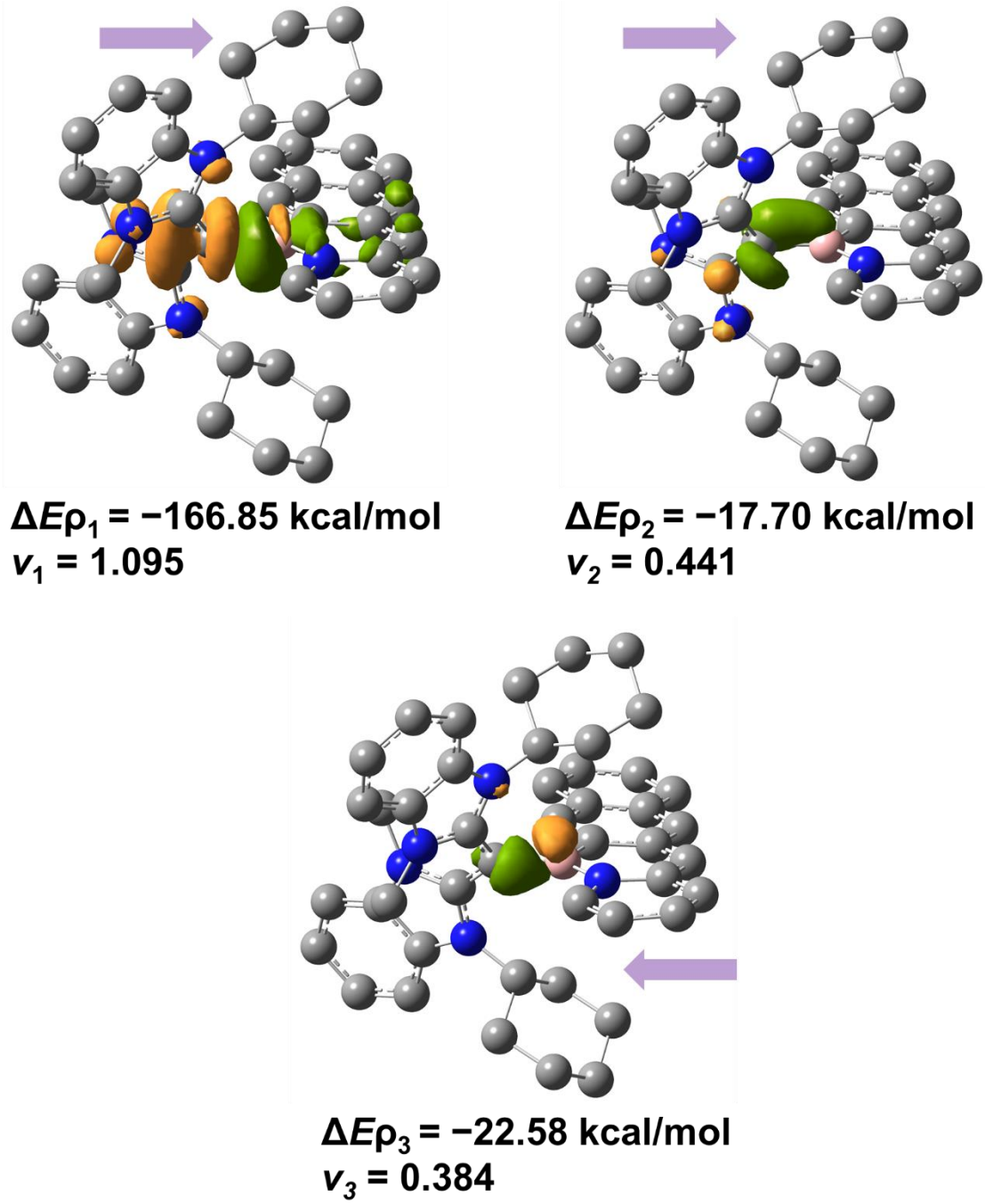

Supplementary Figure 76. Contour plots for the deformation densities associated with the dominant orbital interactions $\Delta E\rho_1$, $\Delta E\rho_2$ and $\Delta E\rho_3$ for **2b**. The colors of the deformation densities indicate the flow of electrons from orange to green (isosurface = 0.004 a.u.). $\Delta\rho_1$: σ donation from the ligand to azaboraacene moiety; $\Delta\rho_2$: π donation from the ligand to B−$C_{(carbone)}$ bond; $\Delta\rho_3$: B→C polarization of the B−$C_{(carbone)}$ bond.

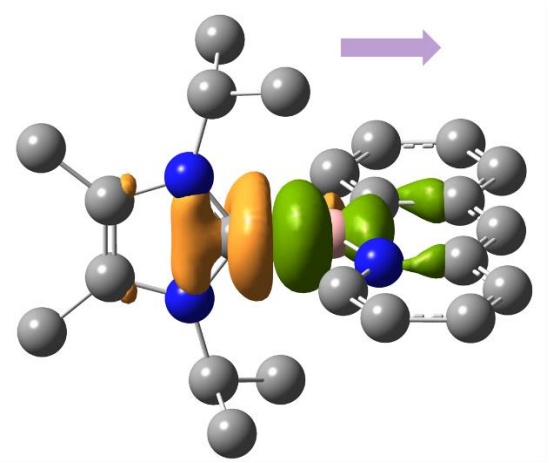

$\Delta E\rho_1 = -123.91$ kcal/mol
$v_1 = 0.732$

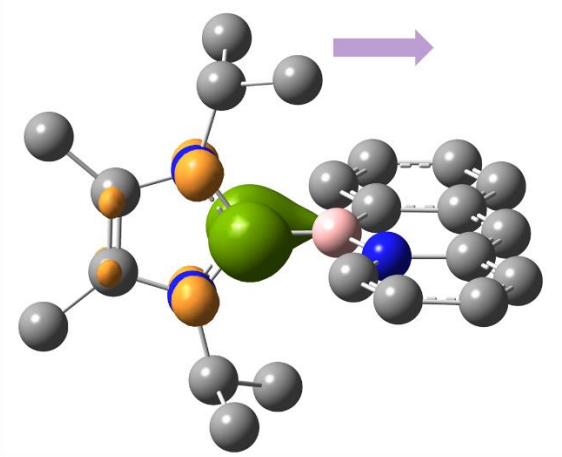

$\Delta E\rho_2 = -10.01$ kcal/mol
$v_2 = 0.318$

Supplementary Figure 77. Contour plots for the deformation densities associated with the dominant orbital interactions $\Delta E\rho_1$ and $\Delta E\rho_2$ for **3a**. The colors of the deformation densities indicate the flow of electrons from orange to green (isosurface = 0.004 a.u.). $\Delta\rho_1$: σ donation from the ligand to azaboraacene moiety; $\Delta\rho_2$: π donation from the ligand to B−$C_{(carbene)}$ bond.

Natural Population Charges (NPA) Analysis

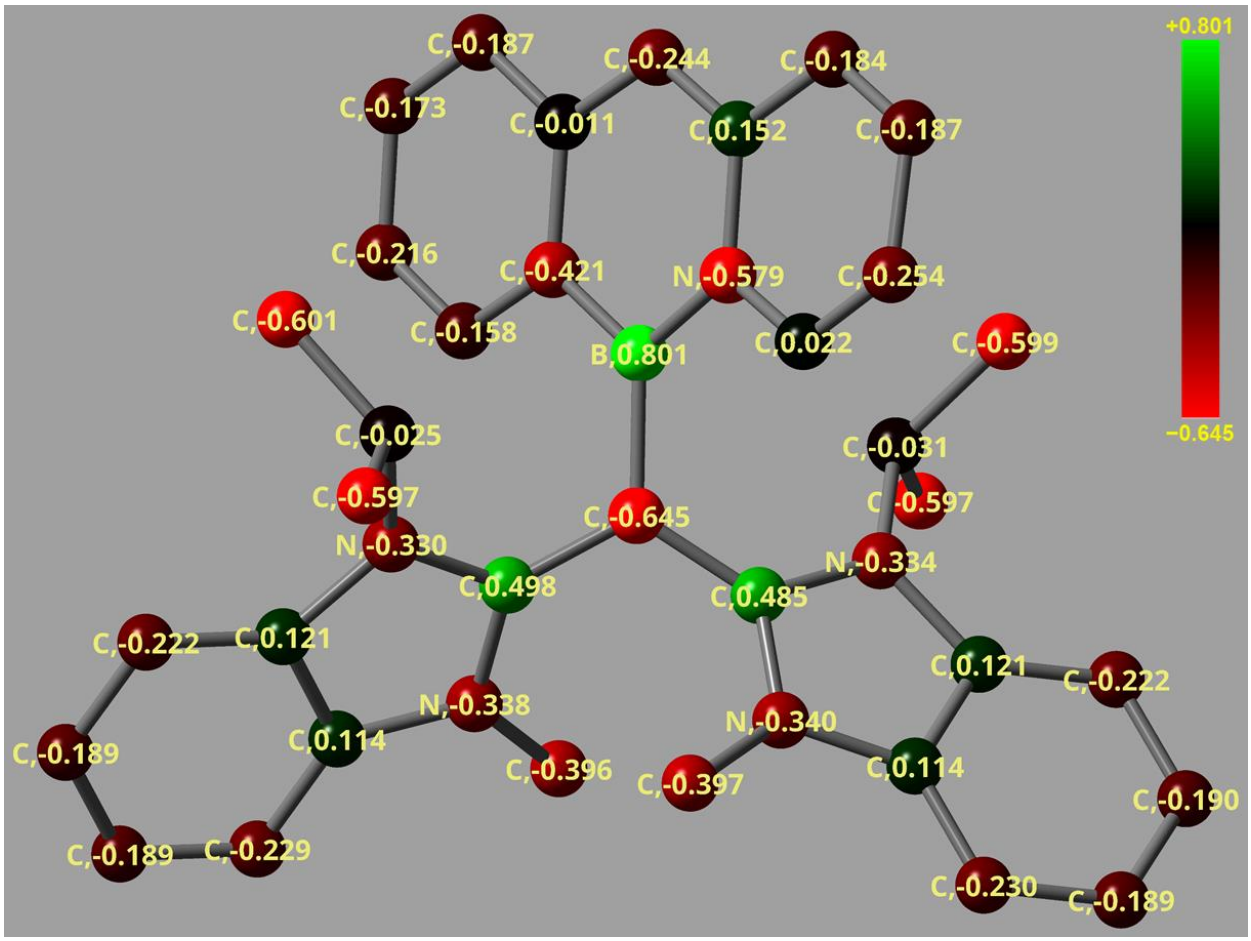

Supplementary Figure 78. NPA charge distribution on the optimized **1a** (at B3LYP-D3(BJ)/def2-TZVP level of theory) with color scheme and scale (bright red for '−' charge and bright green for '+' charge). The numerical values indicate the NPA charges for the respective atom.

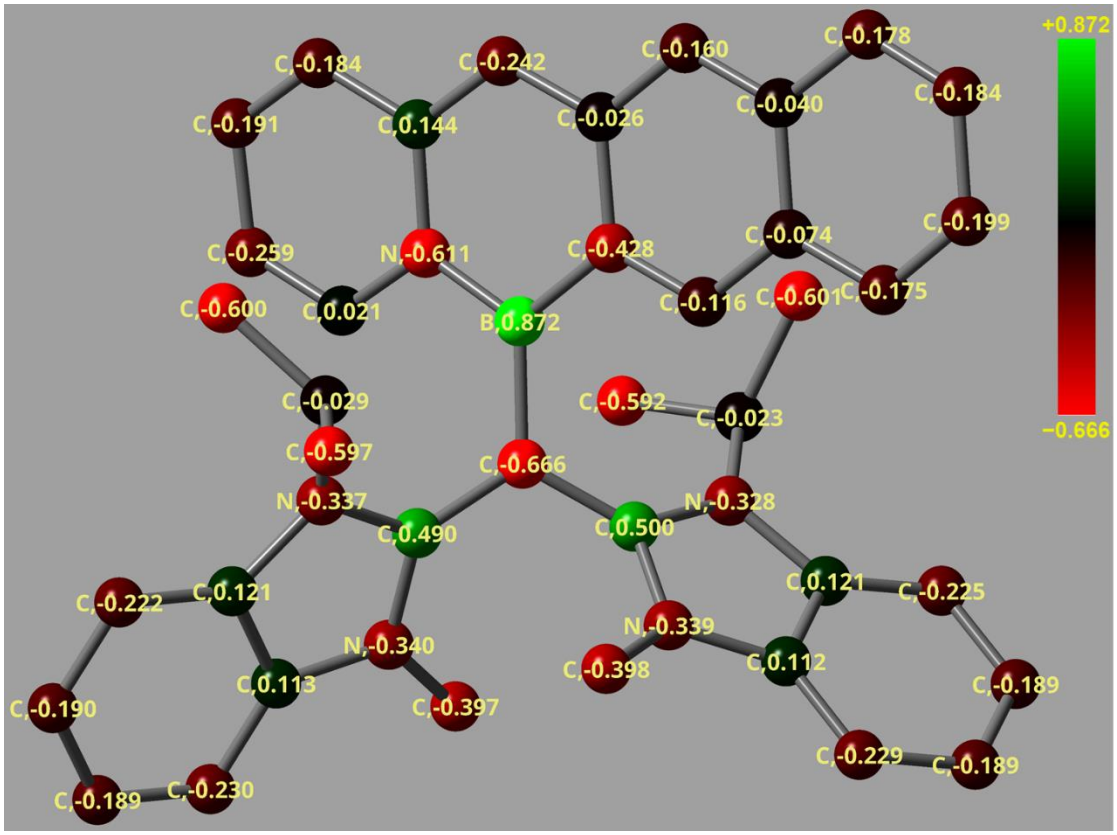

Supplementary Figure 79. NPA charge distribution on the optimized **1b** (at B3LYP-D3(BJ)/def2-TZVP level of theory) with color scheme and scale (bright red for '−' charge and bright green for '+' charge). The numerical values indicate the NPA charges for the respective atom.

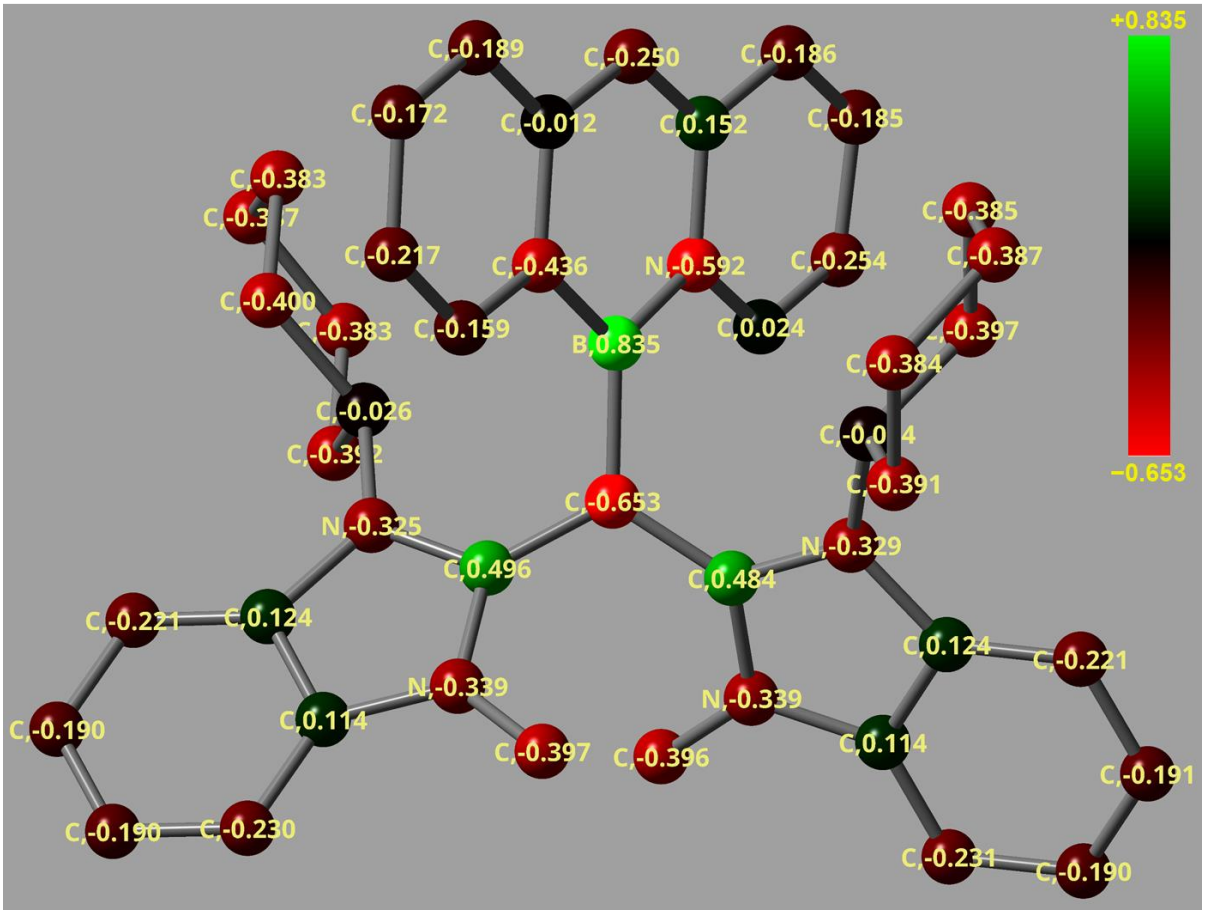

Supplementary Figure 80. NPA charge distribution on the optimized **2a** (at B3LYP-D3(BJ)/def2-TZVP level of theory) with color scheme and scale (bright red for '−' charge and bright green for '+' charge). The numerical values indicate the NPA charges for the respective atom.

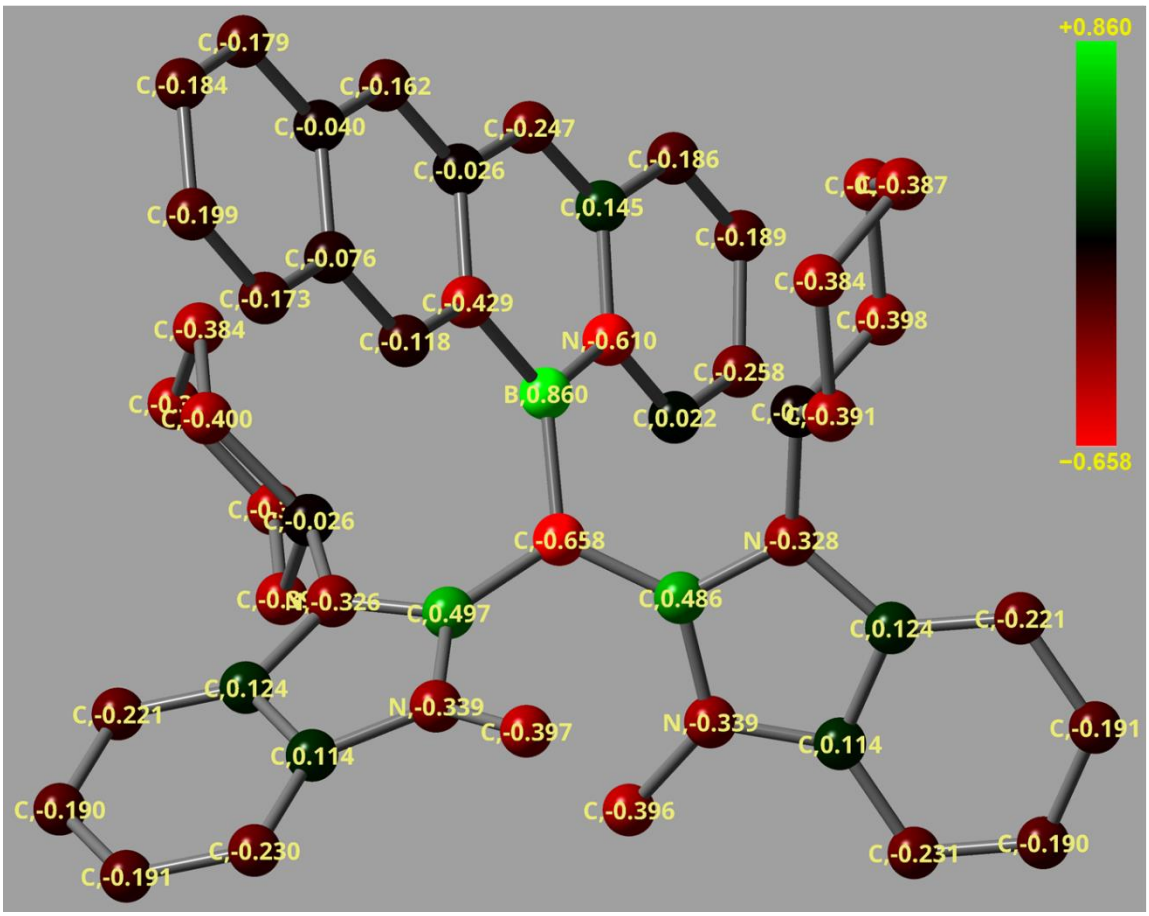

Supplementary Figure 81. NPA charge distribution on the optimized **2b** (at B3LYP-D3(BJ)/def2-TZVP level of theory) with color scheme and scale (bright red for '−' charge and bright green for '+' charge). The numerical values indicate the NPA charges for the respective atom.

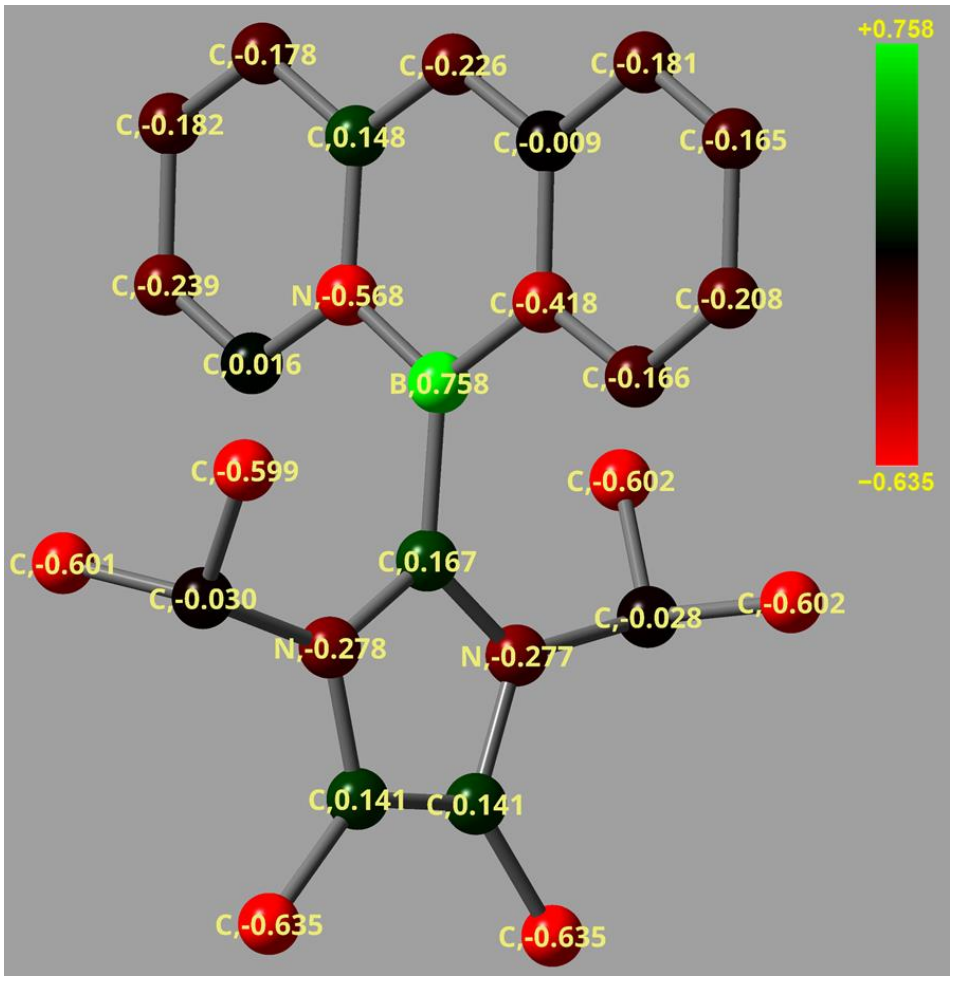

Supplementary Figure 82. NPA charge distribution on the optimized **3a** (at B3LYP-D3(BJ)/def2-TZVP level of theory) with color scheme and scale (bright red for '−' charge and bright green for '+' charge). The numerical values indicate the NPA charges for the respective atom.

Aromaticity Analysis

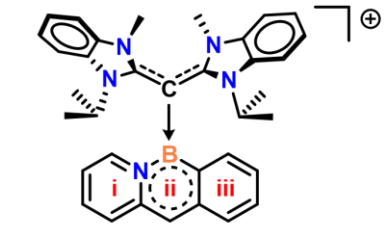

ring	NICS(1)	NICS(1)$_{zz}$
i	−4.30	−11.40
ii	−8.00	−23.07
iii	−10.33	−28.73

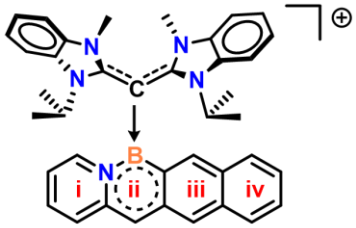

ring	NICS(1)	NICS(1)$_{zz}$
i	−3.06	−7.01
ii	−6.41	−17.86
iii	−12.38	−32.77
iv	−10.27	−26.64

Supplementary Figure 83. NICS(1) and NICS(1)$_{ZZ}$ values (in ppm, calculated at B3LYP/pcSseg-2//B3LYP-D3(BJ)/def2-TZVP level of theory) for each ring in **1a** (left) and **1b** (right).

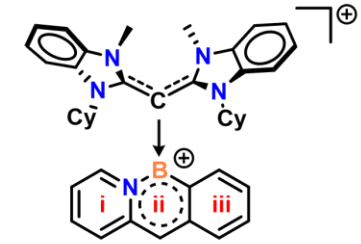

ring	NICS(1)	NICS(1)$_{zz}$
i	−4.23	−11.92
ii	−7.94	−25.17
iii	−10.28	−29.58

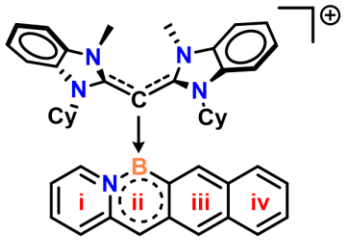

ring	NICS(1)	NICS(1)$_{zz}$
i	−3.01	−8.36
ii	−6.77	−21.47
iii	−12.24	−33.88
iv	−9.97	−26.74

Supplementary Figure 84. NICS(1) and NICS(1)$_{ZZ}$ values (in ppm, calculated at B3LYP/pcSseg-2//B3LYP-D3(BJ)/def2-TZVP level of theory) for each ring in **2a** (left) and **2b** (right).

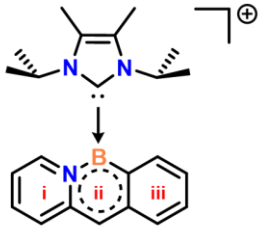

ring	NICS(1)	NICS(1)$_{zz}$
i	−4.83	−11.92
ii	−9.10	−24.81
iii	−10.55	−28.57

Supplementary Figure 85. NICS(1) and NICS(1)$_{ZZ}$ values (in ppm, calculated at B3LYP/pcSseg-2//B3LYP-D3(BJ)/def2-TZVP level of theory) for each ring in **3a**.

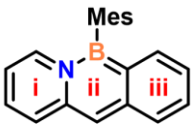

ring	NICS(1)	NICS(1)$_{zz}$
i	−3.64	−9.50
ii	−7.77	−21.80
iii	−10.08	−28.60

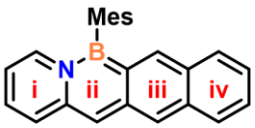

ring	NICS(1)	NICS(1)$_{zz}$
i	−2.51	−6.12
ii	−6.74	−17.90
iii	−11.98	−32.86
iv	−9.63	−26.69

Supplementary Figure 86. NICS(1) and NICS(1)$_{ZZ}$ values (in ppm, calculated at B3LYP/pcSseg-2//B3LYP-D3(BJ)/def2-TZVP level of theory) for each ring in the neutral BN-anthracene **6a** (left) and BN tetracene **6b** (right).

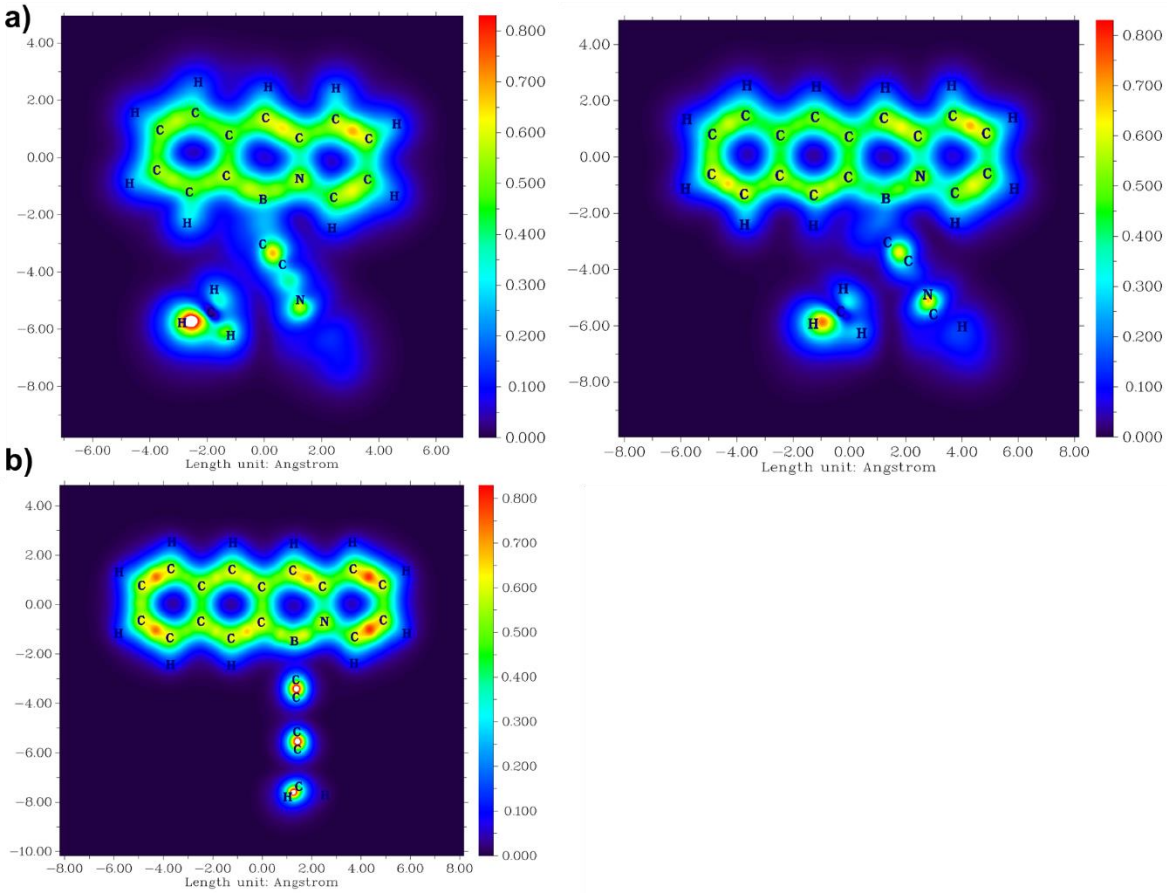

Supplementary Figure 87. a) The localized orbital indicator function (LOL-π (calculated at the B3LYP/def2-TZVP level of theory) for the BN-doped molecular plane of **2a** (left) and **2b** (right); b) **6b**. The green band shows that π-electrons within the bonds are effectively 1delocalized, and red color indicates partially localized.

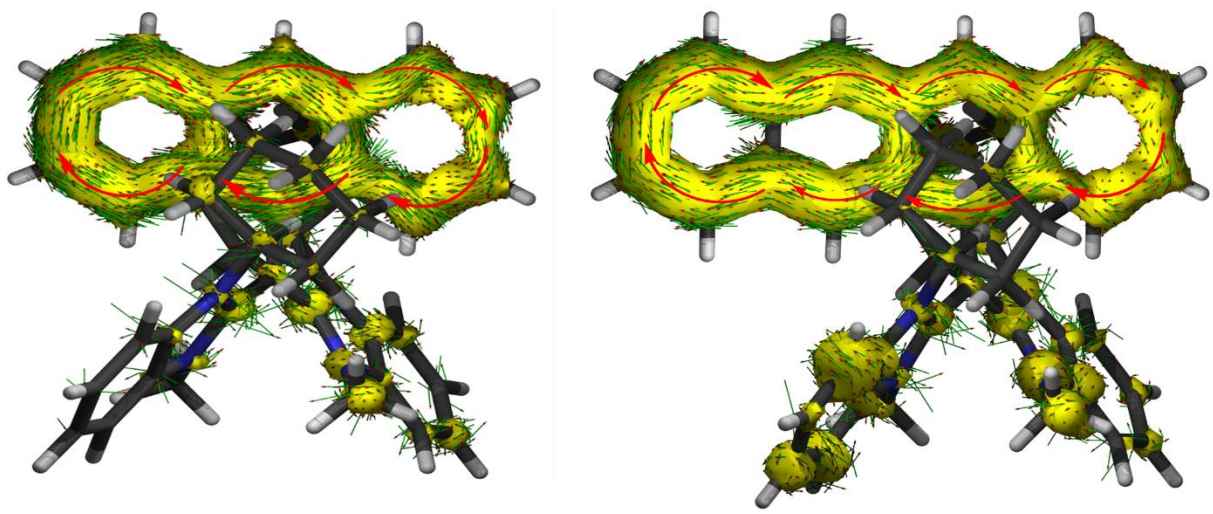

Supplementary Figure 88. ACID plots (contribution from π electrons only) of **2a** (left) and **2b** (right). The isovalue is 0.03, and the diamagnetic (clockwise) ring currents under the magnetic field parallel to the *z*-axis are highlighted by red arrows, the direction of magnetic field is orthogonal to the molecular plane and points upward.

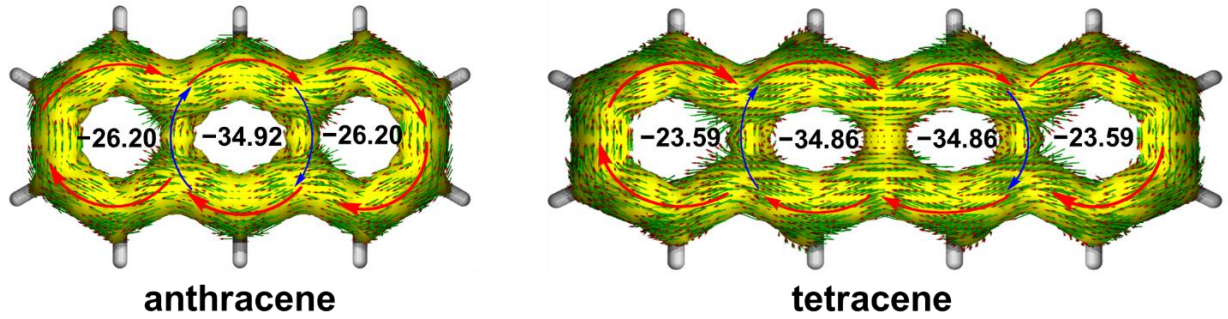

Supplementary Figure 89. ACID plots (contribution from π electrons only) of all-carbon anthracene (left) and tetracene (right). The isovalue is 0.03, and the diamagnetic (clockwise) ring currents under the magnetic field parallel to the *z*-axis are highlighted by red arrows, the direction of magnetic field is orthogonal to the molecular plane and points upward. NICS(1)$_{ZZ}$ values (in ppm, calculated at B3LYP/pcSseg-2//B3LYP-D3(BJ)/def2-TZVP level of theory) for each ring were marked in each ring. The reduced aromaticity for the outer six-membered rings of acenes is due to the 'cancelling out' effect (clockwise blue arrows) from the local ring current in the central rings, which also found in the fully conjugated BN acene systems.

TD-DFT Calculations

The TD-DFT vertical excitation calculations were performed at the B3LYP-D3(BJ)/ma-def2-TZVP//B3LYP-D3(BJ)/def2-TZVP level of theory using Gaussian 16 Rev B.01.[22] It is well-known that the reliability of the TDDFT results strongly depends on the choice of the exchange-correlation functional, additional hybrid functions such as TPPSh-D3(BJ) (10% HF exchange), PBE0-D3(BJ) (25% HF exchange) theory and long-range-corrected CAM-B3LYP-D3(BJ) (composed of 19% HF exchange at short-range and 65% HF exchange at long-range, ideally for charge-transfer (CT) excitations) with the unified *ma*-def2-TZVP basis set[38,39] were also evaluated on **1b** (Supplementary Figure 90a). The results suggest that TPPSh-D3(BJ) and PBE0-D3(BJ) theory reproduced the trend in the experimental spectra of all the cations, and B3LYP-D3(BJ) (20% HF exchange) yielded the most reliable energy ordering and the excitation energies in the excited states for all the compounds. The CAM-B3LYP-D3(BJ) method led to significantly blue-shifted electronic transition energies (> 0.3 eV) with respect to the experimental values and failed to reproduce the experimentally obtained absorption characteristics, which further validated the local excitation (LE) transition characters for these types of compounds. The optimizations and single-point TD-DFT calculations were performed in solvent using the conductor-like polarisable continuum model (CPCM)[40] with parameters for toluene. Both the state-specific (SS)[41] and corrected-linear response (cLR)[42] approaches were assessed, and the difference are minimal (within 2 nm) due to the small change of the electron density for vertical excitation/de-excitations. Thus, the cLR scheme is sufficient for describing the environment response in solution.[43] Due to the fact that possible vibrational progression on the rigid azaboraacene frameworks may couple with the absorption band, vibrationally-resolved UV-Vis absorption spectra (only for $S_1 \rightarrow S_0$ transitions in **1b** and **3a** due to the significantly large computational costs found in analogues **2**) were predicted based on the Franck-Condon analysis,[44,45] as it is implemented in Gaussian 16. The ground and excited state optimizations and frequency calculations were obtained at the B3LYP-D3(BJ)/ TZVP level of theory in implicit solvent (toluene) *via* PCM.

Separately, since the longer linearly fused acene-like molecules may exhibit potential multireference characters,[46] the electronic structures of chromophores **1a** and **1b** in their ground states were further evaluated using the T1 diagnostics, which were calculated at the DLPNO-CCSD(T)/cc-pVTZ levels of theory after checking the stabilities of their KS-DFT wavefunctions. The T1 diagnostics values for **1a** and **1b** are calculated to be 0.0111 and 0.0114, respectively, which are significantly smaller than the 0.02 threshold (for main group species).[31] Furthermore, we performed fractional occupation number weighted density (FOD) calculations[29] as a static electron correlation diagnostic to analyze the ground sate electronic structures of **1a**, **1b** as well as the all-carbon acenes. The FOD plot provides reliable information on the localization of "hot" (strongly correlated and chemically active) electrons in a molecule. As shown in Supplementary Figure 90b, the 'hot' electrons spatial distribution at the atoms of **1a** and **1b** are highly localized and less visible than their parent all-carbon acenes, suggesting even weaker multireference cases among BN-anthracenium and -tetracenium ions than the short-length acenes. Therefore, we believe that the single-reference results presented in this study are reliable predictions.

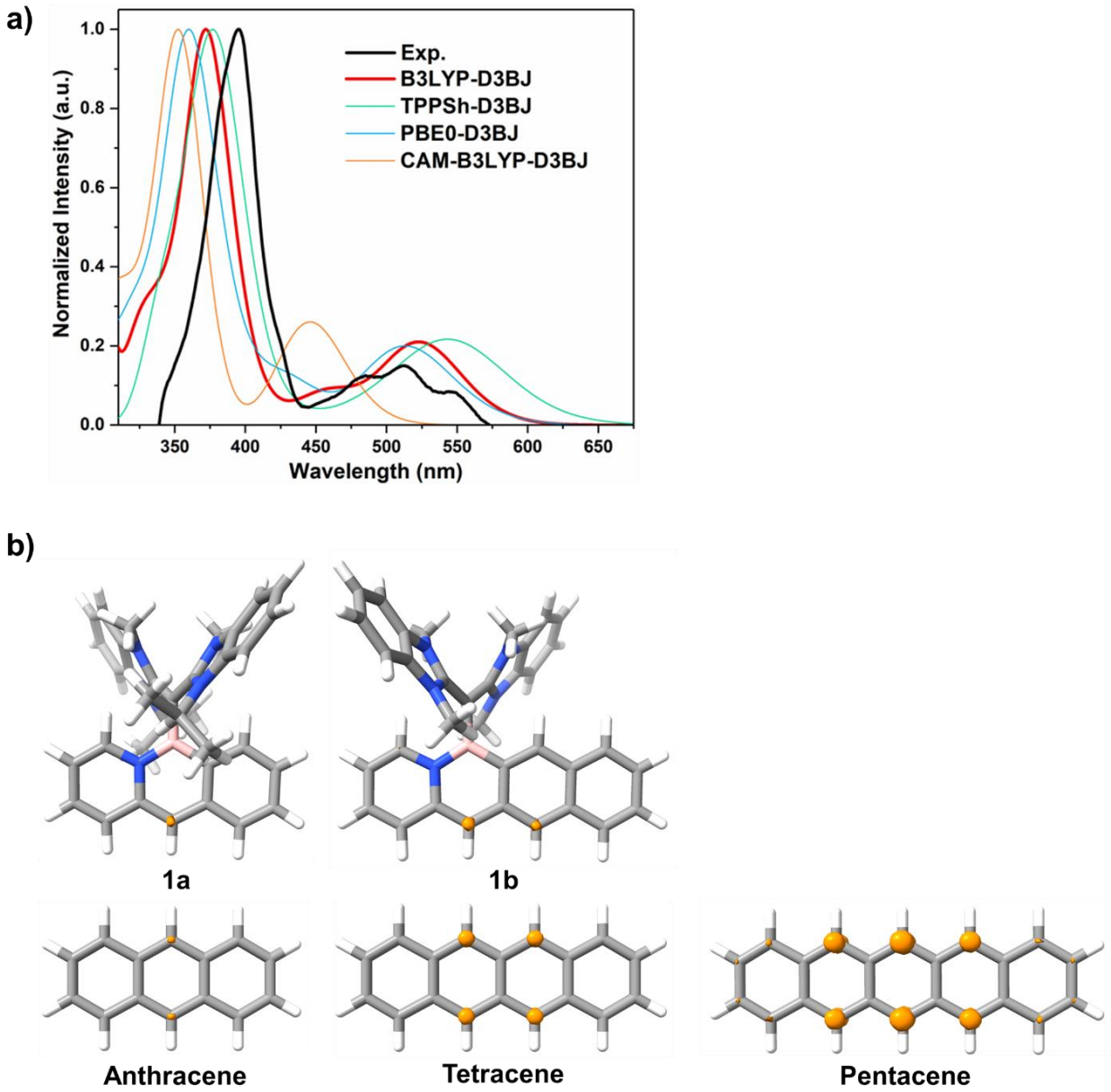

Supplementary Figure 90. a) Comparing the TD-DFT performance of B3LYP-D3(BJ), TPPSh-D3(BJ), PBE0-D3(BJ) and CAM-B3LYP-D3(BJ) using toluene as an implicit solvent. All the spectra have been normalized to compare with the experimental spectrum of **1b**. All the spectra were obtained at the *ma*-def2-TZVP level of theory and were plotted using a full width at half maximum (FWHM) of 0.35 eV. It found that the CAM-B3LYP-D3(BJ) yield a very large error (> 0.3 eV) on excitation energy and the relative intensity of experimental spectrum. b) FOD plots (at σ=0.005 e Bohr^{-3}, TPSS/def2-TZVP, T_{el}= 5000 K) of **1a**, **1b**, anthracene, tetracene and pentacene. (FOD shown in orange).

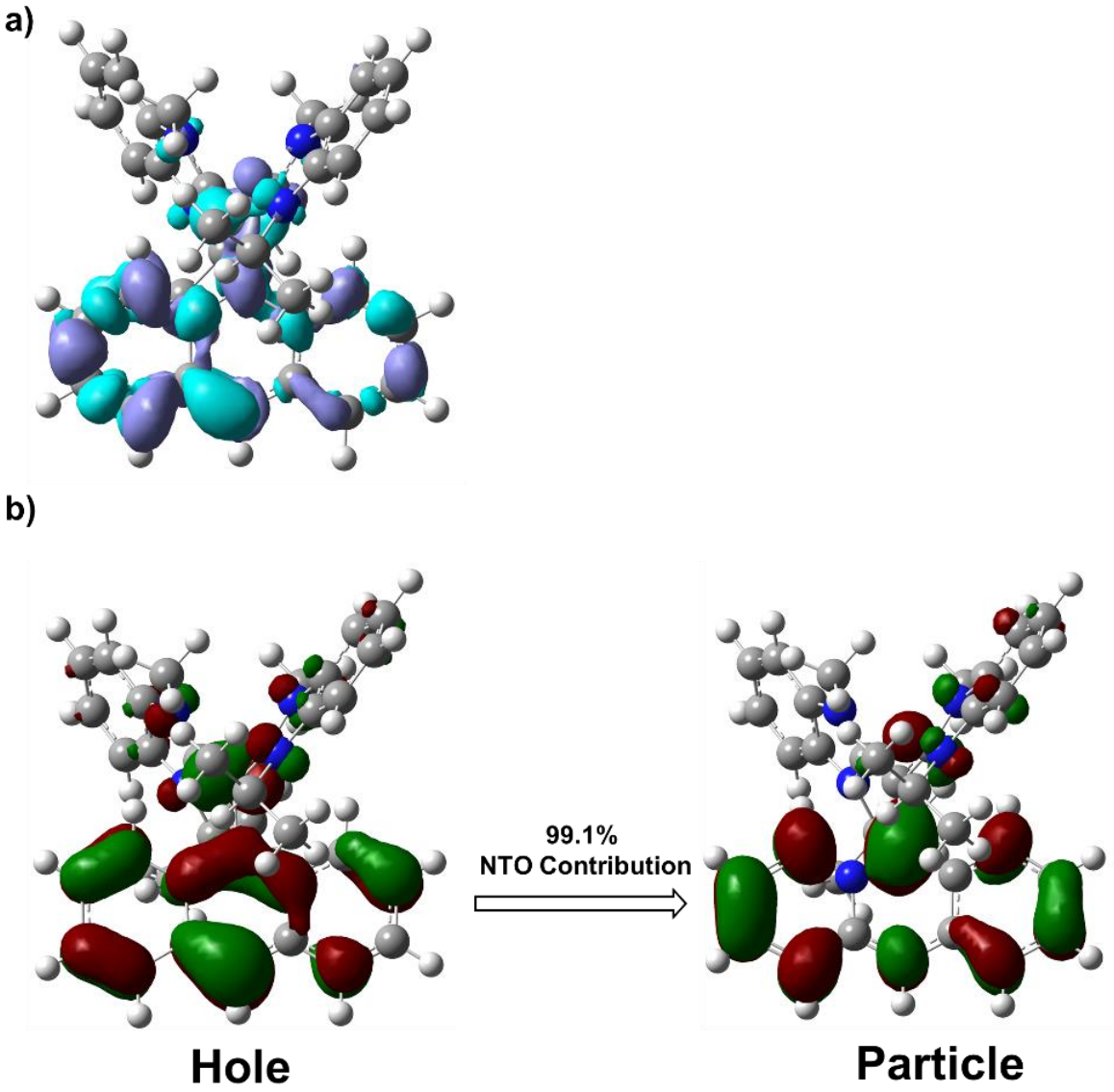

Supplementary Figure 91. a) Electron density difference (EDD) plots between ground state (S_0) and first excited state (S_1) of **1a**. The purple areas indicate density accumulation and cyan areas indicate density depletion in transition. b) Natural transition orbitals (NTO, occupied transition orbitals: hole; unoccupied transition orbitals: particle) for the $S_0 \rightarrow S_1$ vertical transition of **1a**, suggesting its dominant π to π* transition character. The isovalue is 0.03, and calculations were performed at (PCM, toluene)-B3LYP-D3(BJ)/ma-def2-TZVP//B3LYP-D3(BJ)/def2-TZVP level of theory.

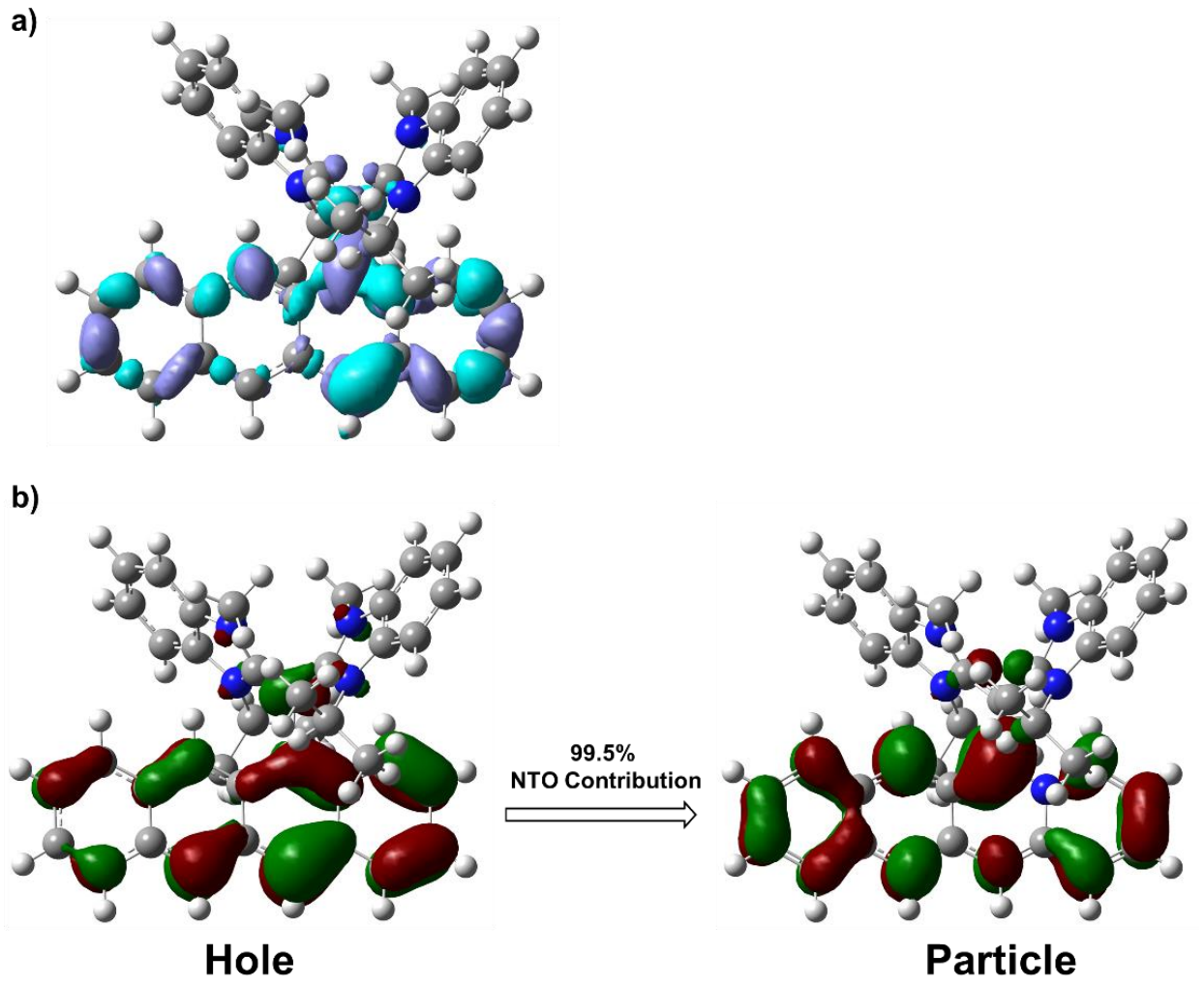

Supplementary Figure 92. a) Electron density difference (EDD) plots between ground state (S_0) and first excited state (S_1) of **1b**. The purple areas indicate density accumulation and cyan areas indicate density depletion in transition. b) Natural transition orbitals (NTO, occupied transition orbitals: hole; unoccupied transition orbitals: particle) for the $S_0 \rightarrow S_1$ vertical transition of **1b**, suggesting its dominant π to π* transition character. The isovalue is 0.03, and calculations were performed at (PCM, toluene)-B3LYP-D3(BJ)/ma-def2-TZVP//B3LYP-D3(BJ)/def2-TZVP level of theory.

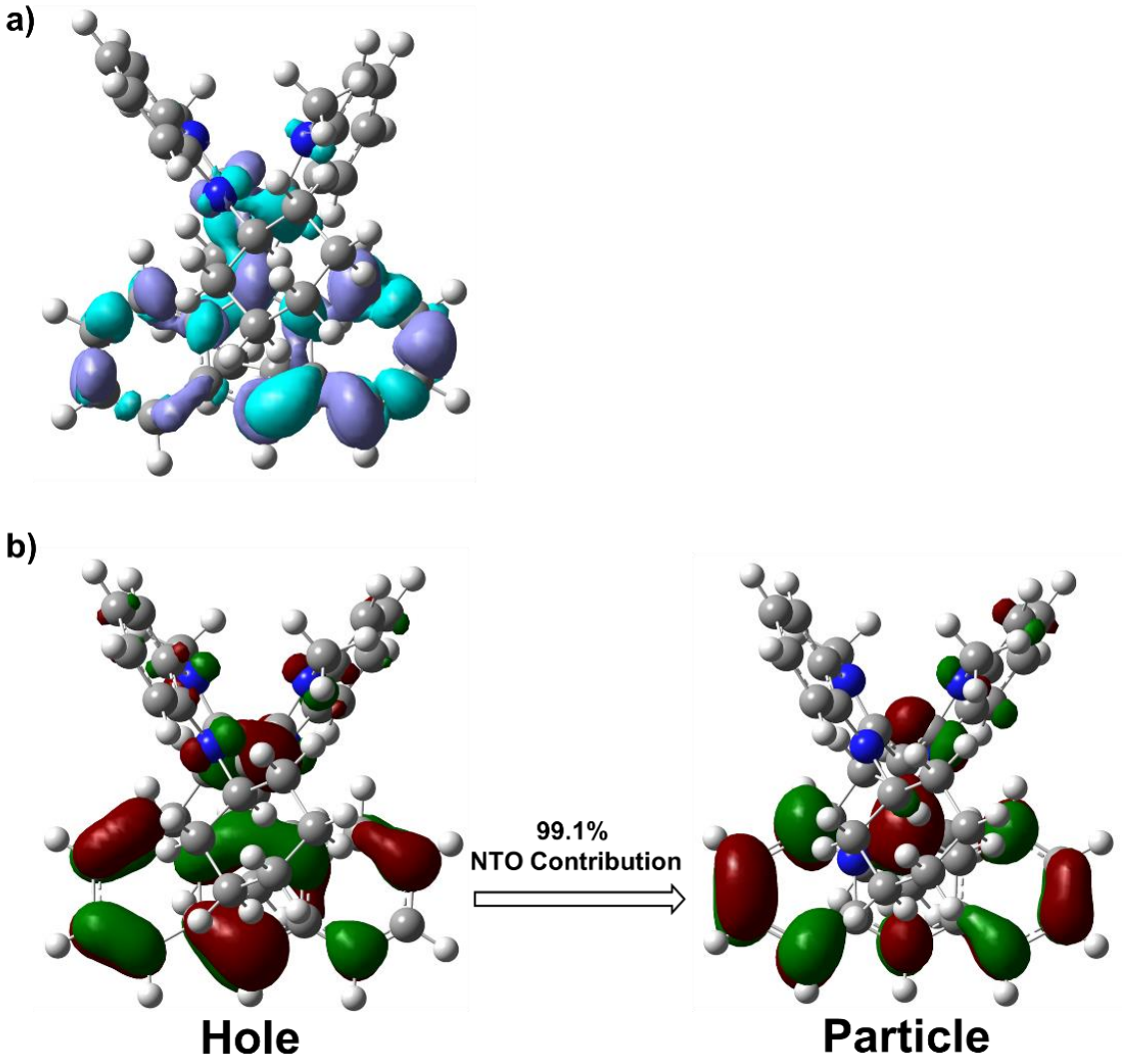

Supplementary Figure 93. a) Electron density difference (EDD) plots between ground state (S_0) and first excited state (S_1) of **2a**. The purple areas indicate density accumulation and cyan areas indicate density depletion in transition. b) Natural transition orbitals (NTO, occupied transition orbitals: hole; unoccupied transition orbitals: particle) for the $S_0 \rightarrow S_1$ vertical transition of **2a**, suggesting its dominant π to π* transition character. The isovalue is 0.03, and calculations were performed at (PCM, toluene)-B3LYP-D3(BJ)/ma-def2-TZVP//B3LYP-D3(BJ)/def2-TZVP level of theory.

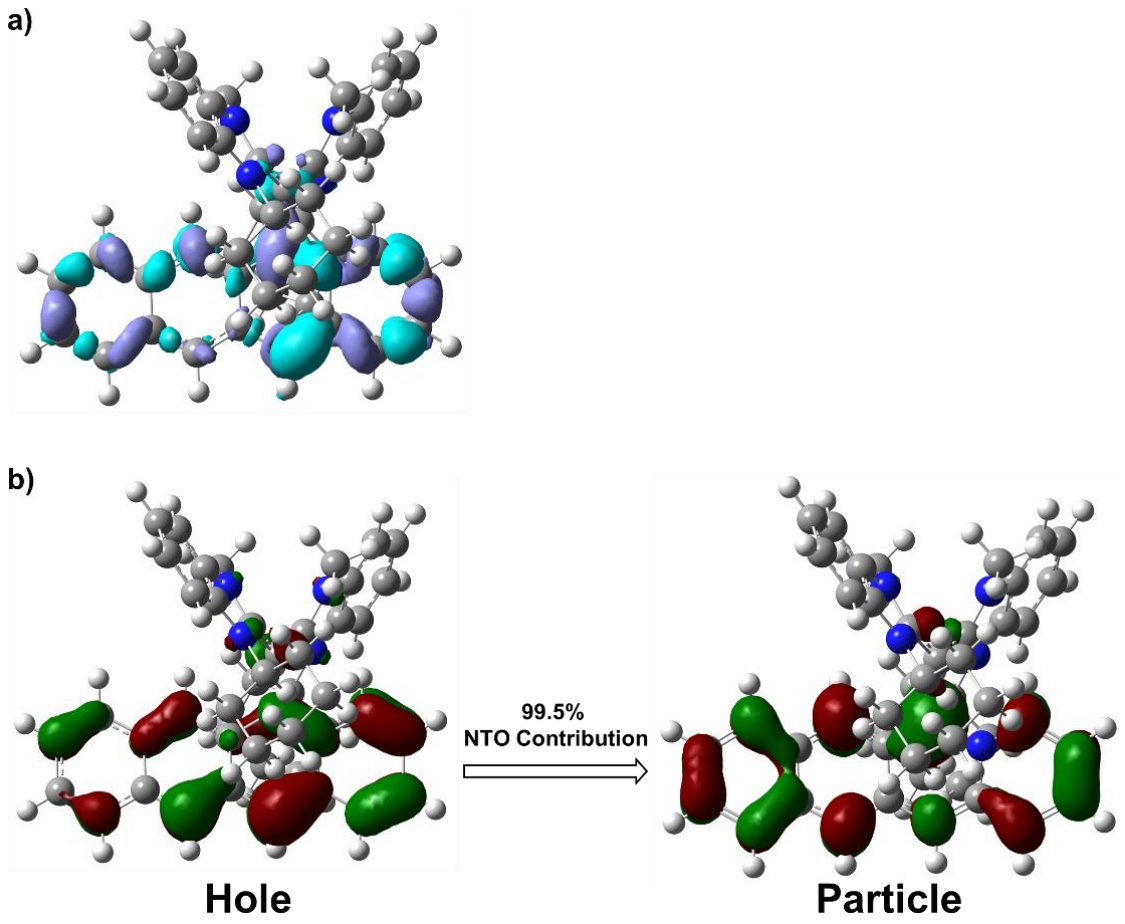

Supplementary Figure 94. a) Electron density difference (EDD) plots between ground state (S_0) and first excited state (S_1) of **2b**. The purple areas indicate density accumulation and cyan areas indicate density depletion in transition. b) Natural transition orbitals (NTO, occupied transition orbitals: hole; unoccupied transition orbitals: particle) for the $S_0 \rightarrow S_1$ vertical transition of **2b**, suggesting its dominant π to π* transition character. The isovalue is 0.03, and calculations were performed at (PCM, toluene)-B3LYP-D3(BJ)/ma-def2-TZVP//B3LYP-D3(BJ)/def2-TZVP level of theory.

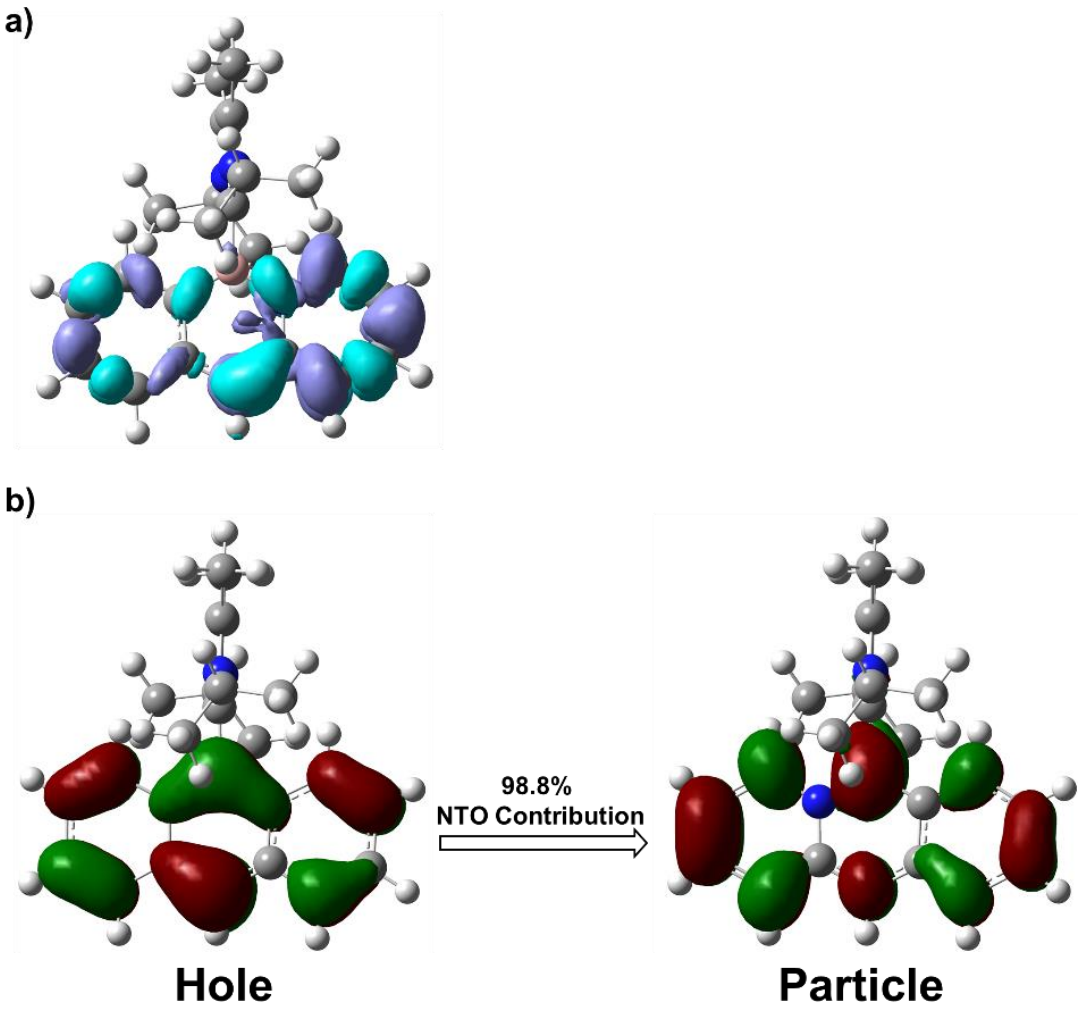

Supplementary Figure 95. a) Electron density difference (EDD) plots between ground state (S_0) and first excited state (S_1) of **3a**. The purple areas indicate density accumulation and cyan areas indicate density depletion in transition. b) Natural transition orbitals (NTO, occupied transition orbitals: hole; unoccupied transition orbitals: particle) for the $S_0 \rightarrow S_1$ vertical transition of **3a**, suggesting its dominant π to π* transition character. The isovalue is 0.03, and calculations were performed at (PCM, toluene)-B3LYP-D3(BJ)/ma-def2-TZVP//B3LYP-D3(BJ)/def2-TZVP level of theory.

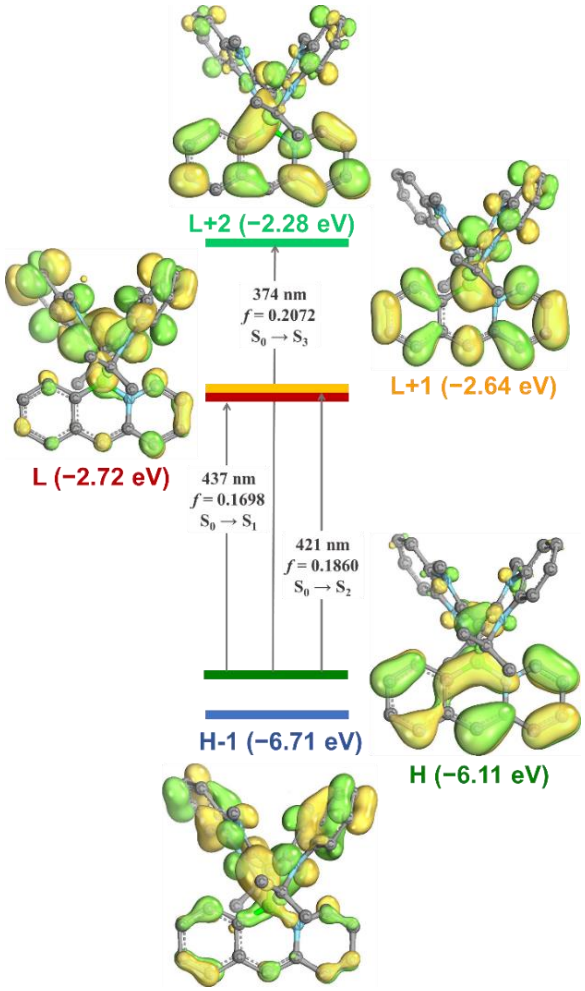

Supplementary Figure 96. Kohn–Sham molecular orbitals (HOMO-1, HOMO, LUMO, LUMO+1 and LUMO+2) and their orbital energies of **1a**. All the calculations were performed by the TD-DFT methods at (PCM, toluene)-B3LYP-D3(BJ)/ma-def2-TZVP//B3LYP-D3(BJ)/def2-TZVP level of theory. (H: HOMO, L: LUMO). The electronic transitions $S_0 \rightarrow S_1$ and $S_0 \rightarrow S_2$ are predominantly derived from vertical excitations to the LUMO and LUMO+1 from the HOMO, respectively. The LUMO (−2.72 eV) and LUMO+1 (−2.65 eV) in **1a** are energetically comparable and the second excited singlet (S_2) state is slightly above its S_1 state.

Supplementary Table 6 Selected wavelength, oscillator strength (*f*) and major configurations from the TD-DFT calculation (at the B3LYP-D3(BJ)/ma-def2-TZVP//B3LYP-D3(BJ)/def2-TZVP (PCM, toluene) level of theory) for **1a**

	λ_{cal} (nm)	electronic transitions	*f*	Major configurations
1a	437	$S_1 \leftarrow S_0$	0.1698	HOMO→LUMO (97%)
	420	$S_2 \leftarrow S_0$	0.1860	HOMO→LUMO+1 (98%)
	374	$S_3 \leftarrow S_0$	0.2072	HOMO-1→ LUMO+2 (82%) HOMO→LUMO+2 (8%)
	365	$S_4 \leftarrow S_0$	0.0930	HOMO-1→LUMO (86%)
	358	$S_5 \leftarrow S_0$	0.5486	HOMO-1→LUMO+1(93%)

325	$S_6 \leftarrow S_0$	0.0360	HOMO-1→LUMO+2 (78%) HOMO→LUMO+3 (17%)
321	$S_7 \leftarrow S_0$	0.2162	HOMO→LUMO+3 (72%) HOMO-1→LUMO+2 (18%)
303	$S_8 \leftarrow S_0$	0.0349	HOMO→LUMO+4 (82%)
		•••	

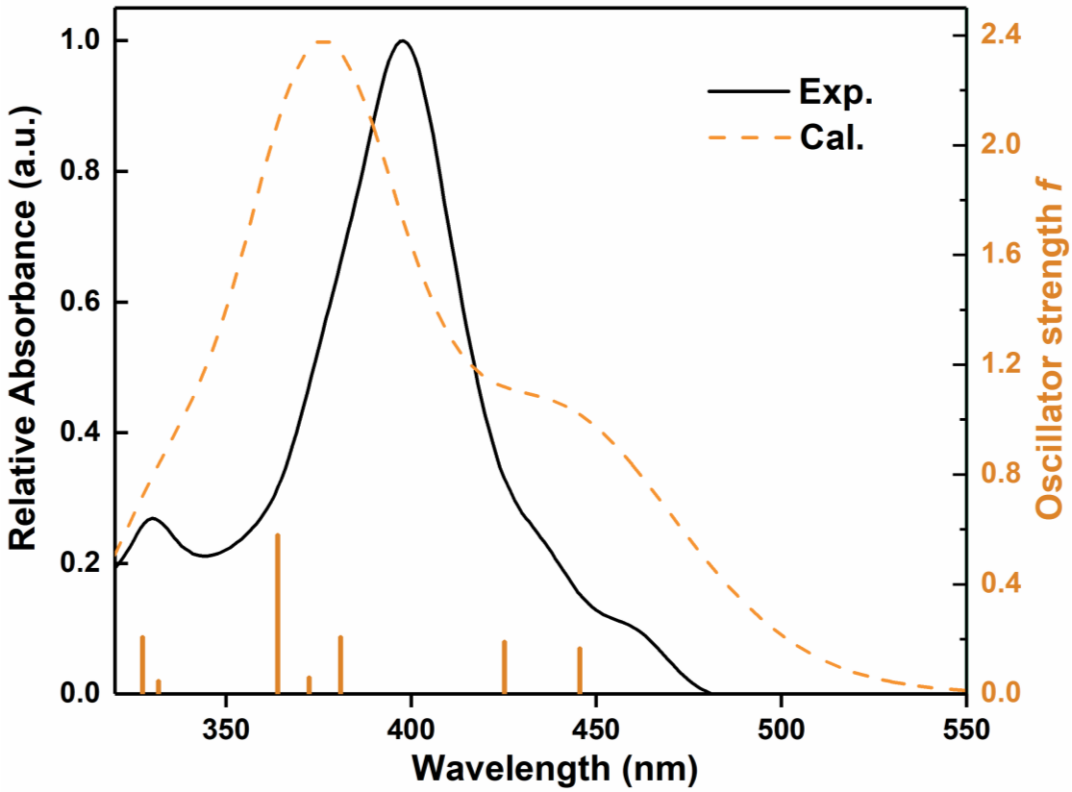

Supplementary Figure 97. Comparison of experimental absorption spectrum (blue solid line) of **1a** and the TD-DFT calculation at the B3LYP-D3(BJ)/ma-def2-TZVP//B3LYP-D3(BJ)/def2-TZVP (PCM, toluene) level of theory. Orange sticks indicate the positions and relative oscillator strengths of the calculated electronic transitions. Electronic transition energies are uncorrected.

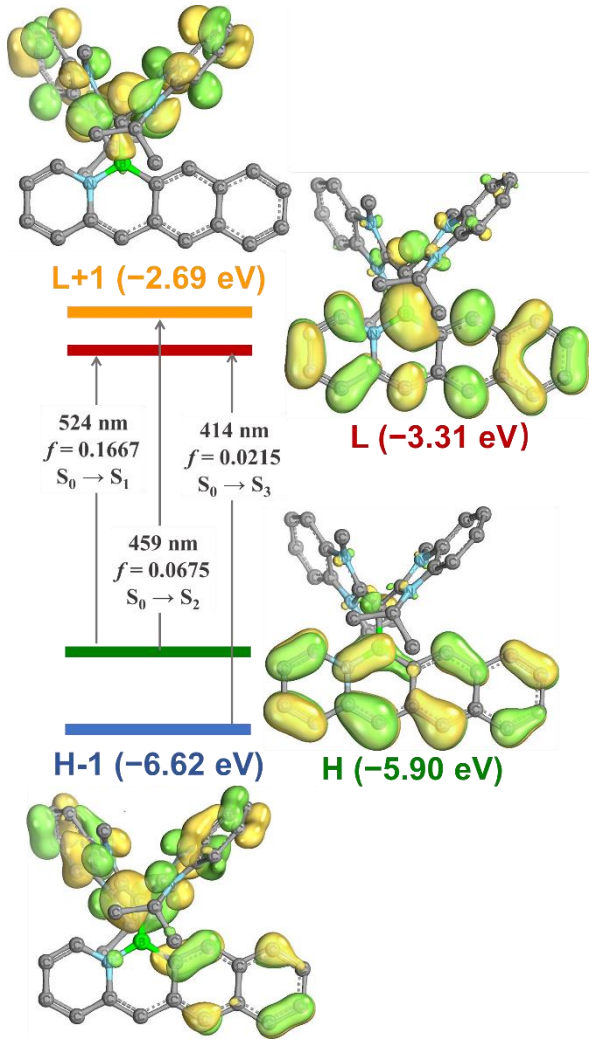

Supplementary Figure 98. Kohn–Sham molecular orbitals (HOMO-1, HOMO, LUMO and LUMO+1) and their orbital energies of **1b**. All the calculations were performed by the TD-DFT methods at (PCM, toluene)-B3LYP-D3(BJ)/ma-def2-TZVP//B3LYP-D3(BJ)/def2-TZVP level of theory. (H: HOMO, L: LUMO).

Supplementary Table 7 Selected wavelength, oscillator strength (*f*) and major configurations from the TD-DFT calculation (at the B3LYP-D3(BJ)/ma-def2-TZVP//B3LYP-D3(BJ)/def2-TZVP (PCM, toluene) level of theory) for **1b**

	λ_{cal} (nm)	electronic transitions	*f*	Major configurations
1b	524	$S_1 \leftarrow S_0$	0.1667	HOMO→LUMO (98%)
	459	$S_2 \leftarrow S_0$	0.0675	HOMO→LUMO+1 (99%)
	414	$S_3 \leftarrow S_0$	0.0215	HOMO-1→LUMO (96%)
	389	$S_4 \leftarrow S_0$	0.1718	HOMO→LUMO+2 (88%)
	371	$S_5 \leftarrow S_0$	0.6811	HOMO-1→LUMO+1(95%)
	349	$S_6 \leftarrow S_0$	0.099	HOMO→LUMO+3 (73%), HOMO→LUMO+4 (18%)
	341	$S_6 \leftarrow S_0$	0.1258	HOMO→LUMO+3 (18%),

			HOMO→LUMO+4 (62%)
324	$S_7 \leftarrow S_0$	0.0793	HOMO-1→LUMO+2 (93%)
		•••	

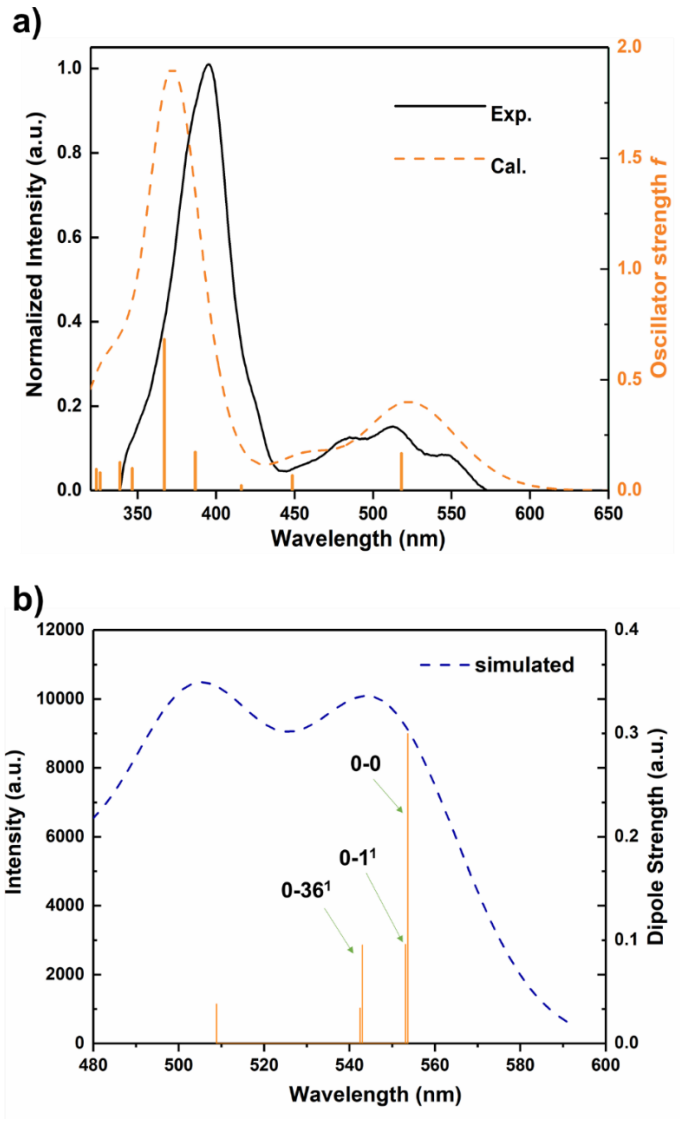

Supplementary Figure 99. a) Comparison of experimental absorption spectrum (blue solid line) of **1b** and the TD-DFT calculation at the B3LYP-D3(BJ)/ma-def2-TZVP//B3LYP-D3(BJ)/def2-TZVP (PCM, toluene) level of theory. Orange sticks indicate the positions and relative oscillator strengths of the calculated electronic transitions. Electronic transition energies are uncorrected. b) The vibronic spectrum (excitation from S_0 to S_1 state) of **1b** obtained from structures optimized at (PCM, toluene)-B3LYP-D3(BJ)/TZVP level of theory at 0 K. The 0-0 transition energy of the simulated spectrum has been shifted by 0.16 eV (based on the experimental 0-0 transition energy [2.24 eV] derived from the crossing point of the normalized absorption and emission spectra of **1b**). The orange stick lines refer to the individual vibronic models and the lengths of the bars indicate the dipole strength.

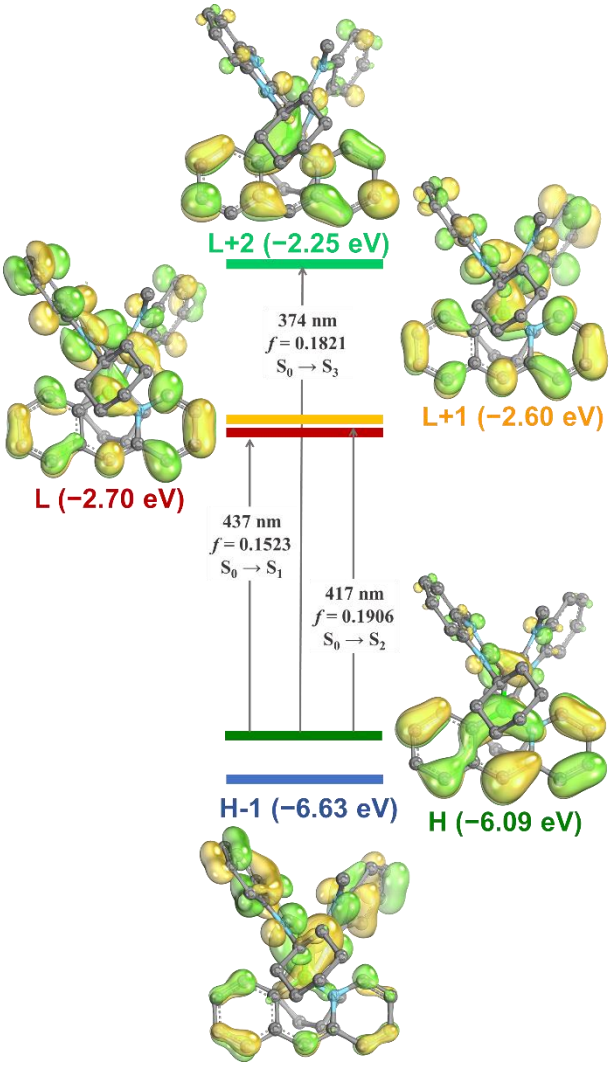

Supplementary Figure 100. Kohn–Sham molecular orbitals (HOMO-1, HOMO, LUMO, LUMO+1 and LUMO+2) and their orbital energies of **2a**. All the calculations were performed by the TD-DFT methods at (PCM, toluene)-B3LYP-D3(BJ)/ma-def2-TZVP//B3LYP-D3(BJ)/def2-TZVP level of theory. (H: HOMO, L: LUMO). The electronic transitions $S_0 \rightarrow S_1$ and $S_0 \rightarrow S_2$ are predominantly derived from vertical excitations to the LUMO and LUMO+1 from the HOMO, respectively. The LUMO (−2.70 eV) and LUMO+1 (−2.60 eV) in **2a** are energetically comparable and the second excited singlet (S_2) state is slightly above its S_1 state.

Supplementary Table 8 Selected wavelength, oscillator strength (*f*) and major configurations from the TD-DFT calculation (at the B3LYP-D3(BJ)/ma-def2-TZVP//B3LYP-D3(BJ)/def2-TZVP (PCM, toluene) level of theory) for **2a**

	λ_{cal} (nm)	electronic transitions	*f*	Major configurations
2a	437	$S_1 \leftarrow S_0$	0.1523	HOMO→LUMO (97%)
	417	$S_2 \leftarrow S_0$	0.1906	HOMO→LUMO+1 (98%)
	374	$S_3 \leftarrow S_0$	0.1821	HOMO-1→LUMO (31%) HOMO→LUMO+2 (60%)

	369	$S_4 \leftarrow S_0$	0.0893	HOMO-1→LUMO+2 (64%) HOMO→LUMO+2 (30%)
	360	$S_5 \leftarrow S_0$	0.5464	HOMO-1→LUMO+1(94%)
	327	$S_6 \leftarrow S_0$	0.0871	HOMO-1→LUMO+2 (91%)
	320	$S_7 \leftarrow S_0$	0.1551	HOMO→LUMO+3 (85%)
	303	$S_8 \leftarrow S_0$	0.0320	HOMO→LUMO+4 (84%)
			•••	

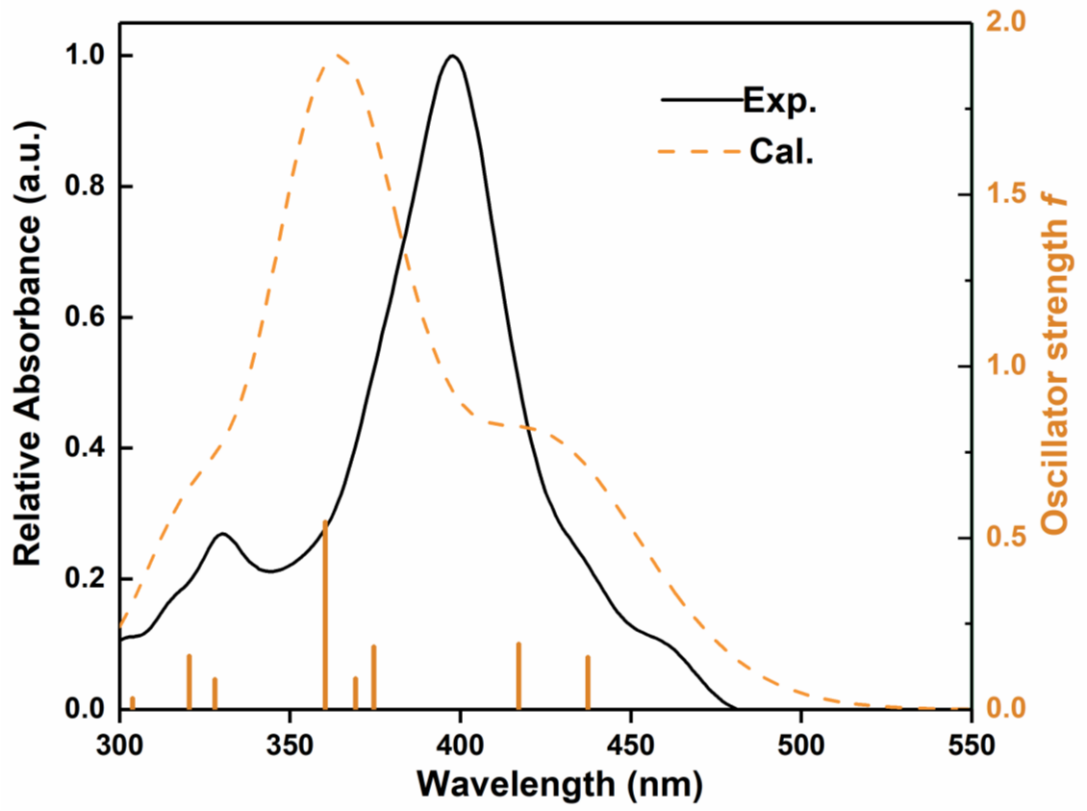

Supplementary Figure 101. Comparison of experimental absorption spectrum (blue solid line) of **2a** and the TD-DFT calculation at the B3LYP-D3(BJ)/ma-def2-TZVP//B3LYP-D3(BJ)/def2-TZVP (PCM, toluene) level of theory. Orange sticks indicate the positions and relative oscillator strengths of the calculated electronic transitions. Electronic transition energies are uncorrected.

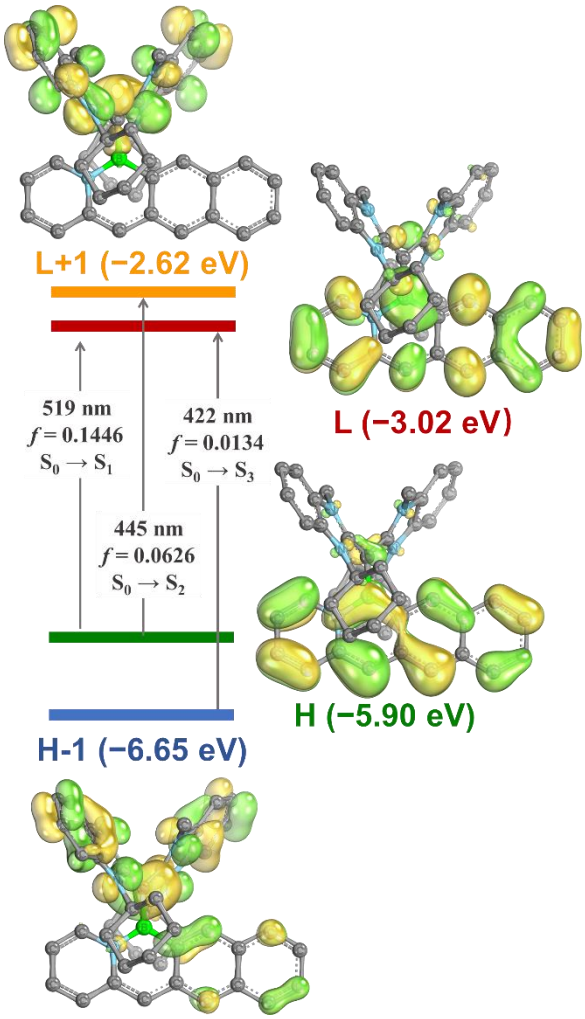

Supplementary Figure 102. Kohn–Sham molecular orbitals (HOMO-1, HOMO, LUMO and LUMO+1) and their orbital energies of **2b**. All the calculations were performed by the TD-DFT methods at (PCM, toluene)-B3LYP-D3(BJ)/ma-def2-TZVP//B3LYP-D3(BJ)/def2-TZVP level of theory. (H: HOMO, L: LUMO).

Supplementary Table 9 Selected wavelength, oscillator strength (*f*) and major configurations from the TD-DFT calculation (at the B3LYP-D3(BJ)/ma-def2-TZVP//B3LYP-D3(BJ)/def2-TZVP (PCM, toluene) level of theory) for **2b**

	λ_{cal} (nm)	electronic transitions	*f*	Major configurations
2b	519	$S_1 \leftarrow S_0$	0.1446	HOMO→LUMO (98%)
	445	$S_2 \leftarrow S_0$	0.0626	HOMO→LUMO+1 (99%)
	422	$S_3 \leftarrow S_0$	0.0134	HOMO-1→LUMO (97%)
	387	$S_4 \leftarrow S_0$	0.1744	HOMO→LUMO+2 (89%)
	370	$S_5 \leftarrow S_0$	0.7471	HOMO-1→LUMO+1(96%)
	347	$S_6 \leftarrow S_0$	0.1538	HOMO→LUMO+3 (68%), HOMO→LUMO+4 (22%)
	337	$S_7 \leftarrow S_0$	0.0561	HOMO-2→LUMO (10%), HOMO→LUMO+3 (18%),

			HOMO→LUMO+4 (62%)
329	$S_8 \leftarrow S_0$	0.0659	HOMO-1→LUMO+2 (92%)
		•••	

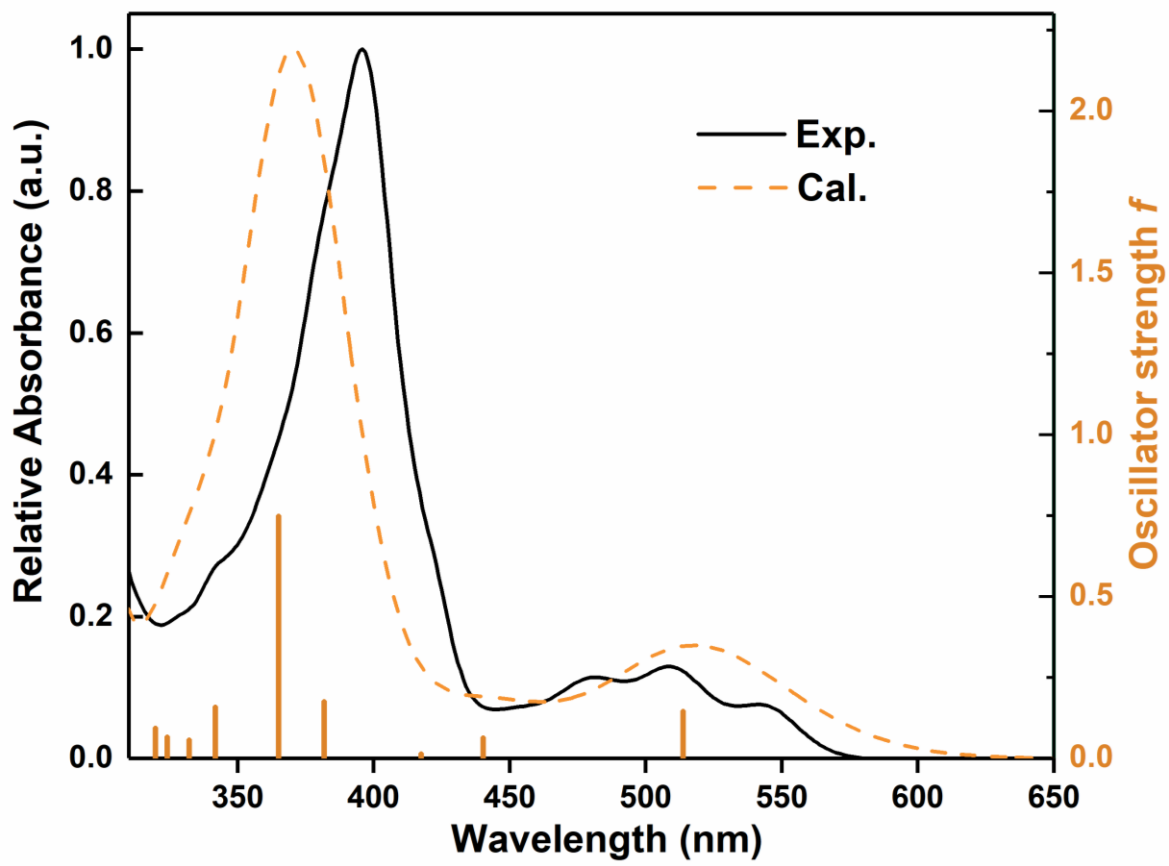

Supplementary Figure 103. Comparison of experimental absorption spectrum (blue solid line) of **2b** and the TD-DFT calculation at the B3LYP-D3(BJ)/ma-def2-TZVP//B3LYP-D3(BJ)/def2-TZVP (PCM, toluene) level of theory. Orange sticks indicate the positions and relative oscillator strengths of the calculated electronic transitions. Electronic transition energies are uncorrected.

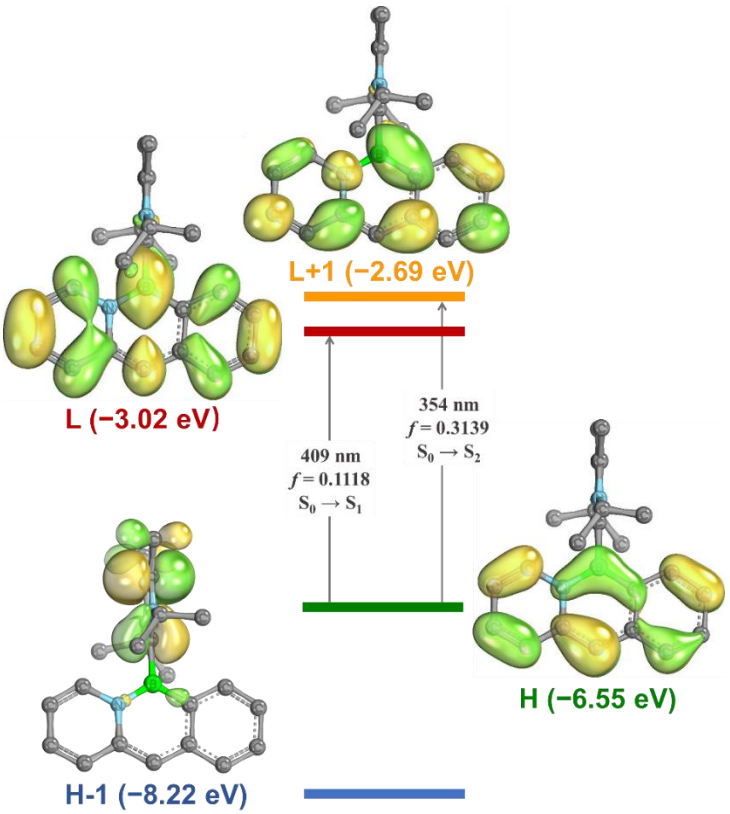

Supplementary Figure 104. Kohn–Sham molecular orbitals (HOMO-1, HOMO, LUMO and LUMO+1) and their orbital energies of **3a**. All the calculations were performed by the TD-DFT methods at (PCM, toluene)-B3LYP-D3(BJ)/ma-def2-TZVP//B3LYP-D3(BJ)/def2-TZVP level of theory. (H: HOMO, L: LUMO).

Supplementary Table 10 Selected wavelength, oscillator strength (*f*) and major configurations from the TD-DFT calculation (at the B3LYP-D3(BJ)/ma-def2-TZVP//B3LYP-D3(BJ)/def2-TZVP (PCM, toluene) level of theory) for **3a**

	λ_{cal} (nm)	electronic transitions	*f*	Major configurations
3a	404	$S_1 \leftarrow S_0$	0.1168	HOMO→LUMO (97%)
	351	$S_2 \leftarrow S_0$	0.3006	HOMO→LUMO+1 (91%)
	335	$S_3 \leftarrow S_0$	0.0128	HOMO→LUMO+2 (98%)
			•••	
	258	$S_6 \leftarrow S_0$	0.2335	HOMO-3→LUMO (30%), HOMO-2→LUMO (48%), HOMO→LUMO+5 (10%)
	250	$S_7 \leftarrow S_0$	0.5362	HOMO-3→LUMO (53%), HOMO-2→LUMO+1 (23%),
			•••	

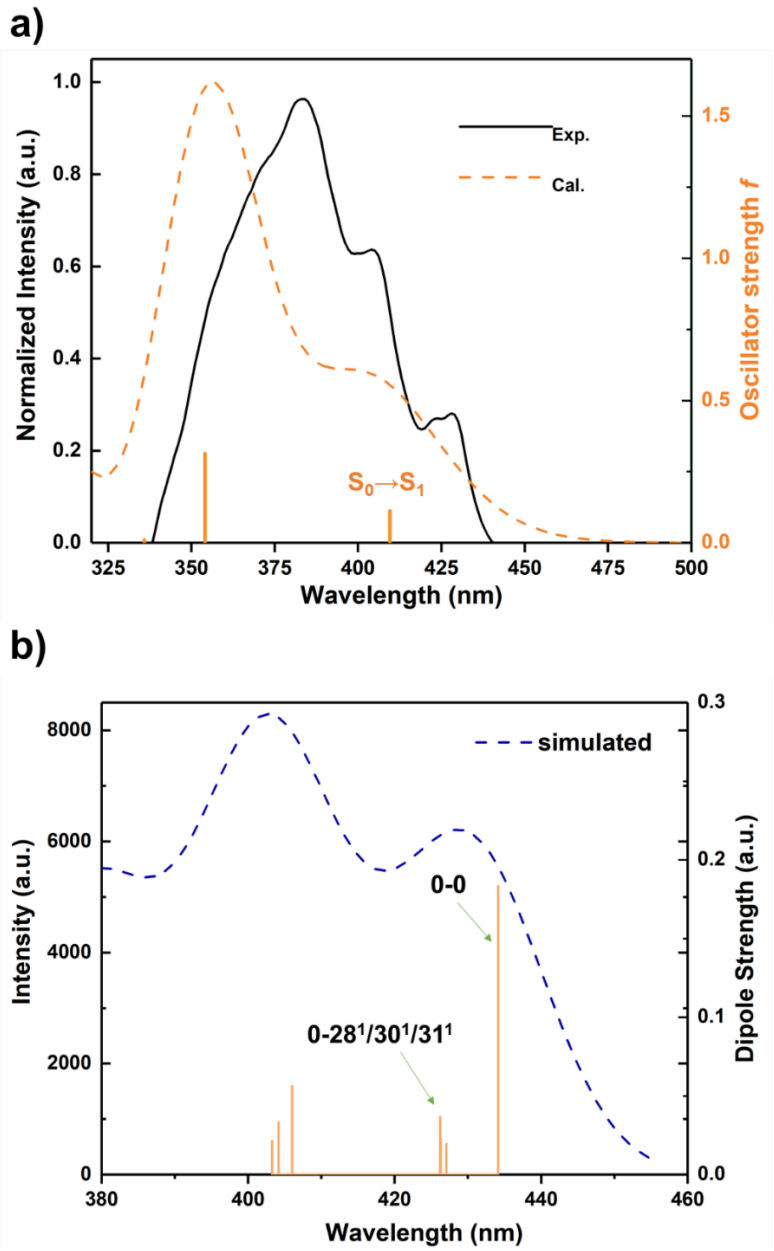

Supplementary Figure 105. a) Comparison of the theoretical and experimental absorption spectra of **3a**. Theoretical spectra were calculated at the (PCM, toluene)-B3LYP-D3(BJ)/ma-def2-TZVP//B3LYP-D3(BJ)/def2-TZVP level of theory. Orange stick lines indicate the positions and relative oscillator strengths *f* of the calculated electronic transitions. Electronic transition energies are uncorrected. b) The vibrionic spectrum (excitation from S_0 to S_1 state) of **3a** obtained from structures optimized at (PCM, toluene)-B3LYP-D3(BJ)/TZVP level of theory at 0 K. The 0-0 transition energy of the simulated spectrum has been shifted by 0.14 eV (based on the experimental 0-0 transition energy [2.89 eV] derived from the crossing point of normalized absorption and emission spectra of **3a**). The orange stick lines refer to the individual vibrionic models and the lengths of the bars indicate the dipole strength.

Supplementary Table 11. The calculated vertical emission energies ($E^{vert\text{-}fluo}$) for **1**, **2** and **3a** at PCM(toluene)-B3LYP-D3(BJ)/TZVP level of theory. $E^{vert\text{-}fluo}$: vertical emission energy of the first excited singlet at ground state geometry. $\lambda_{em}{}^{cal}$: calculated emission wavelength, in nm. ΔE_{S0}: HOMO-LUMO gap for the ground state. ΔE_{S1}: HOMO-LUMO gap for the first excited singlet state. Energies given in eV.

	1a	**1b**	**2a**	**2b**	**3a**
$E^{vert\text{-}fluo}$	2.36	1.98	2.37	2.00	2.56
$\lambda_{em}{}^{cal}$	524	624	522	621	485
ΔE_{S0}	3.38	2.85	3.25	2.88	3.55
ΔE_{S1}	3.40	2.45	3.41	2.46	3.00

The emission spectra are independent of the excitation wavelength and the obtained excitation spectra are similar to the absorption spectra (Supplementary Figure 33-37), thus $S_1 \rightarrow S_0$ fluorescence emission are observed and obey Kasha's rule. $E^{vert\text{-}fluo}$ are consistent with the observed emission peaks in the spectroscopic studies.

Calculated Values for the Energy-matching Conditions for Singlet Fission (SF)

Using the S_0 geometries of **1a**, **1b** and **2b** (obtained at B3LYP-D3(BJ)/def2-TZVP level of theory) as starting point, the S_1 and T_2 energies were computed using TD-DFT at B3LYP-D3(BJ)/def2-TZVP level of theory, while T_1 were optimized by the unrestricted density functional theory (UDFT) method at B3LYP-D3(BJ)/def2-TZVP level of theory. Their energies (S_1, T_1 and T_2) are estimated based on adiabatic processes in gas phase. The values of *<S**2>* are calculated to check the spin contamination effect on triplet excitation states, and reveal that the spin operators are extremely close to 2.000 (the exact value for triplet), indicating no spin contamination effect found for T_1 and T_2. The reliability of our calculations was verified by comparing the experimental values of $E(S_1)$, $E(T_1)$, and ΔE_{SF} of tetracene[47,48] with the respective calculated values (Supplementary Table 12), which showed the experimental and computed values for $E(S_1)$ and $E(T_1)$ agreed very well. It should be noted that complicated contribution of MOs are found for the T_2 state of **1b** [HOMO-2 → LUMO (19%), HOMO-1 → LUMO (12%), HOMO → LUMO+2 (52%), and HOMO → LUMO+3 (10%)] and tetracene [HOMO-1 → LUMO (57%), HOMO → LUMO+1 (38%)] as well as the mixed transition characters ($LE^3 + CT^3$) for T_2 states of **1b**/**2b**, thus the current single-reference DFT-based theory might be not well suited to estimate $E(T_2)$. Multireference configuration interaction methods like the complete active space self-consistent field (CASSCF) or complete active space second-order perturbation theory (CASPT2) calculations are necessary to precisely determine the $E(T_2)$, which is beyond the scope of this paper due to too high computational cost.

Supplementary Table 12. Summary of the calculated energies (in eV, at the B3LYP-D3(BJ)/def2-TZVP level) of the S_1, T_1 and T_2 states relatives to the energy of their S_0 state of **1**, **2b** and tetracene. $E(S_1)_{adiab}$: adiabatic excitation energy of the first excited singlet. $E(T_1)_{adiab}$: adiabatic excitation energy of the first excited triplet. $E(T_2)_{adib}$: adiabatic excitation energy of the second excited triplet. ΔE_{SF}: energies related to singlet fission efficiency calculated as $2E(T_1)_{adiab}$- $E(S_1)_{adiab}$. ΔE_T: energies related to $2E(T_1)_{adiab} - E(T_2)_{adiab}$

	$E(S_1)_{adiab}$	$E(T_1)_{adiab}$	$E(T_2)_{adiab}$	ΔE_{SF}	ΔE_T
1a	2.61	1.51	2.50	0.41	0.52
1b	2.20	1.14	2.22	0.08	0.06
2b	2.19	1.15	2.21	0.11	0.11
Tetracene[a]	2.25 (2.31)	1.24 (1.25)	2.34 (2.54)	0.23 (~0.2)	0.14

[a] the experimental values for tetracene are given in parentheses.

The best SF materials for a solar cell should have a very small negative ΔE_{SF} or slightly endothermic (around 0 eV), which could ensure a thermodynamically favorable SF and minimize energy loss.[49,50] Organic compounds such as tetracene or pentacene have been proven as efficient SF sensitizers. Pentacene undergoes the exoergic SF process ((ΔE_{SF} = −0.11 eV) with very high SF efficiencies, however, it is not a suitable candidate for the development of single-junction Si-based SF solar cells because its $E(T_1)$ (0.86 eV) is significantly below E_g of Si (1.11 eV).[51] For tetracene, it has a matching $E(T_1)$ (1.25 eV) and undergoes larger endoergic SF ($\Delta E_{SF} \approx 0.2$ eV) with lower SF efficiency. Nevertheless, the main drawback of tetracene and pentacene is their low photostability.

Spin-orbit Coupling (SOC) Calculations

The spin-orbit coupling (SOC) matrix elements ($<S_m|\hat{H}_{SO}|T_n>$) between S_m (m = 0, 1, 2, …) and T_n (n = 1, 2, …) states were calculated to investigate the tendency of spin-forbidden S_m/T_n state processes such as intersystem crossing (ISC) and phosphorescence. All SOCs were computed at TDDFT-B3LYP-D3(BJ)/TZVP level based on the equilibrium S_1 geometries of **1b** and **2b** and the three T_m sublevels (ms = +1, 0, −1) are considered to be degenerate. The SOCs for S_m/T_1 in **1b**/**2b** are non-zero (S_1/T_1; S_2/T_1; S_2/T_2) compared to the hydrocarbon tetracene (nearly 0 cm^{-1} between the low-lying S_m and T_n), which indicates stronger couplings and would promote the S_m/T_n ISC (via thermal and/or vibrational coupling), leading to high triplet yields for the SF process. We note that the $E(S_1)$ and $E(T_2)$ are very close in energy (similar to tetracene[48]), a feature that can lead to an S_1/T_2 reverse intersystem crossing (RISC). However, one still cannot discard the possibility for singlet exciton fission because the calculated SOC for S_1/T_2 is around 0.1 cm^{-1}, suggesting weak coupling. For an effective SF chromophore, the long-lived T_1 excitons are desirable. The results showed that the SOC elements for T_1/S_0 channel in **1b** and **2b** were less than 0.1 cm^{-1}, which is comparable to the pure hydrocarbon tetracene (all the SOCs for tetracene were nearly ~0 cm^{-1}), suggesting T_1 excitons should be long-lived and the phosphorescence would be weak.

Supplementary Table 13. Spin-orbit coupling (SOC) matrix elements (in cm^{-1}) between the low-lying singlet S_m and triplet excited states T_n of **1b**.

S_m	T_n	$< S_m\|\hat{H}_{SO}\|T_n >$
0	**1**	**0.09**
1	1	0.24
2	**1**	**0.70**
0	2	0.46
1	**2**	**0.09**
2	2	0.64

Supplementary Table 14. Spin-orbit coupling (SOC) matrix elements (in cm^{-1}) between the low-lying singlet S_m and triplet excited states T_n of **2b**.

S_m	T_n	$< S_m\|\hat{H}_{SO}\|T_n >$
0	**1**	**0.11**
1	1	0.29
2	**1**	**0.58**
0	2	0.40
1	**2**	**0.10**
2	2	0.51

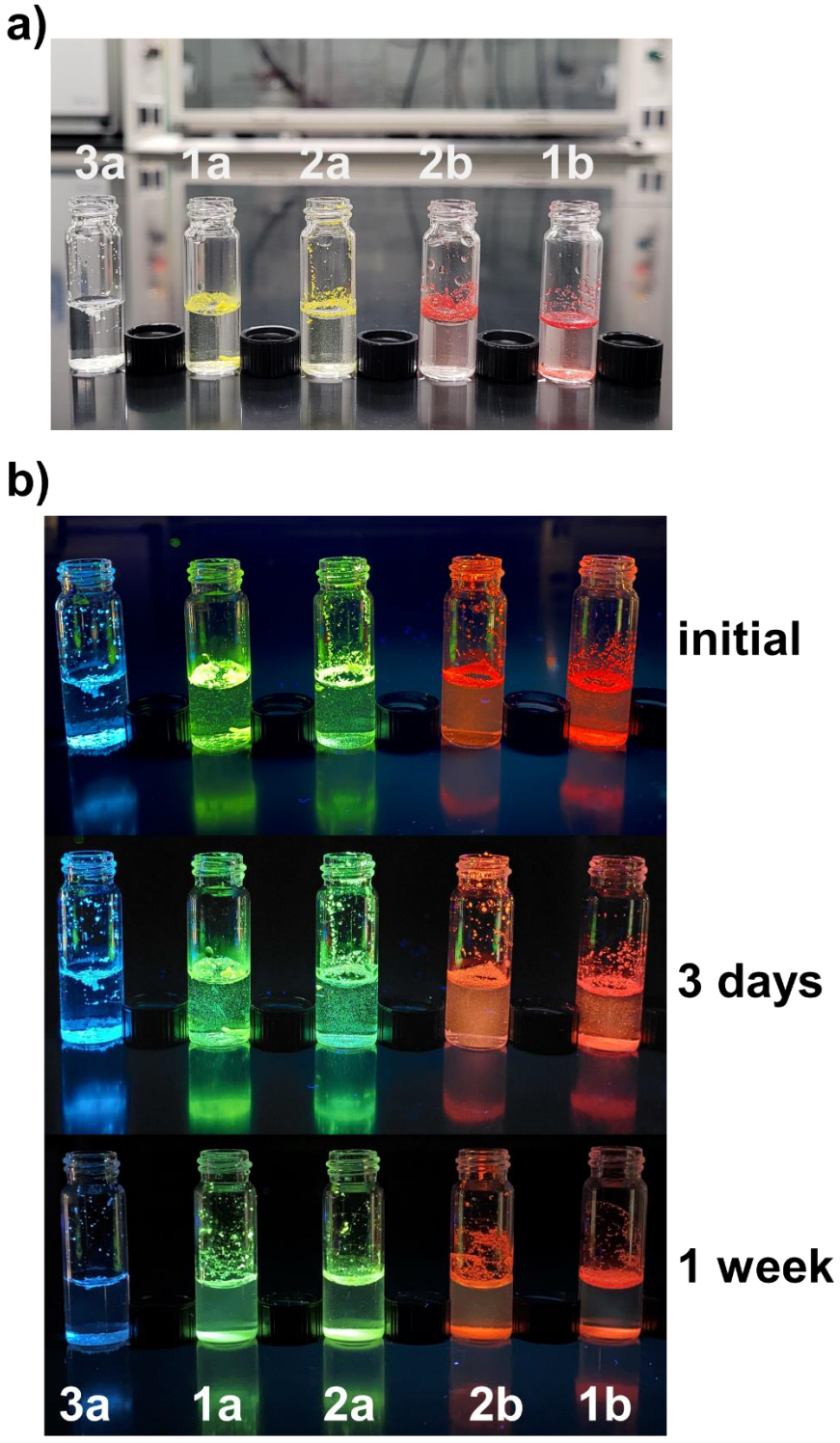

Supplementary Figure 106. Air and moisture stability tests for azaboraacenium ions **1**, **2** and **3a** in solid states. a) Solids of **1**, **2** and **3a** in vials submerging/shaking with pure water and exposure to ambient atmosphere and light. b) vials under UV light (365nm) irradiation to monitor the solid decomposition. Based on their solid fluorescence change, these compounds are able to survive for at least one week under test conditions.

UV-Vis Spectroscopy and Kinetic Studies

To experimentally assess the stability in the solution state, UV-visible spectra were obtained using a Cary 60 UV-vis spectrometer. Dilute solutions of compounds (4.0×10^{-5} M) were prepared using degassed spectroscopic grade dry THF. The cells were protected from light until each experiment began, at which point an initial spectrum was recorded. Each cell was then exposed to ambient air by loosening the cuvette cap to allow for free exchange of air, while minimizing solvent evaporation. The cells were placed on a laboratory bench under ambient light. Their UV–vis absorption spectra were taken at different time intervals to monitor the degradation process.

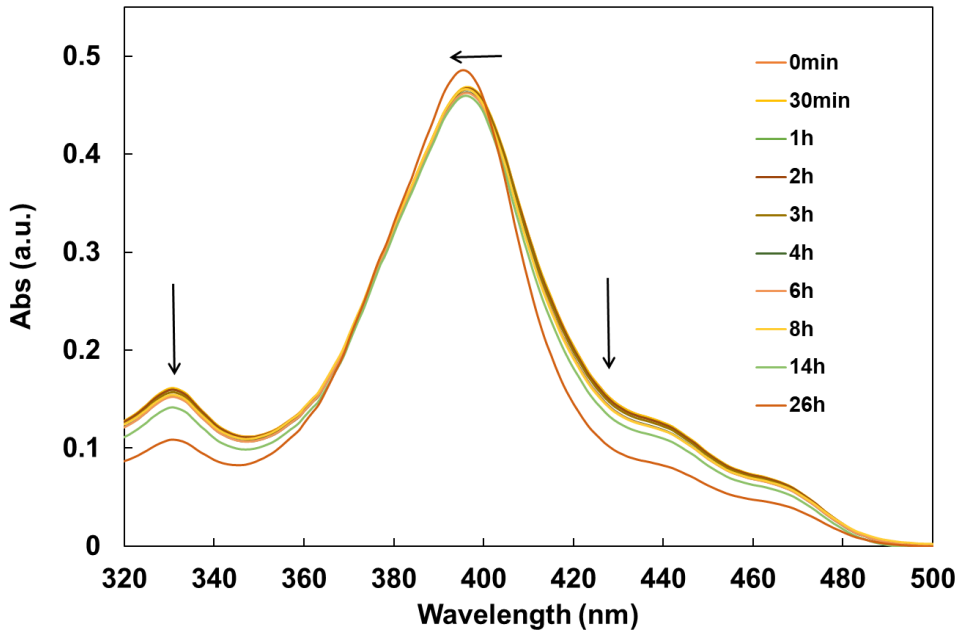

Supplementary Figure 107. Absorption spectra of **1a** in THF obtained right after the preparation and after placing the samples in the ambient light and temperature for certain times indicated in legend. The abrupt decrease in low energy band after one day was mainly due to the water (from ambient atmosphere) unavoidably accumulated in THF solution then protonated CDC ligand.

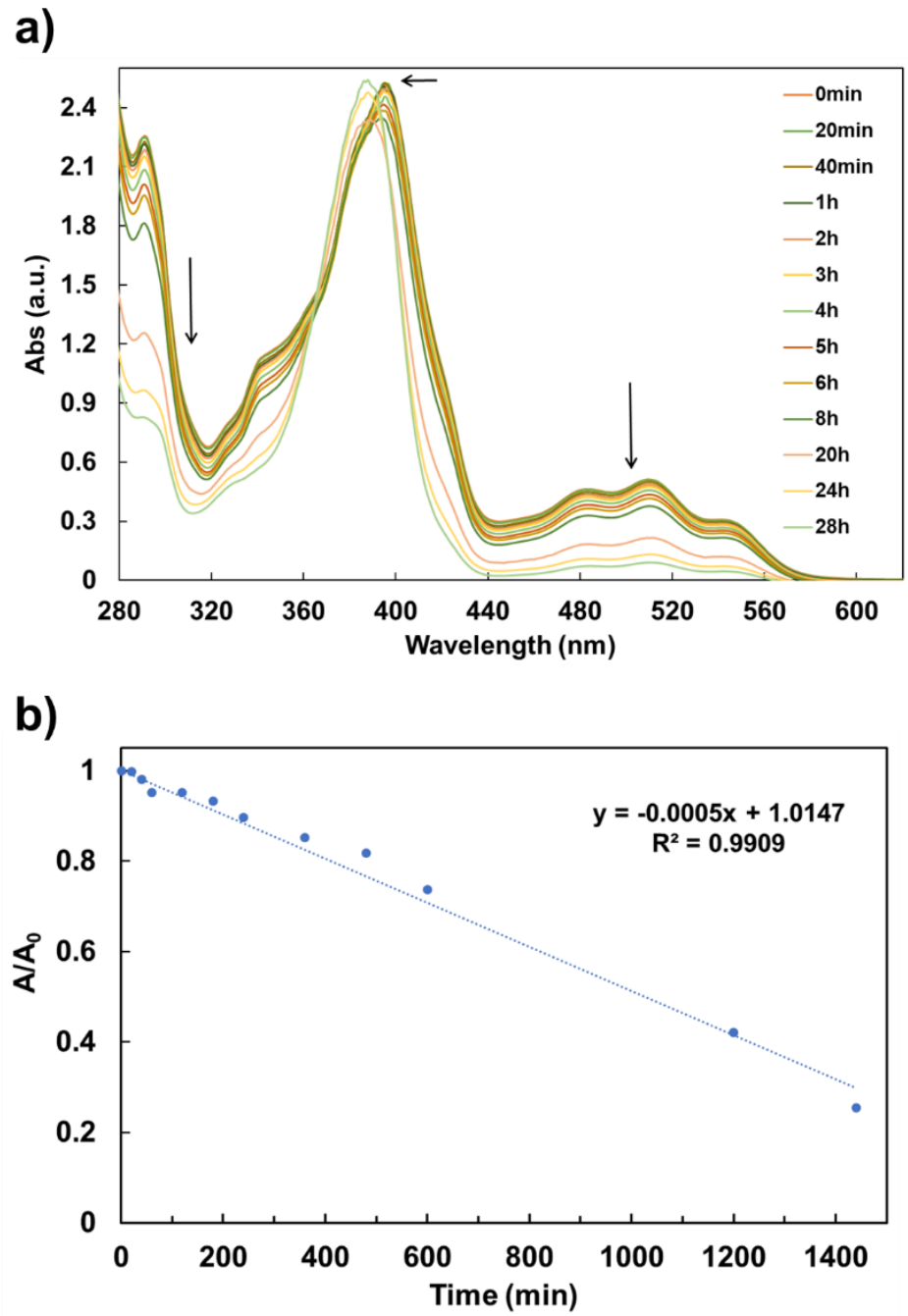

Supplementary Figure 108. a) Absorption spectra of **1a** in THF obtained right after the preparation and after placing the samples in the ambient light and temperature for certain times indicated in legend. b) Time dependence of optical density (with respect to the initial prepared solution) of **1b** in THF at the absorption peak position (monitored in 510 nm). The gradually decrease in low energy band after one day was accompanied by the water accumulated in THF solution then protonated CDC ligand. The linearly decreased intensity in low energy band suggest the decay is not first-order kinetics, which prelude the quantitative assessment of the photooxidative resistances. The degradation accompanied by the protonated CDC ligand caused by the water (from ambient atmosphere) unavoidably accumulated in THF solution.

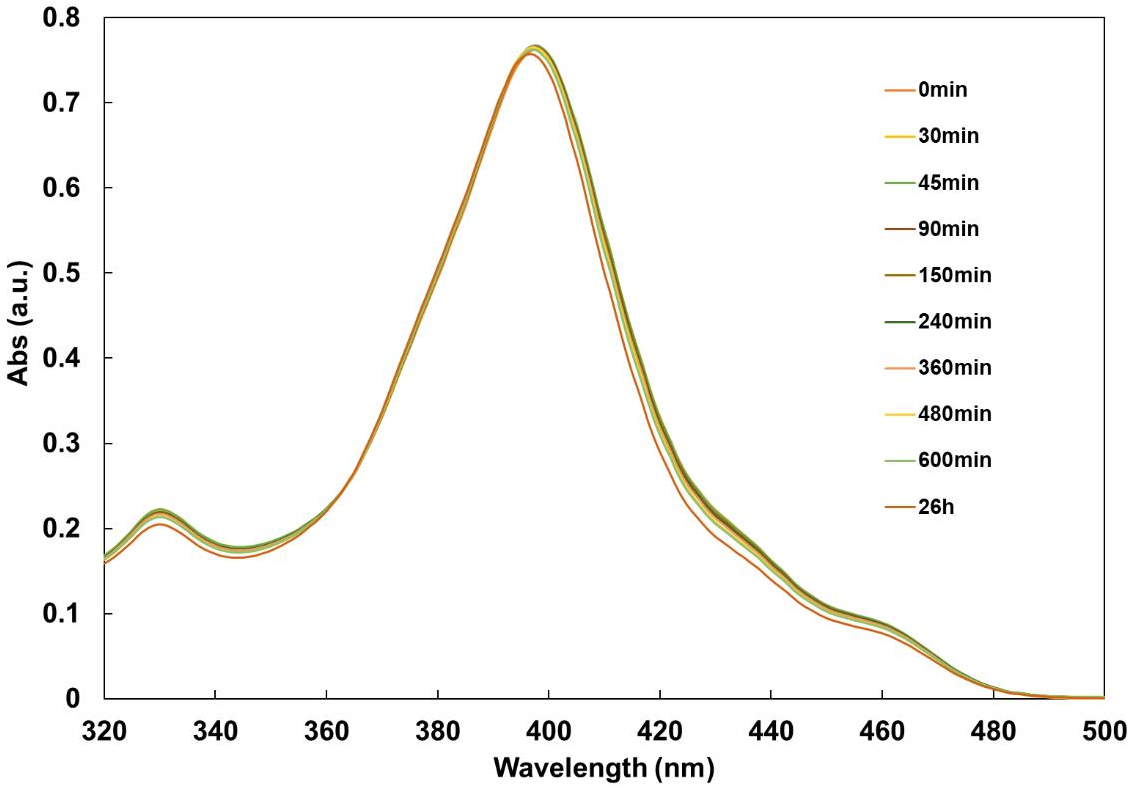

Supplementary Figure 109. Absorption spectra of **2a** in THF obtained right after the preparation and after placing the samples in the ambient light and temperature for certain times indicated in legend. The decrease in low energy band after one day was mainly due to the water (from ambient atmosphere) inevitably accumulated in THF solution then protonated the ligand.

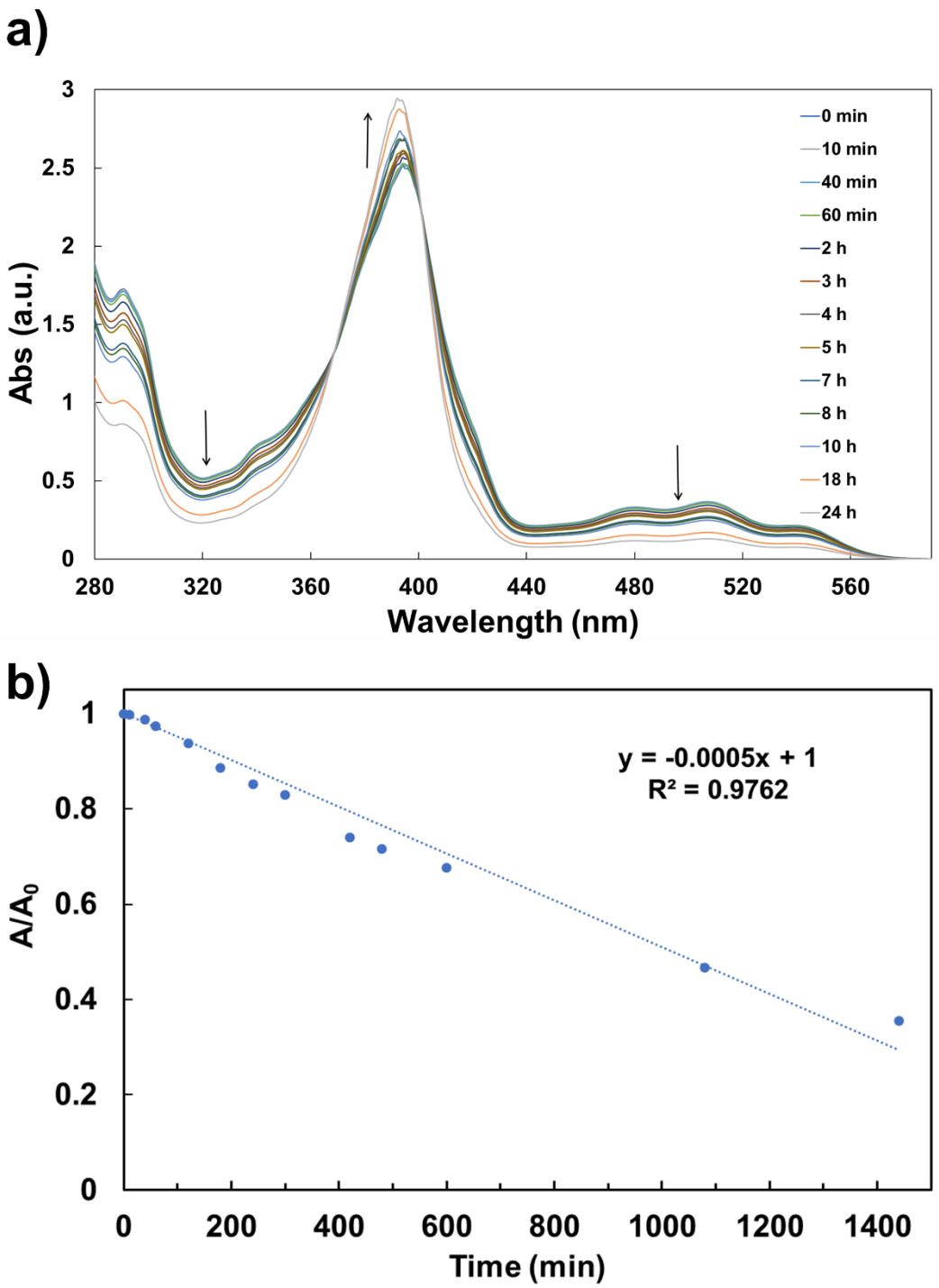

Supplementary Figure 110. a) Absorption spectra of **2b** in THF obtained right after the preparation and after placing the samples in the ambient light and temperature for certain times indicated in legend. b) Time dependence of optical density (with respect to the initial prepared solution) of **2b** in THF at the absorption peak position (monitored in 507 nm). The linearly decreased intensity in low energy band suggests the decay is not first-order kinetics, which preludes the quantitative assessment of the photooxidative resistances. The degradation accompanied

by the protonated CDC ligand caused by the water (from ambient atmosphere) inevitably accumulated in THF solution.

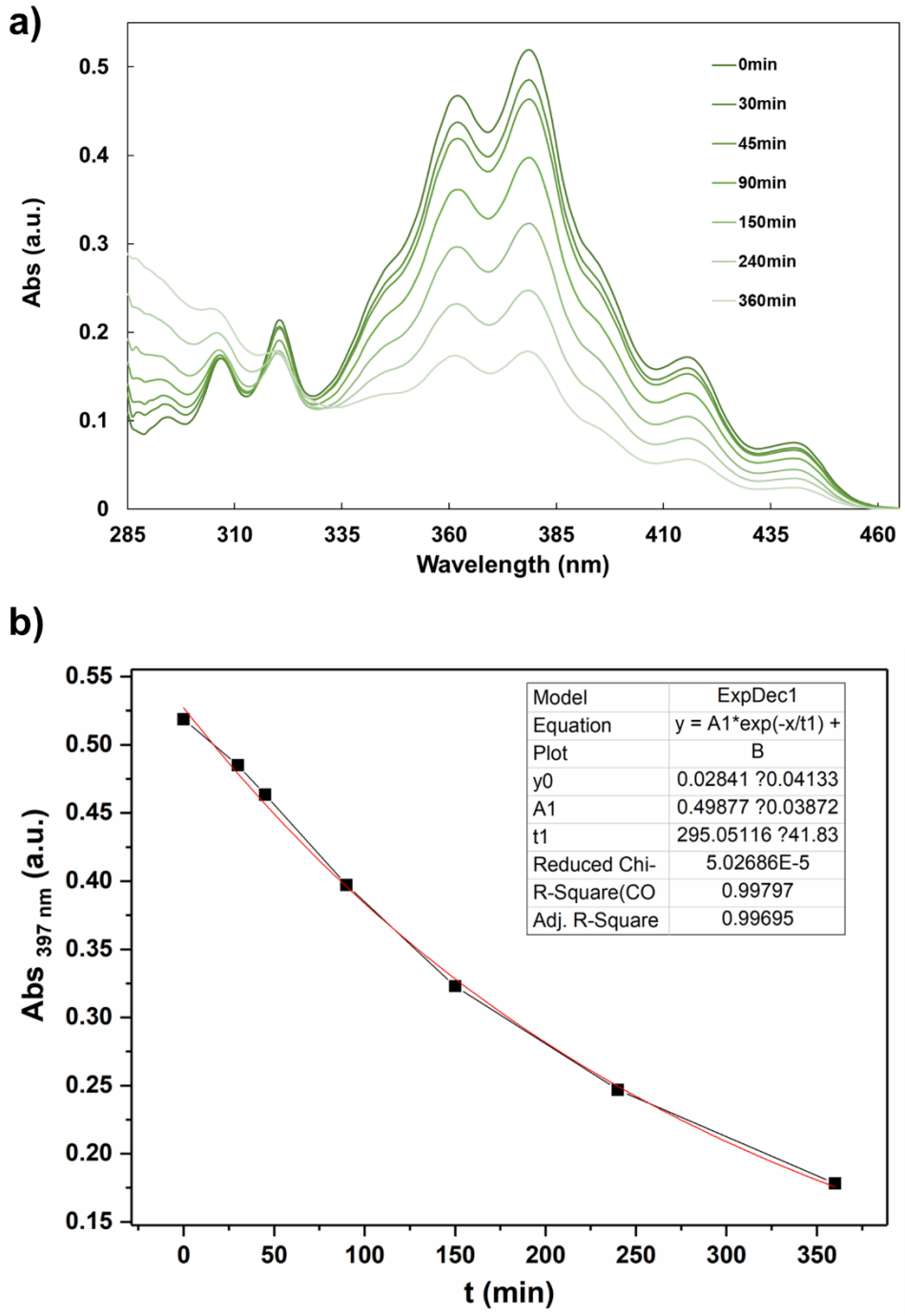

Supplementary Figure 111. a) Absorption spectra of **6a** in THF obtained right after the preparation and after placing the samples in the ambient light and temperature for certain times indicated in legend. b) Time dependence of optical density (with respect to the initial prepared solution) of **6a** in THF at the absorption peak position (monitored in 379 nm) and non-linear curve fitting for determination of the half-life.

Photooxidation of BN-acene

Tetracene and its higher homologues are highly photoreactive.[52] They undergo photochemical [4π + 4π] dimerization and/or form endoperoxide with atmospheric oxygen at the most central carbon rings. The latter also known as photooxidation, which could happen in two pathways (Supplementary Figure 114):[53] (a) The electron transfer from PAHs to the triplet oxygen ($^3O_2$) leads to the formation of cationic acenes and highly reactive anionic oxygen, then they interact with each other causing a degradation of acenes. Then, the singlet oxygen interacts with the PAHs leading to degradation. (b) The photoexcited PAHs could change into triplet state through intersystem crossing (ISC) and result in highly reactive singlet oxygen ($^1O_2$) by means of oxygen sensitization. Even so, the degradation mechanism for acenes is very complicated and still controversial.

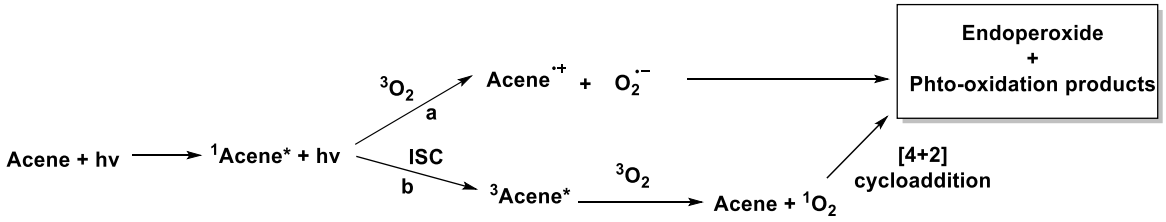

Supplementary Figure 112. Photooxidation pathways for acenes: (a) singlet oxygen sensitization (b) electron transfer. Reproduced from reference.[54]

It is suggested that the lowering of the LUMO is proposed as the source of photostabilization by reducing the rate of electron transfer to $^3O_2$ (pathway a),[54] while the lowering energy of the HOMO could reduce $^1O_2$ sensitization (pathway b).[55] Generally, lower lying HOMO and LUMO energies and small triplet excitation energies are expected to be beneficial to increase the photostability of acenes. Based on the FMOs analysis (Supplementary Figure 58-59) and the X-ray structure of photooxidation product **7**, the degradation mechanism for the aromatized BN-acene should follow similar pathways i.e., the central ring would be the more reactive sites (Supplementary Figure 113).

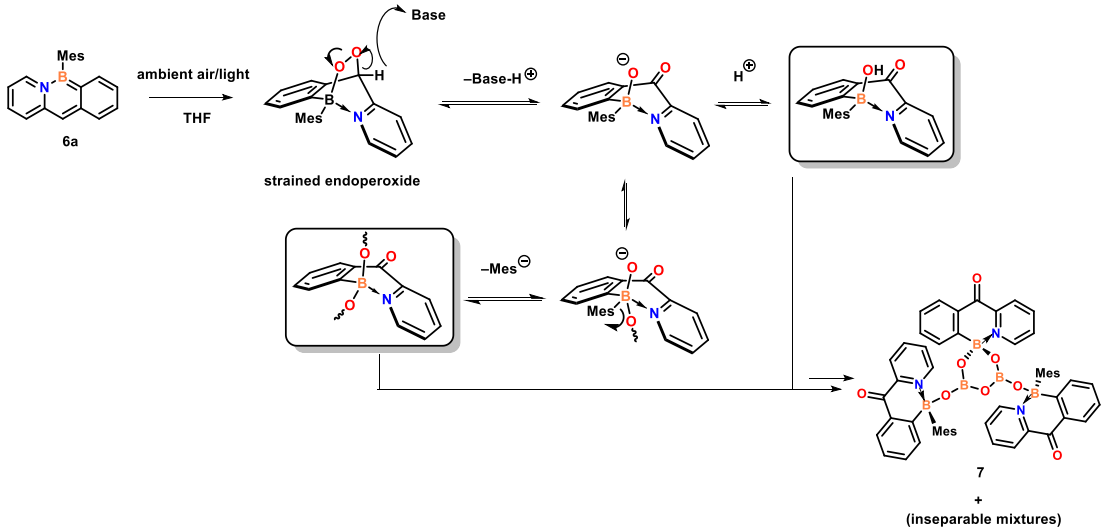

Supplementary Figure 113. Plausible zwitterionic intermediate of the photooxygenation of **6a** leading to compound **7**. The base and $B(OH)_3$ could be generated from decomposing of BN-acene skeleton in varying degrees.

Electrochemistry

All cyclic voltammetry (CV) experiments for **1-2** and **6a** were conducted using a 3-electrode geometry using a WavePico Wireless potentiostat. Electrolyte solutions (0.1 M) were prepared from anhydrous, deoxygenated solvent (**1-2** in THF, **6a** in CH_2Cl_2) and anhydrous Bu_4NPF_6. The working electrode was a glassy carbon electrode (3-mm diameter), with a Pt-coil counter electrode and an Ag/AgCl reference. Sample concentrations were *ca*. 1 mM. The ferrocene/ferrocenium (Fc/Fc^+) couple was used as an internal standard following each experiment. Compound **3a** decomposed under the electrochemical experiments. The CV test with extending scanning range (50, 100, 200, 300 mV) for **1-2** and **6a** were carried out. The redox potential signals of −1.05 V, −0.38 V and 0.5 V (*vs* Fc/Fc^+) in **1-2** were intrinsic feature of the CDC ligand rather instead of impurity effect. We guess it may be due to the high energy of the π lone pair on the CDC ligand and strong intermolecular interactions, leading to these active oxidation potentials or solvent effect in THF.

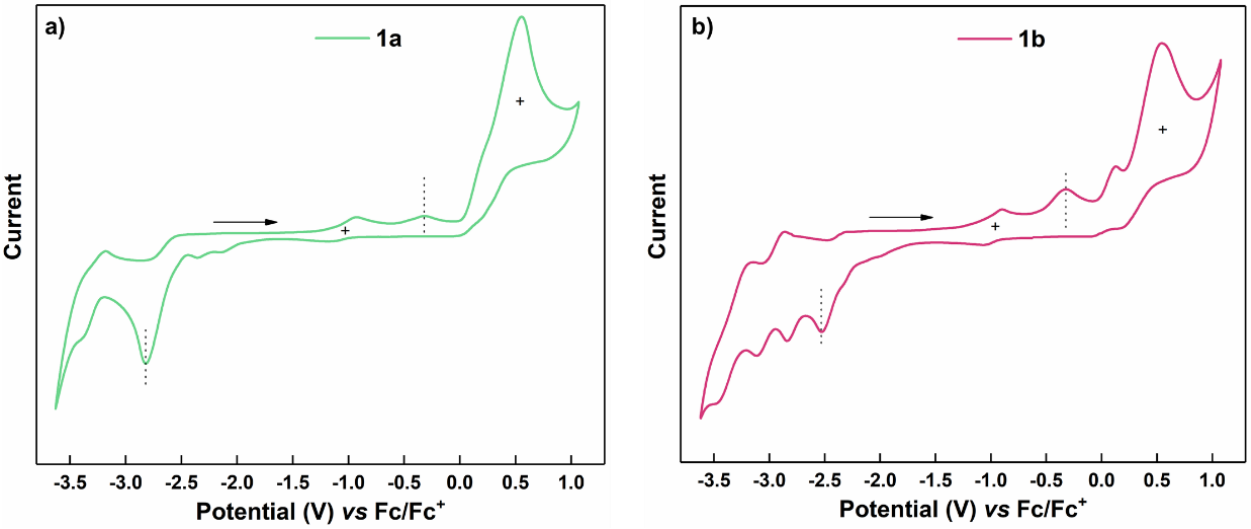

Supplementary Figure 114. Cyclic voltammograms of **1a** (a) and **1b** (b) (0.1 M Bu_4NPF_6 in THF, potential *vs* Fc/Fc^+, scanning rate v = 100 mV s^{-1}).

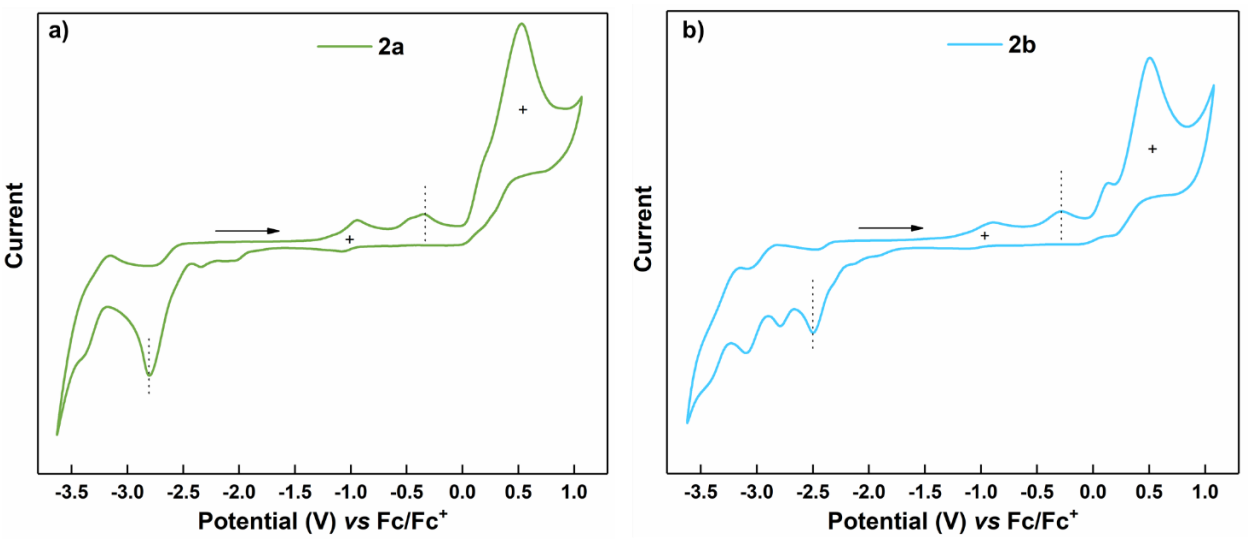

Supplementary Figure 115. Cyclic voltammograms of **2a** (a) and **2b** (b) (0.1 M Bu_4NPF_6 in THF, potential *vs* Fc/Fc^+, scanning rate v = 100 mV s^{-1}).

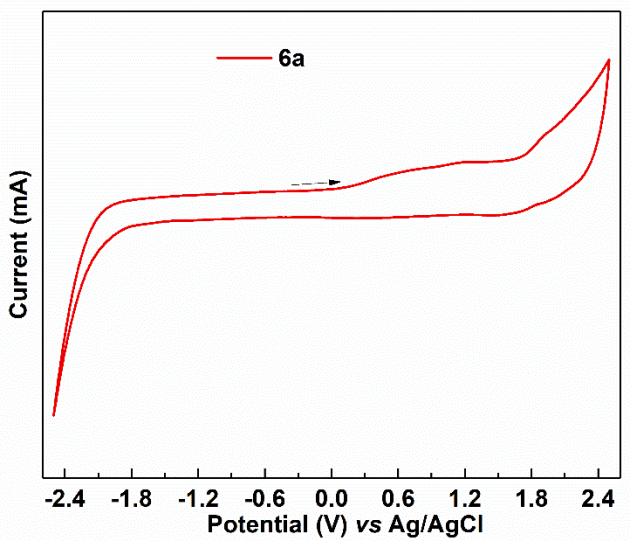

Supplementary Figure 116. Cyclic voltammograms of **6a** (0.1 M Bu_4NPF_6 in CH_2Cl_2, potential *vs* Fc/Fc^+, scanning rate v = 100 mV s^{-1}).

References

1 Yang, Y. H., Gao, Q. & Xu, S. M. Ligand-Free Iridium-Catalyzed Dehydrogenative ortho C-H Borylation of Benzyl-2-Pyridines at Room Temperature. *Advanced Synthesis & Catalysis* **361**, 858-862, (2019).

2 Chen, W. C., Hsu, Y. C., Lee, C. Y., Yap, G. P. A. & Ong, T. G. Synthetic Modification of Acyclic Bent Allenes (Carbodicarbenes) and Further Studies on Their Structural Implications and Reactivities. *Organometallics* **32**, 2435-2442, (2013).

3 Ishibashi, J. S. A., Darrigan, C., Chrostowska, A., Li, B. & Liu, S. Y. A BN anthracene mimics the electronic structure of more highly conjugated systems. *Dalton Transactions* **48**, 2807-2812, (2019).

4 Bruker. Saint; APEX4. Bruker AXS Inc., Madison, Wisconsin, USA., (2019).

5 Krause, L., Herbst-Irmer, R., Sheldrick, G. M. & Stalke, D. Comparison of silver and molybdenum microfocus X-ray sources for single-crystal structure determination. *Journal of Applied Crystallography* **48**, 3-10, (2015).

6 Sheldrick, G. M. SHELXT - Integrated space-group and crystal-structure determination. *Acta Crystallographica a-Foundation and Advances* **71**, 3-8, (2015).

7 Dolomanov, O. V., Bourhis, L. J., Gildea, R. J., Howard, J. A. K. & Puschmann, H. OLEX2: a complete structure solution, refinement and analysis program. *Journal of Applied Crystallography* **42**, 339-341, (2009).

8 Spek, A. L. PLATON SQUEEZE: a tool for the calculation of the disordered solvent contribution to the calculated structure factors. *Acta Crystallographica Section C-Structural Chemistry* **71**, 9-18, (2015).

9 Neese, F. The ORCA program system. *Wiley Interdisciplinary Reviews-Computational Molecular Science* **2**, 73-78, (2012).

10 Neese, F. Software update: The ORCA program system-Version 5.0. *Wires Comput Mol Sci* **12**, (2022).

11 Lee, C., Yang, W. & Parr, R. G. Development of the Colle-Salvetti correlation-energy formula into a functional of the electron density. *Physical Review B* **37**, 785-789, (1988).

12 Becke, A. D. DensityБ─functional thermochemistry. III. The role of exact exchange. *The Journal of Chemical Physics* **98**, 5648-5652, (1993).

13 Sch ц ┌fer, A., Huber, C. & Ahlrichs, R. Fully optimized contracted Gaussian basis sets of triple zeta valence quality for atoms Li to Kr. *The Journal of Chemical Physics* **100**, 5829-5835, (1994).

14 Weigend, F. & Ahlrichs, R. Balanced basis sets of split valence, triple zeta valence and quadruple zeta valence quality for H to Rn: Design and assessment of accuracy. *Physical Chemistry Chemical Physics* **7**, 3297-3305, (2005).

15 Grimme, S. Semiempirical hybrid density functional with perturbative second-order correlation. *Journal of Chemical Physics* **124**, (2006).

16 Johnson, E. R. & Becke, A. D. A post-Hartree-Fock model of intermolecular interactions: Inclusion of higher-order corrections. *Journal of Chemical Physics* **124**, (2006).

17 Neese, F., Wennmohs, F., Hansen, A. & Becker, U. Efficient, approximate and parallel Hartree-Fock and hybrid DFT calculations. A 'chain-of-spheres' algorithm for the Hartree-Fock exchange. *Chemical Physics* **356**, 98-109, (2009).

18 Glendening, E. D., Landis, C. R. & Weinhold, F. NBO 6.0: Natural bond orbital analysis program. *Journal of Computational Chemistry* **34**, 1429-1437, (2013).

19 Jensen, F. Segmented Contracted Basis Sets Optimized for Nuclear Magnetic Shielding. *Journal of Chemical Theory and Computation* **11**, 132-138, (2015).

20 Herges, R. & Geuenich, D. Delocalization of electrons in molecules. *Journal of Physical Chemistry A* **105**, 3214-3220, (2001).

21 Schmider, H. L. & Becke, A. D. Chemical content of the kinetic energy density. *Journal of Molecular Structure-Theochem* **527**, 51-61, (2000).
22 Gaussian 16 Rev. B.01 (Wallingford, CT, 2016).
23 Lu, T. & Chen, F. W. Multiwfn: A multifunctional wavefunction analyzer. *Journal of Computational Chemistry* **33**, 580-592, (2012).
24 Mitoraj, M. P., Michalak, A. & Ziegler, T. A Combined Charge and Energy Decomposition Scheme for Bond Analysis. *Journal of Chemical Theory and Computation* **5**, 962-975, (2009).
25 Radon, M. On the properties of natural orbitals for chemical valence. *Theoretical Chemistry Accounts* **120**, 337-339, (2008).
26 Knizia, G. Intrinsic Atomic Orbitals: An Unbiased Bridge between Quantum Theory and Chemical Concepts. *Journal of Chemical Theory and Computation* **9**, 4834-4843, (2013).
27 Knizia, G. http://www.iboview.org/.
28 Gao, X. *et al.* Evaluation of Spin-Orbit Couplings with Linear-Response Time-Dependent Density Functional Methods. *Journal of Chemical Theory and Computation* **13**, 515-524, (2017).
29 Grimme, S. & Hansen, A. A Practicable Real-Space Measure and Visualization of Static Electron-Correlation Effects. *Angewandte Chemie International Edition* **54**, 12308-12313, (2015).
30 Bauer, C. A., Hansen, A. & Grimme, S. The Fractional Occupation Number Weighted Density as a Versatile Analysis Tool for Molecules with a Complicated Electronic Structure. *Chemistry Б—⌠ A European Journal* **23**, 6150-6164, (2017).
31 Lee, T. J. & Taylor, P. R. A diagnostic for determining the quality of single-reference electron correlation methods. *International Journal of Quantum Chemistry* **36**, 199-207, (1989).
32 Riplinger, C., Sandhoefer, B., Hansen, A. & Neese, F. Natural triple excitations in local coupled cluster calculations with pair natural orbitals. *The Journal of Chemical Physics* **139**, 134101, (2013).
33 Pople, J. A., HeadБ — ▒Gordon, M. & Raghavachari, K. Quadratic configuration interaction. A general technique for determining electron correlation energies. *The Journal of Chemical Physics* **87**, 5968-5975, (1987).
34 Kendall, R. A., Dunning, T. H., Jr. & Harrison, R. J. Electron affinities of the firstБ—▒row atoms revisited. Systematic basis sets and wave functions. *The Journal of Chemical Physics* **96**, 6796-6806, (1992).
35 Bader, R. F. W. *Atoms in molecules: a quantum theory*. (Clarendon Press; Oxford University Press, 1994).
36 Espinosa, E., Alkorta, I., Elguero, J. & Molins, E. From weak to strong interactions: A comprehensive analysis of the topological and energetic properties of the electron density distribution involving X-H center dot center dot center dot F-Y systems. *Journal of Chemical Physics* **117**, 5529-5542, (2002).
37 Johnson, E. R. *et al.* Revealing Noncovalent Interactions. *Journal of the American Chemical Society* **132**, 6498-6506, (2010).
38 Papajak, E., Zheng, J. J., Xu, X. F., Leverentz, H. R. & Truhlar, D. G. Perspectives on Basis Sets Beautiful: Seasonal Plantings of Diffuse Basis Functions. *Journal of Chemical Theory and Computation* **7**, 3027-3034, (2011).
39 Zheng, J. J., Xu, X. F. & Truhlar, D. G. Minimally augmented Karlsruhe basis sets. *Theoretical Chemistry Accounts* **128**, 295-305, (2011).
40 Barone, V. & Cossi, M. Quantum calculation of molecular energies and energy gradients in solution by a conductor solvent model. *Journal of Physical Chemistry A* **102**, 1995-2001, (1998).

41 Improta, R., Scalmani, G., Frisch, M. J. & Barone, V. Toward effective and reliable fluorescence energies in solution by a new state specific polarizable continuum model time dependent density functional theory approach. *Journal of Chemical Physics* **127**, (2007).
42 Caricato, M. *et al.* Formation and relaxation of excited states in solution: A new time dependent polarizable continuum model based on time dependent density functional theory. *Journal of Chemical Physics* **124**, (2006).
43 Guido, C. A., Jacquemin, D., Adamo, C. & Mennucci, B. Electronic Excitations in Solution: The Interplay between State Specific Approaches and a Time-Dependent Density Functional Theory Description. *Journal of Chemical Theory and Computation* **11**, 5782-5790, (2015).
44 Barone, V., Bloino, J., Biczysko, M. & Santoro, F. Fully Integrated Approach to Compute Vibrationally Resolved Optical Spectra: From Small Molecules to Macrosystems. *Journal of Chemical Theory and Computation* **5**, 540-554, (2009).
45 Baiardi, A., Bloino, J. & Barone, V. General Time Dependent Approach to Vibronic Spectroscopy Including Franck-Condon, Herzberg-Teller, and Duschinsky Effects. *Journal of Chemical Theory and Computation* **9**, 4097-4115, (2013).
46 Hachmann, J., Dorando, J. J., Avil ц ╘s, M. & Chan, G. K.-L. The radical character of the acenes: A density matrix renormalization group study. *The Journal of Chemical Physics* **127**, 134309, (2007).
47 Tomkiewicz, Y., Groff, R. P. & Avakian, P. Spectroscopic Approach to Energetics of Exciton Fission and Fusion in Tetracene Crystals. *Journal of Chemical Physics* **54**, 4504-+, (1971).
48 Arnold, S. & Whitten, W. B. Temperature-Dependence of the Triplet Exciton Yield in Fission and Fusion in Tetracene. *Journal of Chemical Physics* **75**, 1166-1169, (1981).
49 Akdag, A., Havlas, Z. & Michl, J. Search for a Small Chromophore with Efficient Singlet Fission: Biradicaloid Heterocycles. *Journal of the American Chemical Society* **134**, 14624-14631, (2012).
50 Burdett, J. J. & Bardeen, C. J. The Dynamics of Singlet Fission in Crystalline Tetracene and Covalent Analogs. *Accounts of Chemical Research* **46**, 1312-1320, (2013).
51 Wu, T. C. *et al.* Singlet fission efficiency in tetracene-based organic solar cells. *Applied Physics Letters* **104**, (2014).
52 Dong, S. Q., Ong, A. & Chi, C. Y. Photochemistry of various acene based molecules. *Journal of Photochemistry and Photobiology C-Photochemistry Reviews* **38**, 27-46, (2019).
53 Mazur, M. & Blanchard, G. J. Photochemical and electrochemical oxidation reactions of surface-bound polycyclic aromatic hydrocarbons. *Journal of Physical Chemistry B* **108**, 1038-1045, (2004).
54 Maliakal, A., Raghavachari, K., Katz, H., Chandross, E. & Siegrist, T. Photochemical stability of pentacene and a substituted pentacene in solution and in thin films. *Chem Mater* **16**, 4980-4986, (2004).
55 Kaur, I. *et al.* Substituent Effects in Pentacenes: Gaining Control over HOMO-LUMO Gaps and Photooxidative Resistances. *Journal of the American Chemical Society* **130**, 16274-16286, (2008).